Ab Initio Study of the Structures, Energetics and Reactions of Some Chemical Systems

LI Chi–Lun

A Thesis Submitted in Partial Fulfilment

of the Requirements for the Degree of

Master of Philosophy

in

Chemistry

June 2002

Ab Initio Study of the Structures, Energetics and Reactions of Some Chemical Systems

Abstract

We have applied an ab initio molecular orbital calculations to study a number of interesting chemical systems. These investigations include: (i) a Gaussian–3 (G3) study on the photodissociation of phenylacetylene and formation of 1,3,5–hexatriyne, (ii) a G3 study of the photoionization and dissociative photoionization channels of cyanoethylene, (iii) a Gaussian–2 study of structures, energetics, and reactions of $C_2H_3S^-$ anions, (iv) high–level calculations of the bond energies of Fe^+–D, Fe^+–H_2O, and Fe^+–CO, (v) identification of charge–localized and –delocalized forms of the rhodizonate dianion by various levels of theory, and (vi) Franck–Condon factor calculations of several butene and dichloroethene isomers. The result of each of these projects is reported in a self–contained chapter in this thesis.

In most of these studies, reasonable agreement is obtained between our computational results and available experimental data. This agreement lends confidence to those results with no experimental data available as well as to the reaction mechanisms proposed.

利用從頭計算法對一些化學體系的結構、力能學及反應之研究

摘要：

在本論文中，我們運用分子軌道理論中的從頭計算法探討一些有趣的化學體系。 這些探討包括：(i) 採用 Gaussian–3 (G3)理論研究苯乙炔的光分解通道和己三炔–[1,3,5]的形成；(ii) 利用 G3 理論研究氯乙烷的光電離分解通道；(iii) 採用 Gaussian–2 理論對 $C_2H_3S^-$ 陰離子的結構、力能學及反應進行研究；(iv) 利用高級的計算理論研究 Fe^+–D， Fe^+–H_2O，及 Fe^+–CO 的鍵能；(v) 離域化與非離域化之 $C_6O_6^{2-}$ 離子的辨認；(vi) 丁烷與雙氯乙烷同分異構物之 Franck–Condon 因素的計算。 這些研究的結果分別記載於本論文中不同的章節裏。

由於我們很多的計算結果與現存的實驗數據吻合，令我們相信其餘有關反應通道及力能的結果是可靠的。

Acknowledgments

I am very much indebted to my supervisor, Professor Wai–Kee Li, whose guidance and encouragement have made this thesis possible.

I also wish to thank:

Dr. See–Wing Chiu, at the University of Illinois, who suggested the project of $C_2H_3S^-$ anion;

Dr. Yu–San Cheung who helped me and gave me opinions on finishing the peak assignments in Chapter 7.

Table of Contents

Chapter 1
Introduction

Accurate and reliable predictions of energetics for molecular systems are the main objectives in quantum chemistry. In the past decade or so, Pople and his co–workers proposed a series of ab initio methods, the Gaussian–n (Gn) models,[1–11] in order to achieve these goals. Their aim is to develop a general procedure for accurate energies applicable for a variety of molecular systems. The Gn models, based on a series of additivity approximations,[8,9] consist of a sequence of single–point calculations to provide an accurate prediction on the energetics of a given molecular system. The Gn models include: Gaussian–1 (G1),[1,2] Gaussian–2 (G2),[3,4] and Gaussian–3 (G3)[5–7] levels of theory and their less expensive variants (*vide infra*). These methods have been shown to be able to determine the energetics of the molecular systems with an average absolute deviation from experiment to be within 10 kJ mol^{-1} (or ~2 kcal mol^{-1} or ~0.1 eV).

Since the G1 model yields less accurate results than G2 and G3, this method has not been applied widely. In this thesis, we employ the G3 method to study the structures and energetics of some selected chemical systems. In addition, a modified G2 method, G2++ method,[12] has also been used to study the dissociation mechanisms of the $C_2H_3S^-$ anions.

1.1 Remark on the Location of Transition Structures

In this thesis, all stationary points on the potential energy surface were characterized by vibrational frequency calculations. In other words, equilibrium structures have only real vibrational frequencies, while transition structures (TSs) have one and only one imaginary frequency. For each TS, the "reactant(s)" and "product(s)" were confirmed by intrinsic reaction coordinate (IRC) calculations. Also, for the dissociation channels that we claim to involve only bond breaking and no TSs, we did try to locate the TS(s) for them and found none.

1.2 Scaling factor

Ab initio harmonic vibrational frequencies are usually larger than the

fundamentals observed experimentally. A major source of this disagreement is the neglect of anharmonicity in the theoretical calculations. Other sources of errors include the incompleteness of electron correlation and the use of finite basis sets. The overestimation of ab initio harmonic vibrational frequencies is found to be relatively uniform, and, as a result, generic frequency scaling factors are often applied. For example, frequency values computed at the Hartree–Fock (HF) level are usually overestimated by about 10%–12%. Therefore, an empirical scaling factor of 0.8929 is applied to the frequencies computed at the HF level. Use of the scaling factor has been demonstrated to produce good agreement with experiment for a wide range of systems. The scaling factors, which are usually determined by a direct comparison between the computed and experimental frequencies, for different levels are now available in the literature.[13]

1.3 Natural Bond Orbital (NBO) Analysis

The Natural Bond Orbital (NBO) analysis is carried out in order to study the bonding and interactions in the various $C_2H_3S^-$ isomers, iron(I) complexes and rhodizonate dianion in Chapters 4, 5, and 6, respectively. This analysis allows us to isolate the interaction energies in low–order perturbative expressions of easily interpretable form and to relate these expressions to chemical explanations. The bond interaction in the various isomers is discussed in terms of stabilization energies, $\Delta E_{(2)}$, which is calculated by the second–order perturbation analysis of the Fock matrix obtained in the NBO analysis.[14] By this perturbational approach, the donor–acceptor interaction involving a filled orbital φ (donor) and an unfilled antibonding orbital φ^* (acceptor) can be quantitatively described. Specifically, this stabilization energy is calculated by the following expression:

$$\Delta_{\varphi\varphi^*}E_{(2)} = -2\frac{(<\varphi \mid F \mid \varphi^* >)^2}{\varepsilon_{\varphi^*} - \varepsilon_{\varphi}}$$

where F is the Fock operator and ε_{φ} and ε_{φ^*} are the NBO energies of the donor and acceptor orbitals, respectively.[15]

1.4 Scope of the Thesis

In the following Chapters, the calculation results of a number of novel

molecular systems will be discussed. In Chapter 2, the photodissociation of phenylacetylene and the formation of 1,3,5–hexatriyne are studied with the G3 method. In Chapter 3, the photoionization and dissociative ionization channels of cyanoethylene are investigated with the G3 method. The potential energy surface of $C_2H_3S^-$ anions is studied with the G2++ method in Chapter 4. In Chapter 5, the bond energies and the bonding properties of Fe^+–D, Fe^+–CO, and Fe^+–H_2O are investigated. In Chapter 6, the charge–delocalized and –localized forms of rhodizonate dianion are studied. In Chapter 7, Franck-Condon factor calculations of the cations of *cis*–2–butene, *trans*–2–butene, isobutene, *cis*–dichloroethene, and *trans*–dichloroethene are carried out. Finally, a conclusion will be given in Chapter 8.

Editorial Note: Each chapter of this thesis should be treated as separate entity. In other words, it has its own numbering system for molecular species, equations, tables, figures, and references.

1.5 References

1. Pople, J. A.; Head-Gordon, M.; Fox, D. J.; Raghavachari, K.; Curtiss, L. A. *J. Chem. Phys.* **1989**, *90*, 5622.
2. Curtiss, L. A.; Jones, C.; Trucks, G. W.; Raghavachari, K.; Pople, J. A. *J. Chem Phys.* **1990**, *93*, 2537.
3. Curtiss, L. A.; Raghavachari, K.; Trucks, G. W.; Pople, J. A. *J. Chem. Phys.* **1991**, *94*, 7221.
4. Curtiss, L. A.; Raghavachari, K.; Pople, J. A. *J. Chem. Phys.* **1993**, *98*, 1293.
5. Curtiss, L. A.; Raghavachari, K.; Redfern, P. C.; Rassolov, V. R.; Pople, J. A. *J. Chem. Phys.* **1998**, *109*, 7764.
6. Curtiss, L. A.; Redfern, P. C.; Raghavachari, K.; Rassolov, V. R.; Pople, J. A. *J. Chem. Phys.* **1999**, *110*, 4703.
7. Curtiss, L. A.; Redfern, P. C.; Raghavachari, K.; Pople, J. A. *J. Chem. Phys.* **2001**, *114*, 108.
8. Curtiss, L. A.; Carpenter, J. E.; Raghavachari, K.; Pople, J. A. *J. Chem. Phys.* **1992**, *96*, 9030.
9. Curtiss, L. A.; Raghavachari, K.; Pople, J. A. *Chem. Phys. Lett.* **1993**, *214*, 183.

10. Curtiss, L. A.; Raghavachari, K.; Redfern, P. C.; Pople, J. A. *J. Chem. Phys.* **1997**, *106*, 1063.
11. Curtiss, L. A.; Raghavachari, K.; Redfern, P. C.; Pople, J. A. *J. Chem. Phys.* **1998**, *109*, 42.
12. Chiu, S.-W.; Lau, K.-C.; Li, W.-K. *J. Phys. Chem. A*. **1999**, *103*, 6003.
13. Scott, A. P.; Radom, L. *J. Phy. Chem.* **1996**, *100*, 16502.
14. Reed, A. E.; Curtiss, L. A.; Weinhold, F. *Chem. Rev.* **1988**, *88*, 899.
15. Klaptke, T. M.; Schulz, A. *Quantum Chemical Methods in Main-Group Chemistry*; Wiley: Chichester, 1998.

Chapter 2

A Gaussian–3 Study on the Photodissociation of Phenylacetylene and Formation of 1,3,5–Hexatriyne

Abstract

Recently, Suits et al. carried out an UV photochemical investigation of phenylacetylene using photofragment translational spectroscopy at a wavelength of 193 nm. This dissociation of phenylacetylene was found to yield a primary channel: C_6H_4 + C_2H_2. The product C_6H_4 may be benzyne, (*Z*)–, or (*E*)–3–hexene–1,5–diyne. Gaussian–3 (G3) calculations have been applied to study the photodissociation of phenylacetylene. For the formation of benzyne from the dissociation of phenylacetylene, two pathways have been investigated. The calculated barrier for the one–step path is 135.5 kcal mol^{-1}, which is lower than the other one by 35.0 kcal mol^{-1}. The calculated barrier for the formation of (*Z*)–3–hexene–1,5–diyne from phenylacetylene is 135.2 kcal mol^{-1}, while the attempt to study the formation of (*E*)–3–hexene–1,5–diyne from phenylacetylene computationally has failed. With sufficient energy, the (*Z*)– and/or (*E*)–3–hexene–1,5–diyne molecules can undergo secondary dissociation to produce 1,3,5–hexatriyne and molecular hydrogen. At the G3 level, the barriers of these reactions are 107.9 and 102.7 kcal mol^{-1}, respectively. The G3 heat of formation of 1,3,5-hexatriyne is 163.4 kcal mol^{-1} and this value agrees well with experiment. In addition, the ionization energies of different reactants and products are also calculated and all the results agree reasonably with experiment.

2.1 Introduction

Polycyclic aromatic hydrocarbons (PAHs) have been proposed as species responsible for the unidentified emission bands observed from the interstellar medium (ISM).[1,2] The ISM was thought to be chemically barren, but it has become clear that this is false. Indeed, more than 100 species have been detected in space, and the list is growing by several molecules each year. While some of the molecules known to be present are relatively uninteresting from a terrestrial perspective (e.g., water, hydrogen cyanide, ammonia), the majority of them are rather exotic. Particularly the more unusual molecules are carbon–rich species such as the cyanopolyynes, acetylenic radicals, cumulene carbenes ($:CC_nH_2$ (n = 2, 3, and 5)), and the three–membered ring compound cyclopropenylidene.[3]

Molecular photodissociation is the principal process competing with radiative relaxation of PAHs in the interstellar medium. The photostability of policyclic aromatic hydrocarbons is of importance in view of their astrophysical role.[4] Research on photostability of PAHs has been carried out to understand their stability and their photofragments under ultraviolet (UV) irradiation.[5-9] The most common fragmentation is the loss of hydrogen atoms. However, acetylene loss appears to be very common in noncompact PAH cations such as naphthalene, anthracene, and phenanthrene.

Phenylacetylene is an aromatic molecule with an unsaturated side group and, like other cyclic aromatic hydrocarbons, it is believed to be an important contributor to the formation of PAH in combustion and in interstellar space.[10-13]

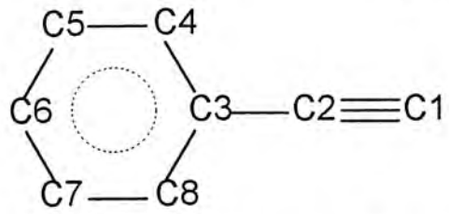

Recently, Suits et al. performed an UV photochemical investigation of phenylacetylene using photofragment translational spectroscopy.[14] The study was carried out at 193 nm. At this wavelength, one primary photochemical pathway was identified:

$$C_6H_5{-}CCH + h\nu_{193} \rightarrow C_6H_4 + HCCH$$

This reaction produces two closed–shell molecules: acetylene (HCCH) and (*Z*)–3–hexene–1,5–diyne, (*E*)–3–hexene–1,5–diyne (C_6H_4), and/or benzyne. The energy available in this reaction is sufficient to induce a secondary reaction:

$$C_6H_4 \rightarrow C_6H_2 + H_2$$

and C_6H_2 had been characterized as 1,3,5–hexatriyne.

The aim of this work is to determine the possible mechanisms for the formation of the C_6H_4 isomers from phenylacetylene and the formation of 1,3,5–hexatriyne from (*Z*)–3–hexene–1,5–diyne and (*E*)–3–hexene–1,5–diyne (C_6H_4).

2.2 Computational Method

The ab initio model of theory employed in this work is the Gaussian–3 (G3) method.[15] In this method, the geometry optimization of a molecule is carried out at the MP2(full)/6–31G(d) level. The zero–point vibrational energy is done at the HF/6–31G(d) level, with scaling factor of 0.8929. To calculate the G3 energy, single–point calculations at the levels of QCISD(T)/6–31G(d), MP4/6–31G(d), MP4/6–31+G(d), MP4/6–31G(2df,p), and MP2(full)/G3large (where G3large is a modified 6–311+G(3df,2p) basis set) are carried out, all based on the aforementioned optimized geometry.

In this work, the transition states structures (TSs) of a number of reactions have been identified. The "reactants" and "products" of a given TS are confirmed by intrinsic reaction coordinate[16,17] calculations.

After the G3 energy of a species is calculated, the heat of formation at 0 K and 298 K (ΔH_{f0} and ΔH_{f298}) for this species can be obtained in the following manner. For molecule AB, its ΔH_{f0} and ΔH_{f298} are calculated from the G3 heat of reaction ΔH_{rT} (A + B → AB) and the respective experimental ΔH_f(A) and ΔH_f(B) for atoms A and B.

All of the calculations have been carried out using the Gaussian 98 package of programs.[18]

2.3 Results and Discussion

The structural formulas of the polyatomic species involved in this work, along with their symmetry point groups, are shown in Figure 1. Figure 2 illustrates the geometries of the TSs involved. The calculated G3 energies (E_0), enthalpies at 298 K (H_{298}), heats of formation at 0 K (ΔH_{f0}) and 298 K (ΔH_{f298}) of all the species and TSs involved in the dissociation of phenylacetylene (**1**) are listed in Table 1. The respective schematic potential energy surfaces (PESs) for the reactions studied are displayed in Figures 3 to 7.

Five dissociation channels are found, which include two plausible mechanisms for the formation of benzyne (**4**) from the dissociation of **1**, the dissociation of **1** into (*Z*)–3–hexene–1,5–diyne (**9**), and the formation of 1,3,5–hexatriyne (**11**) from (*Z*)–3–hexene–1,5–diyne (**9**) and (*E*) –3-hexene–1,5–diyne (**12**). The mechanism for the formation of **12** from **1** was not found by calculation, even though the possibility of the formation of **12** from **1** cannot be ruled out.

2.3.1 Phenylacetylene → Acetylene + Benzyne. There are two plausible ways by which phenylacetylene (**1**) can dissociate into benzyne (**4**) and acetylene (**6**). In the first pathway found, summarized in Figure 3, **1** first rearranges into isomer **2** (benzocyclopropenemethylene) when a proton shifts from C4 to C1 through **TS1**. The singlet isomer **2** then excites to the triplet state, **3**, which is 69.2 kcal mol^{-1} higher in energy. Subsequently, **3** cleavages through **TS2** to generate benzyne (**4**) and vinylidene (**5**), and the latter can readily rearrange to the much more stable acetylene (**6**). In this process, **4** and **5** are produced by the rupture of two C–C single bonds and an additional energy of 63.0 kcal mol^{-1} is required to overcome this barrier. The overall barrier for this reaction is 170.5 kcal mol^{-1}.

The second plausible way of **1** to dissociate into **4** and **6** is much simpler. A hydrogen atom shifts from C4 to C2 and the C3–C2 bond breaks at the same step, as in **TS4**, to produce **4** and **6**. The reaction barrier is 135.5 kcal mol^{-1}, which is lower than that for the previous mechanism by 35.0 kcal mol^{-1}. This second pathway has a lower barrier because bond breaking and bond forming occur simultaneously in **TS4**, while bond breaking dominates in **TS2**.[19] The PES for this one–step path is shown in Figure 4.

2.3.2 Phenylacetylene → Acetylene + (*Z*)–3–Hexene–1,5–diyne. In the pathway shown in Figure 5, hydrogen migration from C5 to C3 precedes dissociation of acetylene. To do this, hydrogen shifts first from C5 to C4 through **TS5** to form isomer 7, which is 90.1 kcal mol^{-1} less stable than **1**. The hydrogen atom then moves from C4 to C3 to form **8** through **TS6**. This step has a barrier of 44.3 kcal mol^{-1}. From **7** to **8**, the C3–C4, C3–C8, and C6–C7 bonds lengthen significantly. The most obvious are the C3–C8 and C6–C7 bonds, which increase from 1.371 Å to 1.539 Å and from 1.384 Å to1.478 Å, respectively. Isomer **8** dissociates into **6** and (*Z*)–3–hexene–1,5–diyne (**9**) via **TS7**, with a barrier of 54.1 kcal mol^{-1}. Here bond rupture occurs at the C3–C8 and C6–C7 bonds. In **TS7**, the C7–C8 bond has a length of 1.253 Å, which is between 1.352 Å in isomer **8** and 1.216 Å in **6**. From **7** to **8**, the C5–C6 bond decreases from 1.429 Å to 1.334 Å, which becomes 1.222 Å in **9**, indicating the formation of a triple bond.

2.3.3 (*Z*)–3–Hexene–1,5–diyne / (*E*)–3–Hexene–1,5–diyne → 1,3,5–Hexatriyne and Molecular Hydrogen. Two closed–shell molecules, 1,3,5–hexatriyne (**11**) and hydrogen molecule, are produced from the dissociation of (*Z*)–3–hexene–1,5–diyne (**9**) or (*E*)–3–hexene–1,5–diyne (**12**). The PESs for these two reactions are shown in Figures 6 and 7.

The mechanisms for these two dissociation reactions are similar and the barrier heights of the two processes are also alike. The elimination of hydrogen molecule from either diyne can be achieved by passing through the two TSs. The first step involves a 3,4–hydride shift in either **9** or **12**. The energy barriers of this step are 73.8 kcal mol^{-1} and 76.0 kcal mol^{-1}, respectively, for **9** and **12**, which are comparable to the barrier of hydride shift in ethylene (74.5 kcal mol^{-1}).[20] Isomers **10** and **13** formed by the hydride shifts are 65.8 and 67.5 kcal mol^{-1} higher in energy than **9** and **12**, respectively.

At the next step, isomers **10** and **13** can lose H_2 molecule to produce **11**. The energy barriers of this step are 42.1 and 35.2 kcal mol^{-1} for **9** and **12**, respectively. The barrier heights of the loss of hydrogen molecule in these cases are similar to that (34.1 kcal mol^{-1}) of elimination of molecular hydrogen from ethylidene to produce acetylene.[20]

2.3.4 Evaluation of Thermochemical Data. The heats of formation for **1** and most of the product isomers mentioned in this work have been calculated (see Table 1) using the G3 method. The experimental heats of formation of **9** and **12** are 129.5 and 128.6 kcal mol^{-1}, [21] respectively. The G3 ΔH_{f298} for these two isomers, 126.7 and 126.4 kcal mol^{-1}, agree well with the experiment. The G3 heats of formation of **11** are found to be 163.4 and 164.8 kcal mol^{-1} for 0 K and 298 K, respectively, and the former agrees well with the result of the experimental work (160 kcal mol^{-1}).[14] The G3 heats of formation at 298 K for **1** and **4** are 79.0 and 110.9 kcal mol^{-1}, respectively, which are in good accord with experimental data found in the literature, 73.3 ± 0.4 [22] and 105.2 ± 2.4 kcal mol^{-1}.[23]

2.3.5 Evaluation of Ion Energetics Data. In addition, ionization energy (IE) for **1** is calculated to be 8.87 eV, which is in good agreement with the result found in experiment, 8.82 ± 0.02 eV.[24] The experimental IEs for **9**, **12**, and **4** are 9.10 ± 0.02,[25] 9.07 ± 0.02,[25] and 9.77 ± 0.03 eV,[26] respectively. The calculated values are 9.09, 9.06, and 9.89 eV respectively. The IEs calculated for **9** and **12** are in excellent agreement with the experimental data, while the result calculated for **4** is in fair accord with the experiment. Finally, the G3 IE of **11** is 9.52 eV, which is in excellent agreement with experiment, 9.50 ± 0.02 eV.[27]

2.4 Conclusions

This chapter presents the theoretical study of the photodissociation of phenylacetylene. The experimental 193–nm dissociation of phenylacetylene was found to yield a primary channel: $C_6H_4 + C_2H_2$. One of the possible C_6H_4 isomer is benzyne. For the formation of benzyne from the dissociation of phenylacetylene, two pathways have been identified. The calculated barrier for the one–step path is 135.5 kcal mol^{-1}, which is lower than that for the multi–step pathway by 35.0 kcal mol^{-1}. Another C_6H_4 isomer which can be dissociated from phenylacetylene is (*Z*)–3–hexene–1,5–diyne. The G3 barrier for the production of (*Z*)–3–hexene–1,5–diyne from the dissociation of phenylacetylene is 135.2 kcal mol^{-1}. With sufficient energy, the (*Z*)– and/or (*E*)–3–hexene–1,5–diyne molecules can undergo secondary dissociation to produce 1,3,5–hexatriyne and molecular

hydrogen. Theoretically, the barrier of these reaction are 107.9 and 102.7 kcal mol^{-1}, respectively. The heats of formation calculated for (*Z*)–3–hexene–1,5–diyne and (*E*)–3–hexene–1,5–diyne have excellent agreement with the results of experiment. The G3 heats of formation of 1,3,5–hexatriyne are 163.4 and 164.8 kcal mol^{-1} at 0 K and 298 K, respectively, and these values agree well with experiment. The G3 heats of formation for phenylacetylene and benzyne are 79.0 and 110.9 kcal mol^{-1}, respectively, and are fair accord with the experimental results. The ionization energies of (*Z*)– and (*E*)–3–hexene–1,5–diyne, and 1,3,5–hexatriyne are calculated to be 9.09, 9.06, and 9.52 eV, respectively. They are in excellent agreement with the experimental values.

2.5 References

1. Léger, A.; Puget, J. L. *Astron. Astrophys.* **1984**, *137*, L5.
2. Allamandola, J. L.; Tielens, A.G. G. M.; Baker, J. R. *Astrophys. J.* **1985**, *290*, L25.
3. Thaddeus, P.; McCarthy, M. C.; Travers, M. J.; Gottlieb, C. A.; Chen, W. *Faraday Discuss.* **1998**, *109*, 121.
4. Jochims, H. W.; Rühl, E. Baumgärtel, H.; Tobita, S.; Leach, S. *Astrophys. J.* **1994**, *420*, 307.
5. Ling, Y.; Lifshitz, C. *J. Phys. Chem.* **1995**, *99*, 11074.
6. Ling, Y.; Lifshitz, C. *J. Phys. Chem. A* **1998**, *102*, 708.
7. Ling, Y.; Martin, J. M. L.; Lifshitz, C. *J. Phys. Chem. A* **1997**, *101*, 219.
8. Granucci, G.; Ellinger, Y.; Boissel, P. *Chem. Phys.* **1995**, *191*,165.
9. Gotkis, Y.; Oleinikova, M.; Noar, M.; Lifshitz, C. *J. Phys. Chem.* **1993**, *97*, 12282.
10. Hopf, H.; Musso, H.; *Angew. Chem.* **1969**, *81*, 704.
11. Hopf, H.; Musso, H.; *Angew. Chem. Int. Ed.* **1969**, *8*, 680.
12. Herzler, J.; Frank, P. *Ber. Bunsen-Ges. Phys. Chem.* **1992**, *96*, 1333.
13. Hofmann, J.; Zimmermann, G.; Guthier, K.; Hebgen, P.; Homann, K. H. *Liebigs. Ann.* **1995**, *1995*, 637.
14. Sorkhabi, O.; Qi, F.; Rizvi, A. H.; Suits, A. G. *J. Am. Chem. Soc.* **2001**, *123*, 671.
15. Curtiss, L. A.; Raghavachari, K.; Redfern, P. C.; Rassolov, V.; Pople, J. A. *J. Chem. Phys.* **1998**, *109*, 7764.

16. Gonzalez, C.; Schlegel, H. B. *J. Chem. Phys.* **1989**, *90*, 2154.
17. Gonzalez, C.; Schlegel, H. B. *J. Phys. Chem.* **1990**, *94*, 5523.
18. Frisch, M. J.; Trucks, G. W.; Schlegel, H. B.; Scuseria, G. E.; Robb, M. A.; Cheeseman, J. R.; Zakrzewski, V. G.; Montgogery, J. A.; Jr.; Stratmann, R.E.; Burant, J. C.; Dapprich, S.; Millam, J. M.; Daniels, A. D.; Kudin, K. N.; Strain, M. C.; Farkas, O.; Tomasi, J.; Barone, V.; Cossi, M.; Cammi, R.; Mennucci, B.; Pomelli, C.; Adamo, C.; Clifford, S.; Ochterski, J.; Petersson, G. A.; Ayala, P. Y.; Cui, Q.; Morokuma, K.; Malick, D. K.; Rabuck, A. D.; Raghavachari, K.; Foresman, J. B.; Cioslowski, J.; Ortiz, J. V.; Baboul, A. G.; Stefanov, B. B.; Liu, G.; Liashenko, A.; Piskorz, P.; Komaromi, I.; Gomperts, R.; Martin, R. L.; Fox, D. J.; Keith, T.; Al-Laham, M. A.; Peng, C. Y.; Nanayakkara, A.; Gonzalez, C.; Challacombe, M.; Gill, P. M. W.; Johnson, B.; Chen, W.; Wong, M. W.; Andres, J. L.; Gonzalez, C.; Head-Gordon, M.; Replogle, E. S.; Pople, J. A. *GAUSSIAN 98*, Revision A.7; Gaussian, Inc., Pittsburgh PA, 1998.
19. Marcus, R. A. *J. Chem. Phys.* **1952**, *20*, 359.
20. Chang, A. H. H.; Mebel, A. M.; Yang, X. –M.; Lin, S.H.; Lee, Y. T. *J. Chem. Phys.* **1998**, *109*, 2748.
21. Roth, W. R.; Adamczak, O.; Breuckmann, R.; Lennartz, H. –W.; Boese, R. *Chem. Ber.* **1991**, *124*, 2499.
22. Davis, H. E.; Allinger, N. L.; Rogers, D. W. *J Org. Chem.* **1985**, *50*, 3601.
23. Riveros, J. M.; Ingeman, S.; Nibbering, N. M. M. *J Am. Chem. Soc.* **1991**, *113*, 1053.
24. Lichtenberger, D. L.; Renshaw, S. K.; Bullock, R. M. *J. Am. Chem. Soc.* **1993**, *115*, 3276.
25. Roth, W. R.; Adamczak, O.; Breuckmann, R.; Lennartz, H. W.; Boese, R. *Chem. Ber.* **1991**, *124*, 2499.
26. Zhang, X.; Chen, P. *J. Am. Chem. Soc.* **1992**, *114*,3147.
27. Bieri, G.; Burger, F.; Heilbronner, E.; Maier, J. P. *Helv. Chim. Acta.* **1977**, *60*, 2213.

Table 1: G3 Energies (E_0), Enthalpies (H_{298}), and Heats of Formation at 0K (ΔH_{f0}) and 298K (ΔH_{f298}) of Various Species Involved in the Dissociation of Phenylacetylene and Most of the Reactants and Products Cation.

Species	E_0 (hartree)	H_{298} (hartree)	ΔH_{f0} (kcal mol^{-1})	ΔH_{f298} (kcal mol^{-1})
1	-308.16140	-308.15395	79.7	79.0 (73.3 ± 0.4)[a]
2	-308.10034	-308.09309	118.0	115.2
3	-307.99015	-307.98267	187.2	184.5
4	-230.74575	-230.74005	112.3	110.9 (105.2 ± 2.4)[b]
5	-77.20691	-77.20282	98.4	98.6
6	-77.27595	-77.27226	55.1	55.1
7	-308.01781	-308.00948	169.8	167.7
8	-308.03215	-308.02413	160.8	158.5
9	-230.72181	-230.71474	127.3	126.7 (129.5)[c]
10	-230.61700	-230.60908	193.1	193.0
11	-229.49771	-229.49071	163.4 (160)[d]	164.8
12	-230.72249	-230.71521	126.9	126.4 (128.6)[c]
13	-230.61495	-230.60711	194.4	194.3
14	-230.71840	-230.71131	129.4	128.9
1$^+$	-307.83533	-307.82746	284.3	281.9
4$^+$	-230.38224	-230.37703	340.4	338.6
9$^+$	-230.38788	-230.38049	336.9	336.5
11$^+$	-229.14781	-229.14056	383.0	384.5
12$^+$	-230.38946	-230.38191	335.9	335.6
H_2	-1.16738	-1.16407		
TS1	-307.98983	-307.98239	187.4	184.7
TS2	-307.88971	-307.88163	250.2	247.9
TS3	-77.20549	-77.20149	99.3	99.5
TS4	-307.94548	-307.93721	215.2	213.0
TS5	-308.01759	-308.00999	170.0	167.4
TS6	-307.94728	-307.93907	214.1	211.9
TS7	-307.94588	-307.93627	215.0	213.6
TS8	-230.60421	-230.59711	201.1	200.5
TS9	-230.54980	-230.54227	235.3	235.0
TS10	-230.60145	-230.59421	202.8	202.4
TS11	-230.55879	-230.55120	229.6	229.3

[a] Experimental results from ref 22. [b] Experimental results from ref 23. [c] Experimental results from ref 21. [d] Experimental results from ref 14.

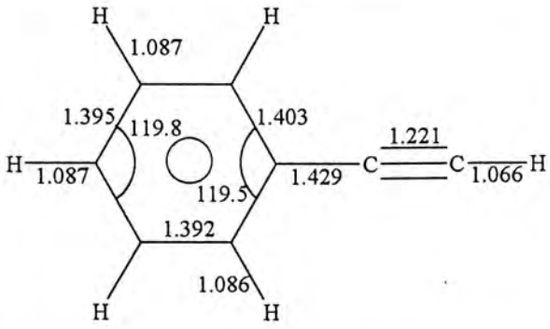

1 (C_{2V}, $^1A_1$)

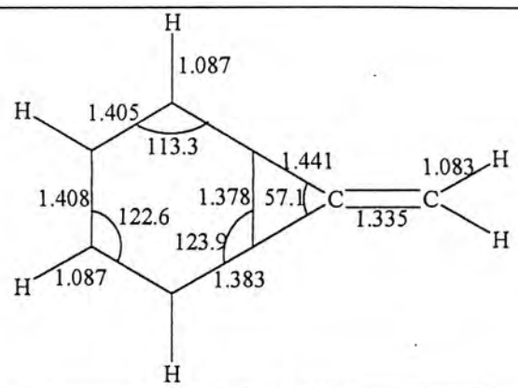

2 (C_{2V}, $^1A_1$)

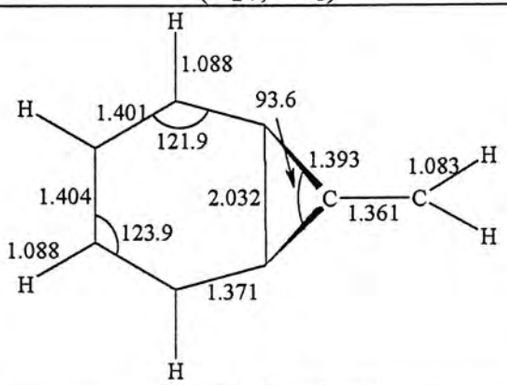

3 (C_S, $^3A''$)

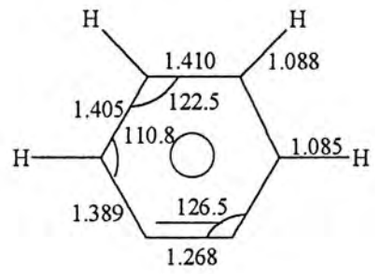

4 (C_{2V}, $^1A_1$)

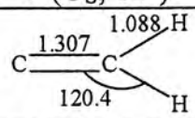

5 (C_{2V}, $^1A_1$)

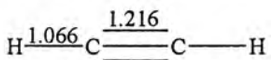

6 ($D_{\infty h}$, $^1\sum_g$)

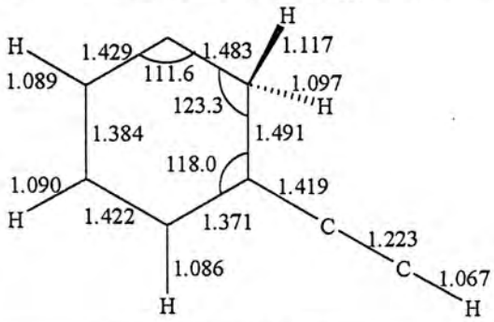

7 (C_1, ^1A)

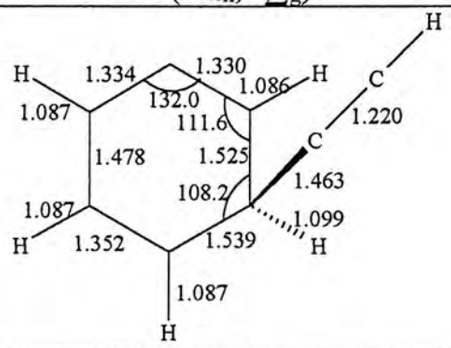

8 (C_1, ^1A)

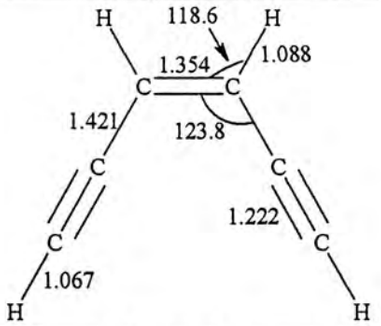

9 (C_{2V}, $^1A_1$)

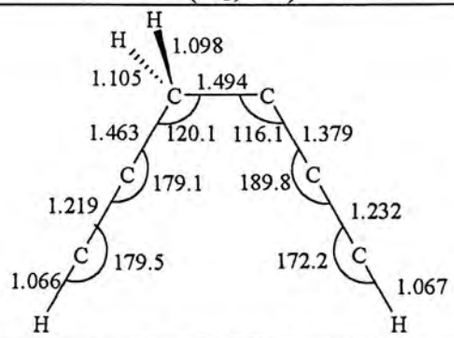

10 (C_1, ^1A)

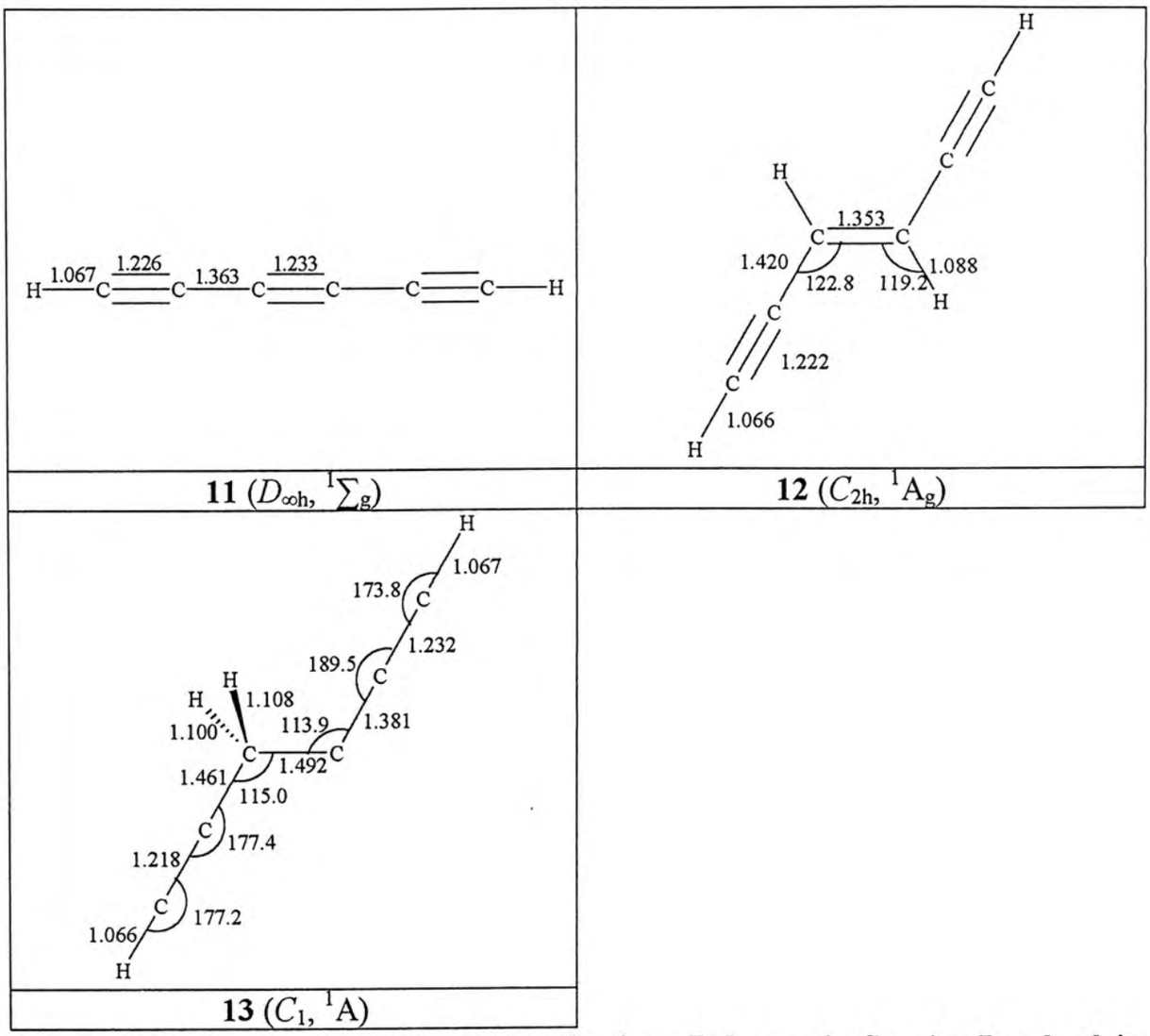

11 ($D_{\infty h}$, $^1\Sigma_g$) **12** (C_{2h}, ^1A_g)

13 (C_1, ^1A)

Figure 1. Structural Formulas of the Various Polyatomic Species Involved in This Work, along with Their Symmetry Point Groups and Electronic States.

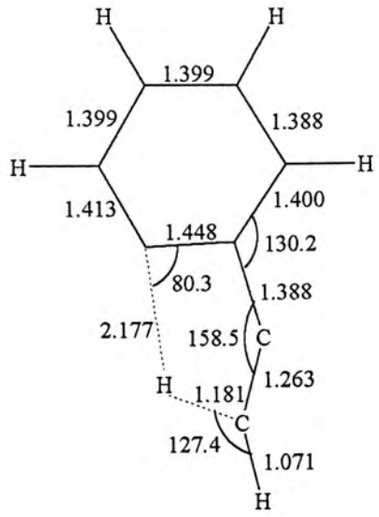

TS1 (C_1)

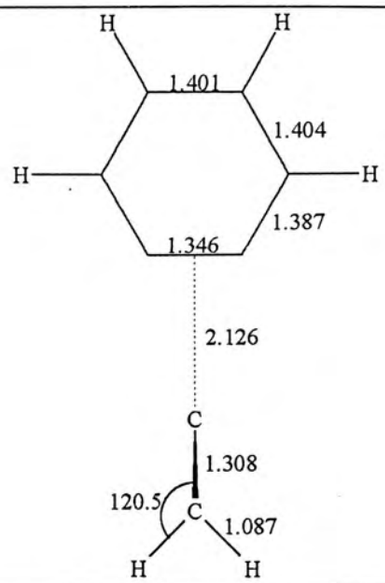

TS2 (C_S)

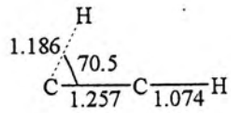

TS3 (C_S)

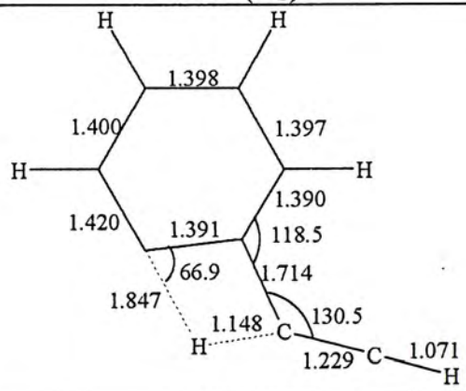

TS4 (C_S)

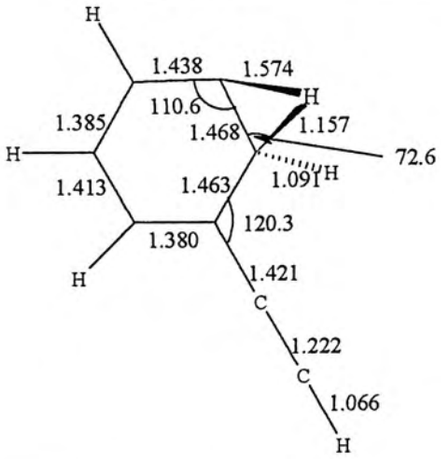

TS5 (C_1)

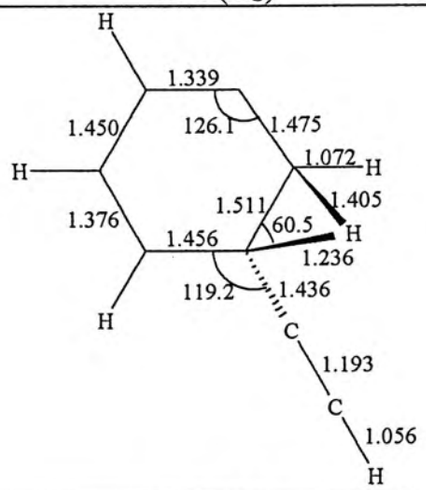

TS6 (C_1)

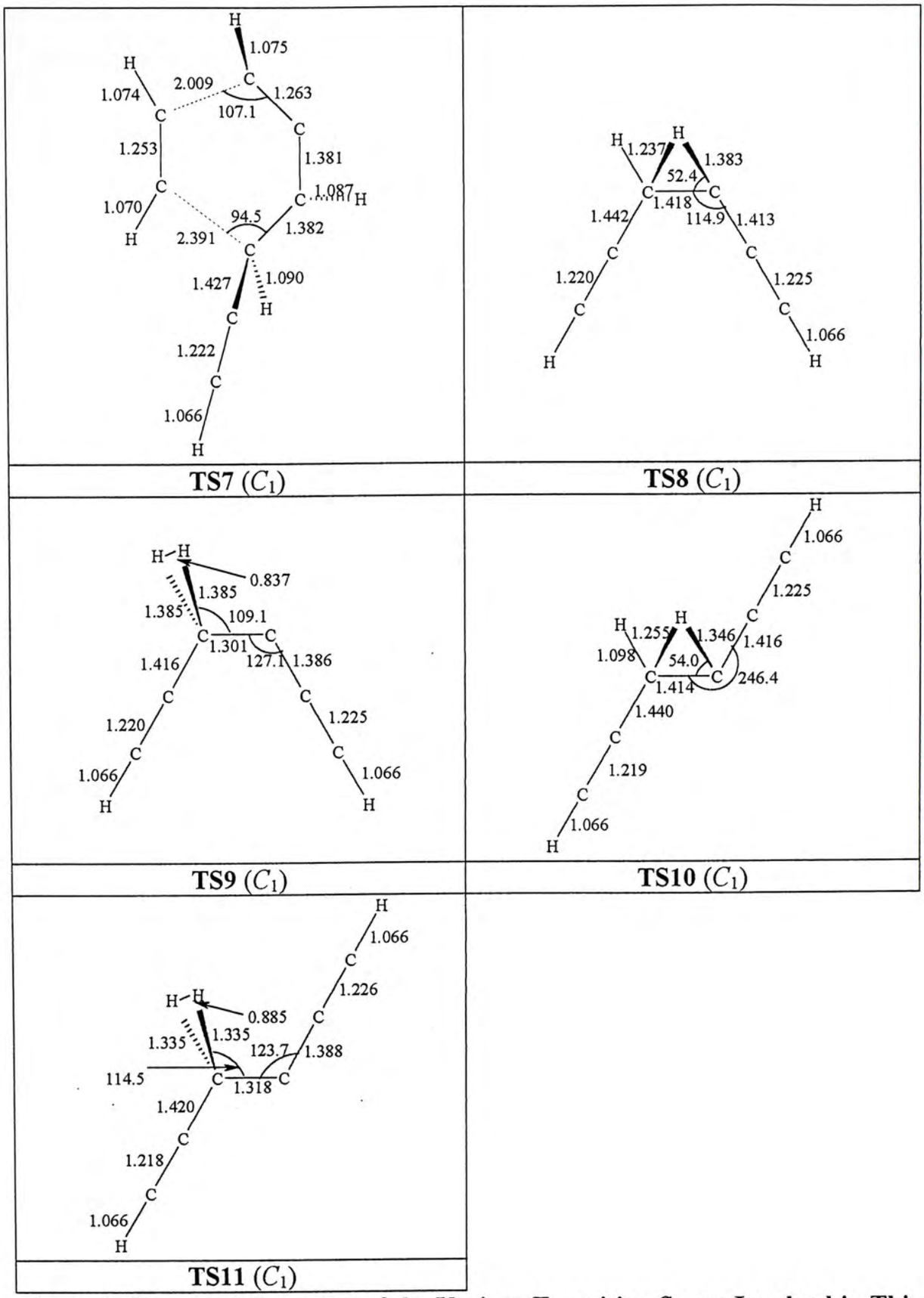

Figure 2. Structural Formulas of the Various Transition States Involved in This Work, along with Their Symmetry Point Groups.

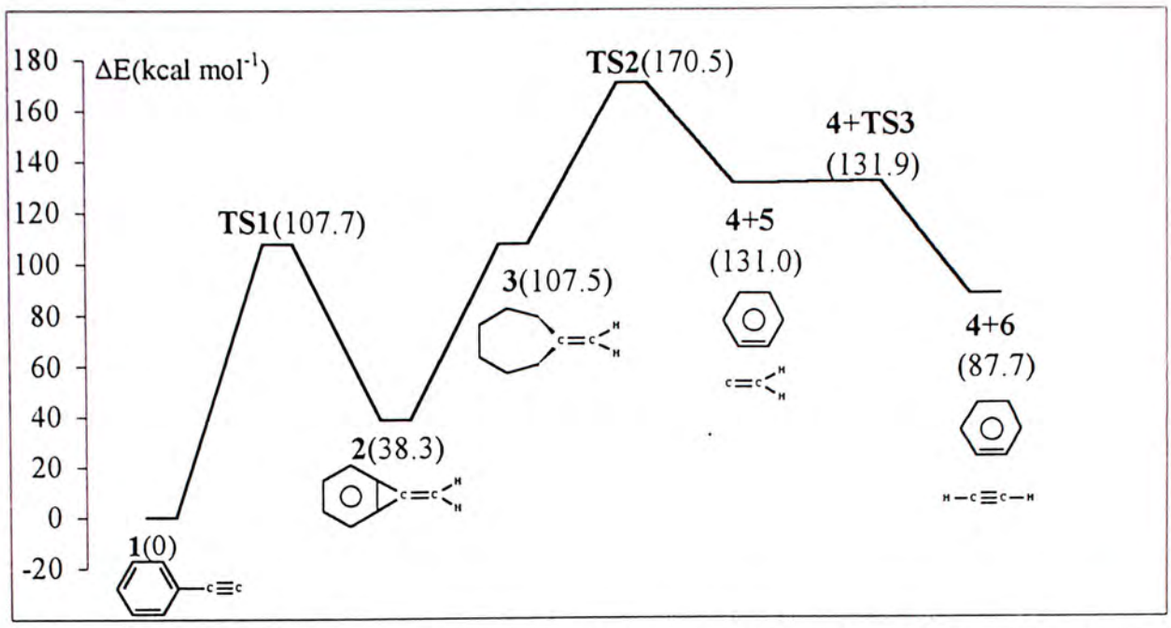

Figure 3. Potential Energy Surface Showing Possible Mechanism for the Formation of Benzyne and Acetylene from the Dissociation of Phenylacetylene.

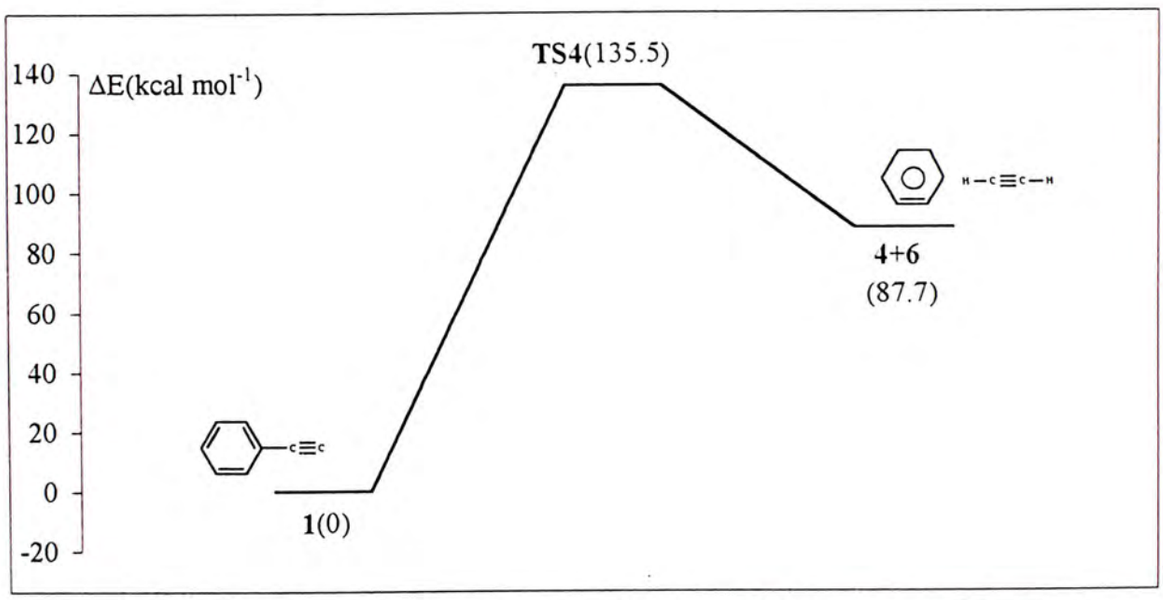

Figure 4. Potential Energy Surface Showing Possible One Step Mechanism for the Formation of Benzyne and Acetylene from the Dissociation of Phenylacetylene.

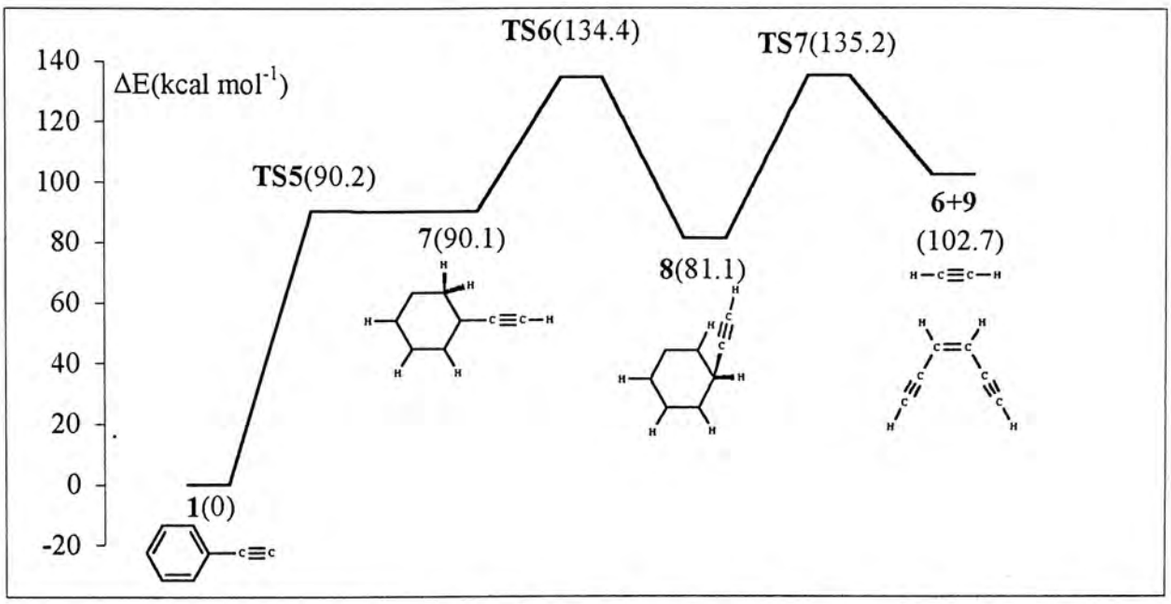

Figure 5. Potential Energy Surface Showing Possible Mechanism for the Formation of (*Z*)–3–Hexene–1,5–diyne and Acetylene from the Dissociation of Phenylacetylene.

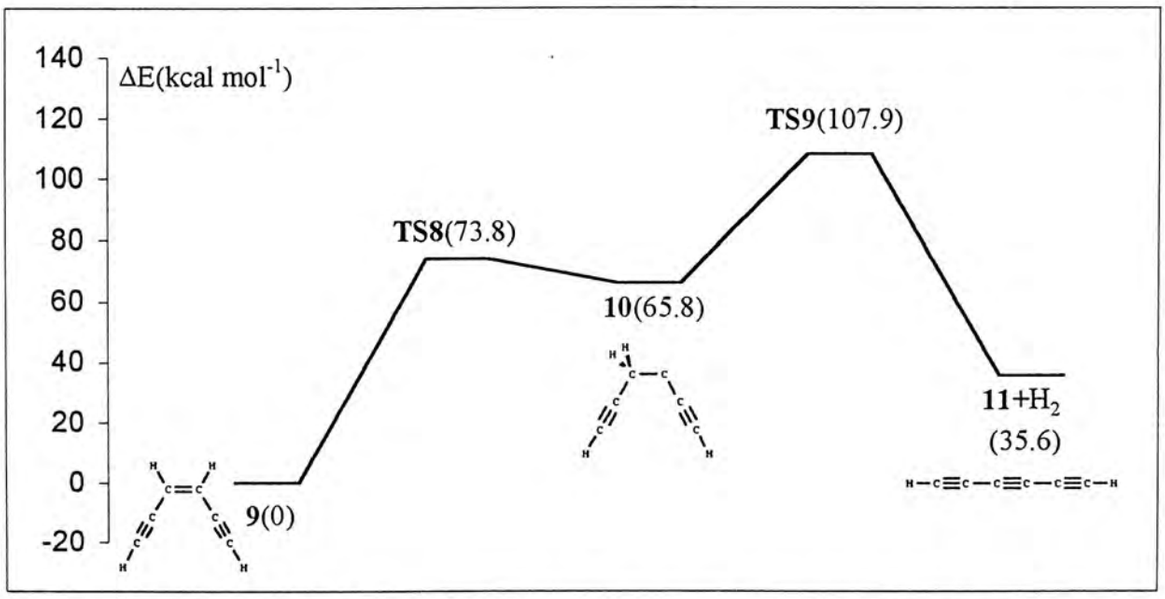

Figure 6. Potential Energy Surface Showing Possible Mechanism for the Formation of 1,3,5–Hexatriyne and Molecular Hydrogen from the Dissociation of (*Z*)–3–Hexene–1,5–diyne.

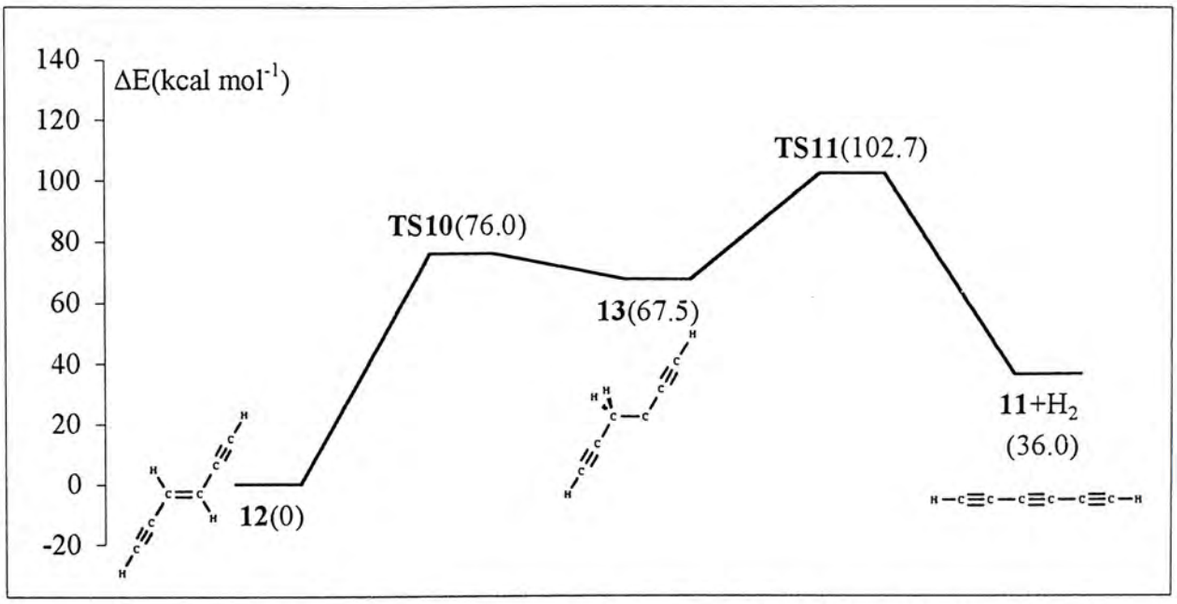

Figure 7. Potential Energy Surface Showing Possible Mechanism for the Formation of 1,3,5–Hexatriyne and Molecular Hydrogen from the Dissociation of (*E*)–3–Hexene–1,5–diyne.

Chapter 3

A Gaussian–3 Study of the Photoionization and Dissociative Photoionization Channels of Cyanoethylene

Abstract

We have carried out ab initio Gaussian–3 calculations to examine the energetics of the dissociative photoionization of cyanoethylene. Combining these results with the experimental photoionization data for ions $C_3H_2N^+$, C_3HN^+, C_3N^+, C_2HN^+, C_2N^+, C_3H^+, C_3^+, CH_2N^+, $C_2H_3^+$, $C_2H_2^+$, C_2H^+, C_2^+, CH_3^+, CH_2^+, CH^+, and C^+, obtained by our collaborators at the University of Science and Technology of China, we have established the dissociation channels of cyanoethylene. The dissociation channels are divided into two types: simple bond cleavage reactions and those involving transition structures and reaction barriers. However, the differences between the experimental and G3 results for the formation of C_3HN^+ and CH_2N^+ fragments are too large to be acceptable.

3.1 Introduction

The cyano group shares many properties with halogens and is frequently classified as a "pseudohalogen." However, the cyano group differs significantly from halogen atoms in that it possesses low–lying unoccupied π^* molecular orbital. This property causes conjugated π electron systems containing two or more cyano groups to have rather strongly bound anion states. Some of these compounds, for example, tetracyanoethylene (TCNE) and tetracyanoquinodimethane (TCNQ), are important constituents of "organic conductors" such as TTF–TCNQ,[1] where TTF is tetrathiafulvalene. In addition, the $R_2C{=}C(CN)_2$ group has been employed as the electron acceptor in a series of model compounds used to investigate long–range electron transfer.[2]

Cyanoethylene, also known as 2–propenenitrile, acrylonitrile, vinyl cyanide, etc, is a precursor used in the synthesis of the acrylic fibers, plastics, rubbers, and acrylamides. Recently, our collaborators, at the University of Science and Technology of China, performed an experimental study of photoionization and photodissociation of cyanoethylene by using vacuum ultraviolet (VUV) photons from Hefei synchrotron radiation source and a time–of–flight mass spectrometer (ITOF–MS). The photoionization mass spectrum and the photoionization efficiency (PIE) curves of all the observed ions from cyanoethylene were measured. The appearance potentials of all ions were obtained from their PIE curves. The experiment results show that a small stable molecule HCN is easily lost, thus the ion $C_2H_2^+$ is formed, and this is the chief dissociative photoionization channel. From these data, we have carried out Gaussian–3 (G3)[3] calculations to study the energetics of the dissociative photoionizations of cyanoethylene and attempt to establish the possible dissociation channels.

3.2 Computational Method

The computational model we employed was the Gaussian–3 (G3)[3] level of theory, details of which have already been described in Section 2.2. All of the calculations were carried out on DEC 900au workstations using the Gaussian 98 package of programs.[4]

3.3 Results and Discussion

All the appearance energies (AEs) of the fragments $C_3H_2N^+$, C_3HN^+, C_3N^+, C_2HN^+, C_2N^+, C_3H^+, C_3^+, CH_2N^+, $C_2H_3^+$, $C_2H_2^+$, C_2H^+, C_2^+, CH_3^+, CH_2^+, CH^+, and C^+, measured by our collaborators, for the photoionization and dissociative photoionizations of cyanoethylene, are listed in Table 1. The structural formulas of the polyatomic species involved in this work, along with their symmetry point groups, are shown in Figure 1. The calculated G3 energies (E_0), enthalpies (H_{298}) and standard heats of formation at 0 K (ΔH_{f0}) and 298 K (ΔH_{f298}) of all the species involved in the dissociation of cyanoethylene (**1**) and its cation (**2**) are listed in Table 2. Based on the E_0(G3) values of **1** and **2** in Table 1, the IE of cyanoethylene is calculated to be 10.95 eV, which is in good agreement with the result found in the experiment, 10.85 eV.

3.3.1 Bond Cleavage Reactions. This section summarizes the dissociation of **2**, which entails only bond cleavage(s), i.e., involving no transition states.

$$C_3H_3N^+ (\mathbf{2}) \xrightarrow{\Delta E_1} C_3N^+ (\mathbf{3}) + H_2 + H \qquad (1)$$

$$\Delta E_1 = AE(C_3N^+) - IE(C_3H_3N) = 11.80 \text{ eV}$$

$$C_3H_3N^+ (\mathbf{2}) \xrightarrow{\Delta E_2} HC_2N^+ (\mathbf{4}) + C + H_2 \qquad (2)$$

$$\Delta E_2 = AE(HC_2N^+) - IE(C_3H_3N) = 10.24 \text{ eV}$$

$$C_3H_3N^+ (\mathbf{2}) \xrightarrow{\Delta E_3} C_2N^+ (\mathbf{5}) + CH (\mathbf{6}) + H_2 \qquad (3)$$

$$\Delta E_3 = AE(C_2N^+) - IE(C_3H_3N) = 12.44 \text{ eV}$$

$$C_3H_3N^+ (\mathbf{2}) \xrightarrow{\Delta E_4} C_3H^+ (\mathbf{7}) + N + 2H \qquad (4)$$

$$\Delta E_4 = AE(C_3H^+) - IE(C_3H_3N) = 13.12 \text{ eV}$$

$$C_3H_3N^+ (\mathbf{2}) \xrightarrow{\Delta E_5} C_3^+ (\mathbf{8}) + N + 3H \qquad (5)$$

$$\Delta E_5 = AE(C_3^+) - IE(C_3H_3N) = 20.84 \text{ eV}$$

$$C_3H_3N^+ (\mathbf{2}) \xrightarrow{\Delta E_6} C_2H_3^+ (\mathbf{9}) + CN (\mathbf{10}) \qquad (6)$$

$$\Delta E_6 = AE(C_2H_3^+) - IE(C_3H_3N) = 3.27 \text{ eV}$$

$$C_3H_3N^+ \textbf{(2)} \xrightarrow{\Delta E_7} C_2H_2^+ \textbf{(11)} + HCN \textbf{(12)} \quad (7)$$

$$\Delta E_7 = AE(C_2H_2^+) - IE(C_3H_3N) = 2.10 \text{ eV}$$

$$C_3H_3N^+ \textbf{(2)} \xrightarrow{\Delta E_8} C_2H^+ \textbf{(13)} + HCN \textbf{(12)} + H \quad (8)$$

$$\Delta E_8 = AE(C_2H^+) - IE(C_3H_3N) = 10.61 \text{ eV}$$

$$C_3H_3N^+ \textbf{(2)} \xrightarrow{\Delta E_9} C_2^+ \textbf{(14)} + HCN \textbf{(12)} + 2H \quad (9)$$

$$\Delta E_9 = AE(C_2^+) - IE(C_3H_3N) = 14.10 \text{ eV}$$

$$C_3H_3N^+ \textbf{(2)} \xrightarrow{\Delta E_{10}} CH_3^+ \textbf{(15)} + CN \textbf{(10)} + C \quad (10)$$

$$\Delta E_{10} = AE(CH_3^+) - IE(C_3H_3N) = 10.24 \text{ eV}$$

$$C_3H_3N^+ \textbf{(2)} \xrightarrow{\Delta E_{11}} CH_2^+ \textbf{(16)} + HCN \textbf{(12)} + C \quad (11)$$

$$\Delta E_{11} = AE(CH_2^+) - IE(C_3H_3N) = 9.88 \text{ eV}$$

$$C_3H_3N^+ \textbf{(2)} \xrightarrow{\Delta E_{12}} CH^+ \textbf{(17)} + HCN \textbf{(12)} + C + H \quad (12)$$

$$\Delta E_{12} = AE(CH^+) - IE(C_3H_3N) = 14.61 \text{ eV}$$

$$C_3H_3N^+ \textbf{(2)} \xrightarrow{\Delta E_{13}} C^+ \textbf{(18)} + HCN \textbf{(12)} + C + 2H \quad (13)$$

$$\Delta E_{13} = AE(C^+) - IE(C_3H_3N) = 18.93 \text{ eV}$$

In the above calculations, the G3 IE of **1** is used. The above dissociation energies (ΔE_1 to ΔE_{13}), along with those calculated by the G3 method (using the data tabulated in Table 2), are given in Table 3 for easy comparison. It is seen that the G3 dissociation energies of most channels are in good agreement, i.e., within ±0.15 eV, with the experimental results. The only exceptions are channels (4) and (11). The difference between the experimental and G3 ΔE_4 is 0.21 eV, which may still be viewed as acceptable. However, the difference between the experimental and G3 ΔE_{11} is 0.29 eV, which is not expected for G3 results of systems with this size. It is believed that this error may arise from kinetic shifts, as suggested by Ma et al [6] and Chiang and co–workers [7] in their studies of other chemical systems.

3.3.2 Dissociation Channels Involving Transition Structures. In this section, we consider the dissociations of the cyanoethylene cation which involve transition structures.

$$C_3H_3N^+ \textbf{(2)} \xrightarrow{\Delta E_{14}} C_3H_2N^+ \textbf{(19)} + H \qquad (14)$$

$$\Delta E_{14} = AE(C_3H_2N^+) - IE(C_3H_3N) = 2.44 \text{ eV}$$

The schematic energy profile of this reaction is shown in Figure 2. In order to dissociate into $C_3H_2N^+$ (**19**) and hydrogen atom, $C_3H_3N^+$ (**2**) first undergoes hydrogen transfer via **TS1** to form intermediate **20**. Cation **20** dissociates into **19** and hydrogen atom via **TS2**. The G3 barrier of this reaction is 2.66 eV, in fair agreement with the experimental dissociation energy, 2.44 eV.

$$C_3H_3N^+ \textbf{(2)} \xrightarrow{\Delta E_{15}} C_3HN^+ \textbf{(21)} + H_2 \qquad (15)$$

$$\Delta E_{15} = AE(C_3HN^+) - IE(C_3H_3N) = 3.47 \text{ eV}$$

The energy profile of this reaction is given in Figure 3. In this figure, we see that **2** undergoes hydride shift via **TS3** to form intermediate **22**. Then **22** can dissociate to linear cation $HCCCN^+$ (**21**) and H_2 via **TS4**. The G3 barrier of this reaction is 2.75 eV. The difference between the experimental and G3 ΔE_{15} is 0.72 eV, which is not acceptable. However, it is noteworthy that the G3 ΔE is lower than that for the experimental result. It is possible the error arises from the experiment, and we have asked our collaborators to check the experimental data again.

$$C_3H_3N^+ \textbf{(2)} \xrightarrow{\Delta E_{16}} CH_2N^+ \textbf{(23)} + C_2H \textbf{(24)} \qquad (16)$$

$$\Delta E_{16} = AE(CH_2N^+) - IE(C_3H_3N) = 3.47 \text{ eV}$$

The energy profile of this reaction is shown in Figure 3. As in reaction (14), cation **20** is first formed via **TS1**. Then **20** rearranges to form **22** via **TS5**. Cation **22** then undergoes bond cleavage reaction to produce linear products $HCNH^+$ (**23**) and CCH (**24**) via **TS6**. The G3 barrier of this reaction is 2.80 eV. The difference between ΔE_{16} and experimental result is also quite large, and once again the G3 ΔE_{16} is smaller than the experimental result. We have now asked our experimental collaborators to check the data of this reaction again.

3.4 Conclusions

By carrying out ab initio G3 calculations, we have investigated the energetics of the photoionization and dissociative photoionizations of cyanoethylene. Combining

these results with the experimental photoionization data of various fragments obtained by our colleagues in China, we are able to establish the dissociation channels for the formation of the following ions: $C_3H_2N^+$, C_3N^+, C_2HN^+, C_2N^+, C_3H^+, C_3^+, $C_2H_3^+$, $C_2H_2^+$, C_2H^+, C_2^+, CH_3^+, CH_2^+, CH^+, and C^+. These ions are produced from two types of dissociation channels: simple bond cleavage reactions and those involving transition structures and reaction barriers. However, the differences between the experimental and G3 results for the formation of C_3HN^+ and CH_2N^+ fragments are too large to be acceptable.

3.5 References

1. Coleman, L. B.; Cohen, J. J.; Sandman, D. J.; Yamagishi, F. G.; Garito, A. F.; Heeger, A. J. *Solid St. Commun.* **1973**, *12*, 1125.
2. Verhoeven, J. W.; Paddon-Row, M. N.; Hush, N. S.; Oevering, H.; Heppener, M. *Pure Appl. Chem.* **1986**, *58*, 1285.
3. Curtiss, L. A.; Raghavachari, K.; Redfern, P. C.; Rassolov, V.; Pople, J. A. *J. Chem. Phys.* **1998**, *109*, 7764.
4. Frisch, M. J.; Trucks, G. W.; Schlegel, H. B.; Scuseria, G. E.; Robb, M. A.; Cheeseman, J. R.; Zakrzewski, V. G.; Montgogery, J. A.; Jr.; Stratmann, R.E.; Burant, J. C.; Dapprich, S.; Millam, J. M.; Daniels, A. D.; Kudin, K. N.; Strain, M. C.; Farkas, O.; Tomasi, J.; Barone, V.; Cossi, M.; Cammi, R.; Mennucci, B.; Pomelli, C.; Adamo, C.; Clifford, S.; Ochterski, J.; Petersson, G. A.; Ayala, P. Y.; Cui, Q.; Morokuma, K.; Malick, D. K.; Rabuck, A. D.; Raghavachari, K.; Foresman, J. B.; Cioslowski, J.; Ortiz, J. V.; Baboul, A. G.; Stefanov, B. B.; Liu, G.; Liashenko, A.; Piskorz, P.; Komaromi, I.; Gomperts, R.; Martin, R. L.; Fox, D. J.; Keith, T.; Al-Laham, M. A.; Peng, C. Y.; Nanayakkara, A.; Gonzalez, C.; Challacombe, M.; Gill, P. M. W.; Johnson, B.; Chen, W.; Wong, M. W.; Andres, J. L.; Gonzalez, C.; Head-Gordon, M.; Replogle, E. S.; Pople, J. A. *GAUSSIAN 98*, Revision A.7; Gaussian, Inc., Pittsburgh PA, 1998.
5. Hall, H. K., Jr.; Baldt, J. H. *J. Am. Chem. Soc.* **1971**, *93*, 140.
6. Ma, Z.–X.; Liao, C.–L.; Ng, C. Y.; Cheung, Y.–S.; Li, W.–K.; Baer, T. *J. Chem. Phys.* **1994**, *100*, 4870.
7. Chiang, S.–Y.; Ma, C.–I.; Shr, D.– J. *J. Chem. Phys.* **1999**, *110*, 9056.

Table 1: Appearance energies (eV) Measured in the Dissociative Photoionizations of Cyanoethylene

m/e	*Ion*	AE	m/e	*Ion*	AE
52	$C_3H_2N^+$	13.39	27	$C_2H_3^+$	14.22
51	C_3HN^+	14.42	26	$C_2H_2^+$	13.05
50	C_3N^+	22.75	25	C_2H^+	21.56
39	C_2HN^+	21.19	24	C_2^+	25.05
38	C_2N^+	23.39	15	CH_3^+	21.19
37	C_3H^+	24.07	14	CH_2^+	20.83
36	C_3^+	31.79	13	CH^+	25.56
28	CH_2N^+	14.42	12	C^+	29.88

Table 2: G3 Energies (E_0), Enthalpies (H_{298}), and Standard Heats of Formation at 0K (ΔH_{f0}) and 298K (ΔH_{f298}) of Various Species Involved in the Dissociation of Cyanoethylene and Its Cation.

species	E_0(G3) (hartree)	H_{298}(G3) (hartree)	ΔH_{f0}(G3) (kj mol^{-1})	ΔH_{f298}(G3) (kj mol^{-1})
C_3H_3N (**1**)	-170.71537	-170.71024	194.0	188.5 (179.7)[a]
$C_3H_3N^+$ (**2**)	-170.31287	-170.30743	1250.8	1246.1
C_3N^+ (**3**)	-168.21557	-168.21043	2163.1	2170.2
C_2HN^+ (**4**)	-130.94671	-130.94174	1516.0	1519.2
C_2N^+ (**5**)	-130.22855	-130.22451	1870.2	1875.1
CH (**6**)	-38.45831	-38.45501	587.0	590.7
C_3H^+ (**7**)	-114.27228	-114.26767	1593.1	1599.0
C_3^+ (**8**)	-113.48375	-113.47951	2132.1	2141.1
$C_2H_3^+$ (**9**)	-77.51350	-77.50923	1138.2	1135.4
CN (**10**)	-92.67345	-92.67015	443.2	446.9
$C_2H_2^+$ (**11**)	-76.85669	-76.85252	1331.3	1332.4
HCN (**12**)	-93.37543	-93.37196	131.5	131.5
C_2H^+ (**13**)	-76.04292	-76.03954	1936.4	1939.7
C_2^+ (**14**)	-75.41717	-75.41386	2048.0	2055.3
CH_3^+ (**15**)	-39.43058	-39.42677	1097.0	1093.7
CH_2^+ (**16**)	-38.73616	-38.73233	1388.8	1389.8
CH^+ (**17**)	-38.06731	-38.06401	1613.5	1617.3
C^+ (**18**)	-37.41571	-37.41335	1792.9	1798.4
$C_3H_2N^+$ (**19**)	-170.32882	-170.32334	1208.9	1204.3
20	-169.76573	-169.76003	1155.9	1156.1
HC_3N^+ (**21**)	-169.04742	-169.04218	1510.5	1513.7
22	-170.26573	-170.25930	1374.6	1372.5
CH_2N^+ (**23**)	-93.64496	-93.64131	955.3	951.5
CCH (**24**)	-76.56469	-76.56093	566.5	570.8
25	-170.29295	-170.28723	1303.1	1299.1
H	-0.50100			
N	-54.56434			
C	-37.82772			
H_2	-1.16737	-1.16407		
TS1	-170.21504	-170.20967	1507.7	1502.8
TS2	-170.25125	-170.24563	1412.6	1408.4
TS3	-170.25991	-170.25438	1389.8	1385.4
TS4	-170.21166	-170.20510	1516.5	1514.8
TS5	-170.25029	-170.24453	1415.1	1411.3
TS6	-170.21011	-170.20336	1520.6	1519.3

[a] Experimental value from ref 5.

Table 3: Experimental and Calculated Energies (eV) of the Dissociation of Cyanoethylene Cation.

Dissociation reaction	ΔE(exp)	ΔE(G3) or reaction barrier
Simple bond cleavage reactions		
(1) $C_3H_3N^+$ (**2**) ⟶ C_3N^+ (**3**) + H_2 + H	11.80	11.67
(2) $C_3H_3N^+$ (**2**) ⟶ HC_2N^+ (**4**) + C + H_2	10.24	10.10
(3) $C_3H_3N^+$ (**2**) ⟶ C_2N^+ (**5**) + CH (**6**) + H_2	12.44	12.48
(4) $C_3H_3N^+$ (**2**) ⟶ C_3H^+ (**7**) + N + 2H	13.12	12.91
(5) $C_3H_3N^+$ (**2**) ⟶ C_3^+ (**8**) + N + 3H	20.84	20.73
(6) $C_3H_3N^+$ (**2**) ⟶ $C_2H_3^+$ (**9**) + CN (**10**)	3.27	3.43
(7) $C_3H_3N^+$ (**2**) ⟶ $C_2H_2^+$ (**11**) + HCN (**12**)	2.10	2.20
(8) $C_3H_3N^+$ (**2**) ⟶ C_2H^+ (**13**) + HCN (**12**) + H	10.61	10.71
(9) $C_3H_3N^+$ (**2**) ⟶ C_2^+ (**14**) + HCN (**12**) + 2H	14.10	14.10
(10) $C_3H_3N^+$ (**2**) ⟶ CH_3^+ (**15**) + CN (**10**) + C	10.24	10.37
(11) $C_3H_3N^+$ (**2**) ⟶ CH_2^+ (**16**) + HCN (**12**) + C	9.88	10.17
(12) $C_3H_3N^+$ (**2**) ⟶ CH^+ (**17**) + HCN (**12**) + C + H	14.61	14.73
(13) $C_3H_3N^+$ (**2**) ⟶ C^+ (**18**) + HCN (**12**) + C + 2H	18.93	18.83
Reactions involving transition structures		
(14) $C_3H_3N^+$ (**2**) ⟶ $C_3H_2N^+$ (**19**) + H	2.44	2.66
(15) $C_3H_3N^+$ (**2**) ⟶ C_3HN^+ (**21**) + H_2	3.47	2.75
(16) $C_3H_3N^+$ (**2**) ⟶ CH_2N^+ (**23**) + CCH (**24**)	3.47	2.80

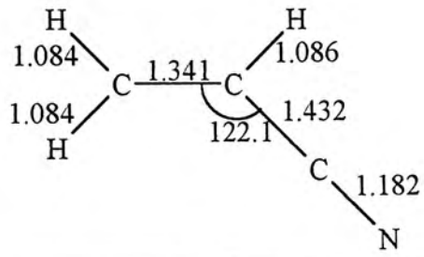	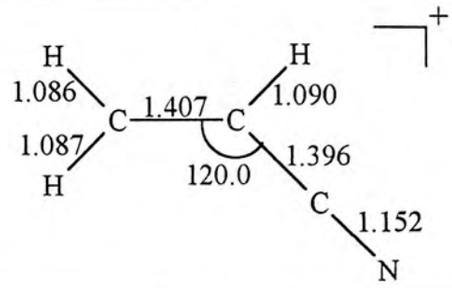
1, C_s	**2**, C_s
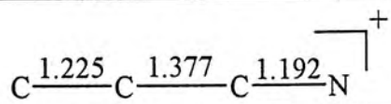	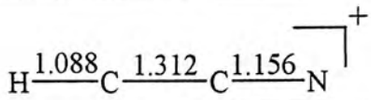
3, $C_{\infty v}$	**4**, $C_{\infty v}$
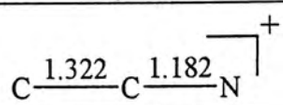	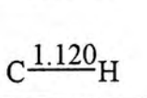
5, $C_{\infty v}$	**6**, $C_{\infty v}$
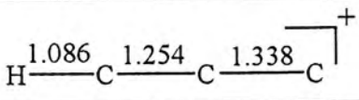	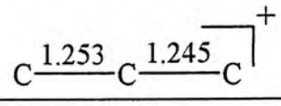
7, $C_{\infty v}$	**8**, $C_{\infty v}$
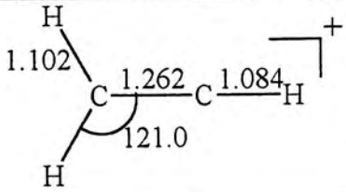	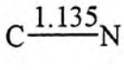
9, C_{2v}	**10**, $C_{\infty v}$
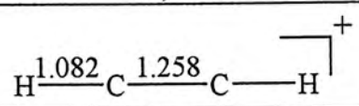	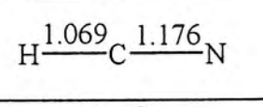
11, $D_{\infty h}$	**12**, $C_{\infty v}$
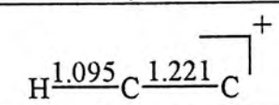	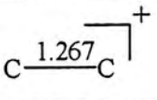
13, $C_{\infty v}$	**14**, $D_{\infty h}$
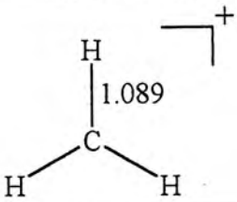	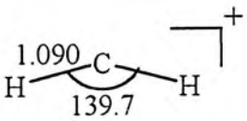
15, D_{3h}	**16**, C_{2v}
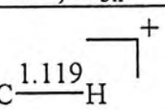	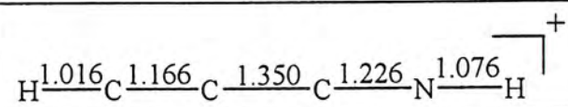
17, $C_{\infty v}$	**19**, $C_{\infty v}$

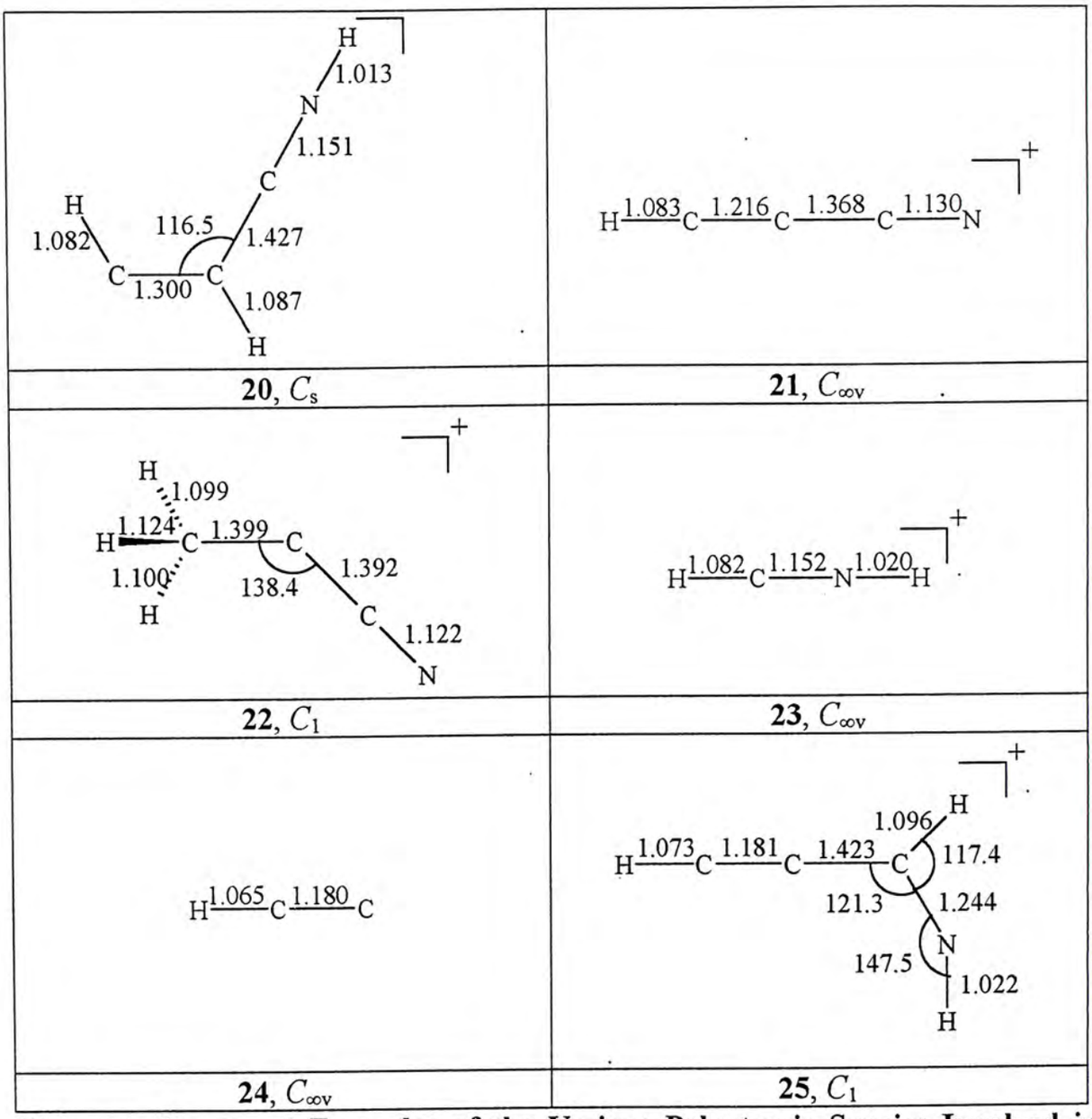

Figure 1. Structural Formulas of the Various Polyatomic Species Involved in This Work, along with Their Symmetry Point Groups.

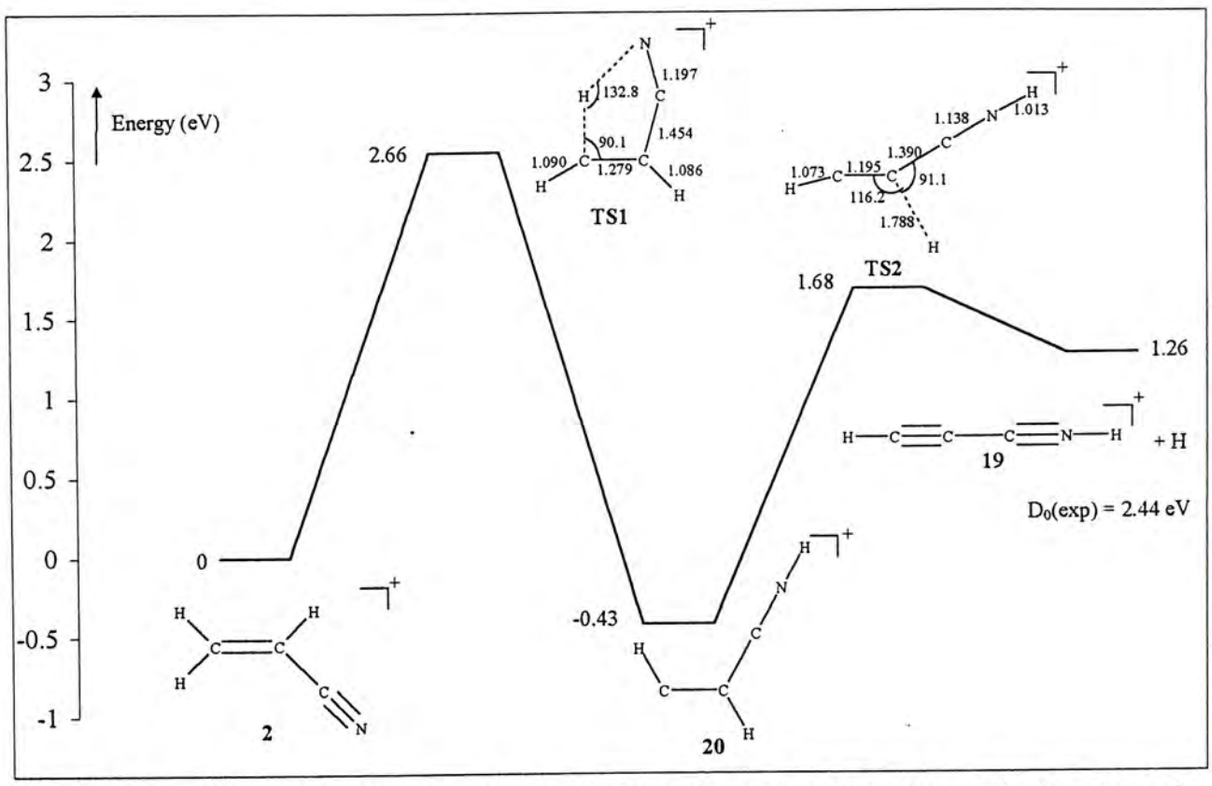

Figure 2. Potential Energy Surface Showing the Possible Mechanism for Dissociation $C_3H_3N^+ \rightarrow C_3H_2N^+ + H$.

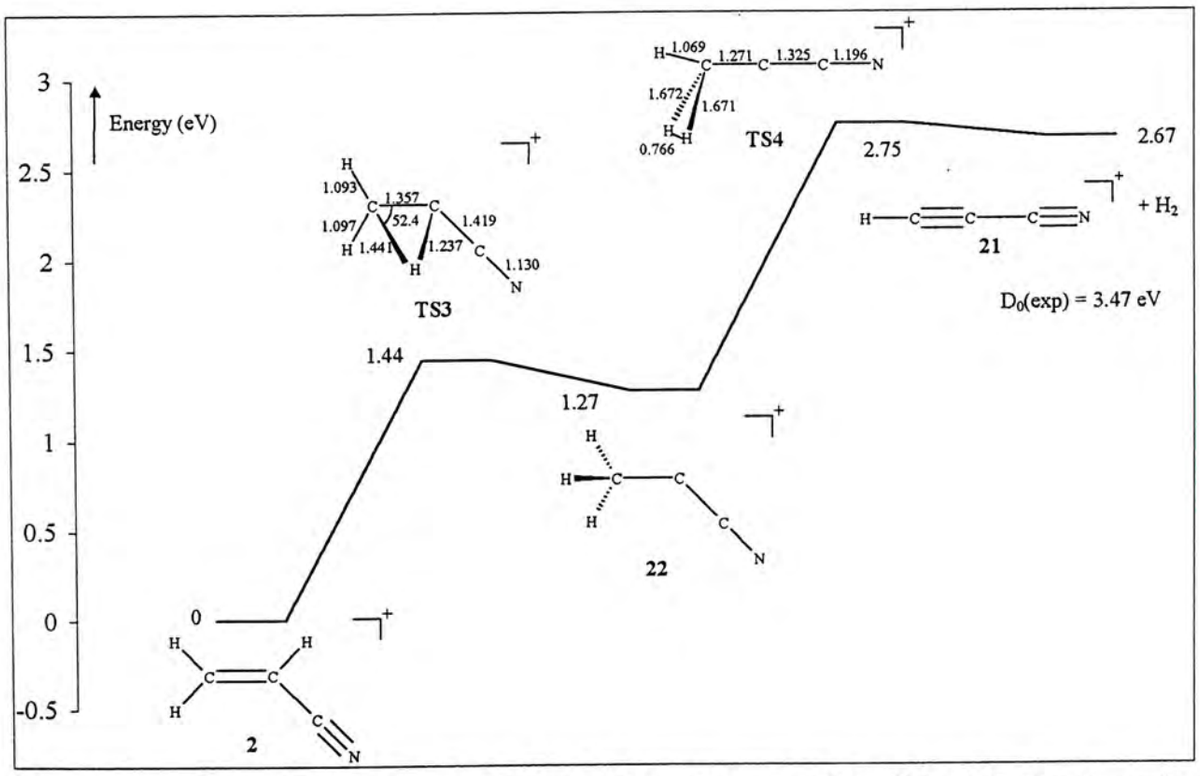

Figure 3. Potential Energy Surface Showing the Possible Mechanism for Dissociation $C_3H_3N^+ \rightarrow C_3HN^+ + H_2$.

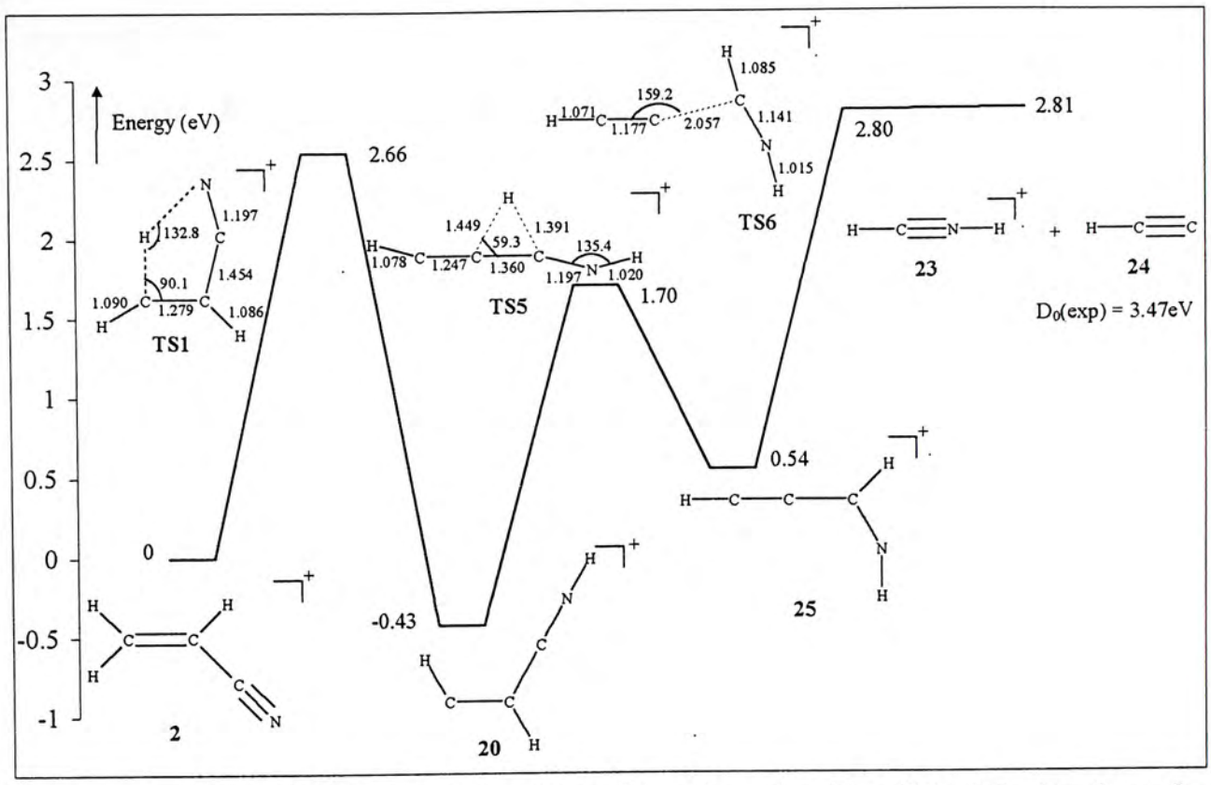

Figure 4. Potential Energy Surface Showing the Possible Mechanism for Dissociation $C_3H_3N^+ \rightarrow CH_2N^+ + CCH$.

Chapter 4

A Gaussian–2 Study of Structures, Energetics, and Reactions of $C_2H_3S^-$ Anions

Abstract

A computational study on the structures, energetics, and reactions of the $C_2H_3S^-$ isomers has been carried out. The computational model used is a modified version of the ab initio Gaussian–2 method. This modified model, called G2++, is designed specifically for anionic systems. Twelve $C_2H_3S^-$ isomers/conformers have been identified. The thioformylmethyl anion (**1**$^-$) is the most stable isomer and its ΔH_{f0} is –0.3 kJ mol^{-1}. The next two lowest energy isomers are the thioacetyl anion (**2**$^-$) and 1–thiovinyl anion (**3**$^-$/**4**$^-$). They are 157.2 and 175.8/166.9 kJ mol^{-1} less stable than **1**$^-$, respectively. A cyclic anion (**12**$^-$) is the least stable and its ΔH_{f0} is 444.6 kJ mol^{-1}. The G2++ proton affinities of **1**$^-$ and thiirane anion (**11**$^-$) are 1446.0 and 1642.2 kJ mol^{-1}, respectively, which are in excellent agreement with the experimental data. Other isomers/conformers identified include CH_2SCH^- (**9**$^-$/**10**$^-$), and 2–thiovinyl anion (**5**$^-$/**6**$^-$/**7**$^-$/**8**$^-$). Four anions (**2**$^-$, **4**$^-$, **5**$^-$, **11**$^-$) can be rearranged from **1**$^-$, with barriers ranging from 246.8 to 274.2 kJ mol^{-1}. Transition structures (TSs) for ring opening processes **11**$^-$ → **10**$^-$ and **12**$^-$ → **7**$^-$, and for rearrangements **8**$^-$ → **4**$^-$ and **2**$^-$ → **3**$^-$ are also found. In addition, rotational TSs **9**$^-$ → **10**$^-$, **5**$^-$ → **7**$^-$, **6**$^-$ → **8**$^-$, and **4**$^-$ → **3**$^-$ are also located.

4.1 Introduction

Gaussian–n theoretical procedures, Gaussian–1 (G1),[1] Gaussian–2 (G2),[2] and Gaussian–3 (G3),[3] as well as their variants are reliable methods to reproduce thermochemical data for a whole range of organic and inorganic species. More and more results are reproduced successfully by employing Gaussian–n method. So these methods have become important tools to estimate heats of formation (ΔH_f), ionization energies, proton affinities (PAs), and electron affinities (EAs) of various species.

Sulphur is the seventh most abundant element in the universe, and the eighth most abundant constituent of man. Organosulphur compounds have thus attracted the attention of chemists for years.[4] In our recent publications we have reported G2/G3 studies of $C_2H_3S^{\bullet}/C_2H_3S^+$ systems[5] and $C_2H_5S^{\bullet}/C_2H_5S^+/C_2H_5S^-$ systems.[6-11] It has been shown that the G2 and G3 methods can also be applied to sulphur containing systems and accurate results can be obtained. However, there have only a few studies of $C_2H_3S^-$ ions. To our knowledge, except the study of thiirane anion and thioformylmethyl anion,[12] no recent study on the $C_2H_3S^-$ ions are available. In our previous studies on $C_2H_3S^{\bullet}/C_2H_3S^+$ systems[5], 14 $C_2H_3S^{\bullet}$ isomers/conformers had been identified and 17 $C_2H_3S^+$ were found. In the present work, we investigate theoretically the structures and energetics of various $C_2H_3S^-$ isomers/conformers as well as the pathways of their isomerization reactions. Based on the results calculated for different $C_2H_3S^-$ ions, we can also compile the EAs of $C_2H_3S^{\bullet}$ radicals. In addition, we also report the calculated heats of formation at 0 K (ΔH_{f0}) and 298 K (ΔH_{f298}) for all the isomers/conformers.

4.2 Computational Method

All calculations were carried out on DEC 900au workstations using the Gaussian 98 packages of programs.[13] The computational model used is a modified Gaussian–2 (called G2++)[14] level of theory. In the G2++ model, all the structures are optimized at MP2(Full)/6-31++G(d) level with diffuse functions included on both heavy and hydrogen atoms. In the energy calculations, some modifications have been made on the original G2 single–points:[2] QCISD(T)/6–311G(d,p), MP4/6–311G(d,p), MP4/6–311++G(d,p) [with additional diffuse functions for hydrogen atom], MP4/6–311G(2df,p), and MP2/6–311++(3df,2p) [with additional

diffuse functions for hydrogen atom]. Higher–level correction (HLC) is added to account for the remaining basis set deficiencies: HLC = $-5.03 \times 10^{-3} n_{\beta} - 0.18 \times 10^{-3} n_{\alpha}$. All the equilibrium and transition structures have been characterized by vibrational frequencies calculations. A scaling factor of 0.972 is applied to the MP2(Full)/6–31++G(d) frequencies for the zero–point vibrational energy corrections. All transition structures (TSs) have been characterized by intrinsic reaction coordinate calculations.

The G2++ heats of formation at temperature T (ΔH_{fT}) in this work have been calculated in the following manner. For molecule AB, its G2++ ΔH_{fT} was calculated from the G2++ heat of reaction $\Delta H_{rT}(A + B \rightarrow AB)$ and the respective experimental $\Delta H_{fT}(A)$ and $\Delta H_{fT}(B)$ for elements A and B. In the calculations of ΔH_{rT} for anions, we set the ΔH_{rT} value of a free electron to be zero.

Finally, it is noted that population analyses (NBO)[15] for various anions have also been carried out at the MP2(Full)/6–31++G(d) level.

4.3 Results and Discussion

In our notations, numerals **1**$^-$, **2**$^-$,..., etc. refer to stable $C_2H_3S^-$ ions, while $C_2H_3S^{\bullet}$ radicals are denoted as **1**, **2**,..., etc. In addition, notation such as **1-2**$^-$ refers to the TS connecting **1**$^-$ and **2**$^-$. At the MP2(Full)/6–31++G(d) level, twelve $C_2H_3S^-$ isomers/conformers are found on the potential energy surface (PES). Based on the results found for $C_2H_3S^-$, 12 stable corresponding $C_2H_3S^{\bullet}$ radicals, two of which are reported for the first time, are also found on the MP2(Full)/6–31++G(d) PES. The structures of the stable $C_2H_3S^-$ ions (**1**$^-$ to **12**$^-$) and $C_2H_3S^{\bullet}$ radicals (**1** to **12**) are depicted in Figures 1 and 2, respectively. Figure 3 illustrates the geometries of the $C_2H_3S^-$ TSs. The PES of the $C_2H_3S^-$ anions is presented in Figure 4.

The G2++ energies at 0 K (E_0), enthalpies at 298 K (H_{298}), ΔH_{f0} and ΔH_{f298} values for $C_2H_3S^-$ and $C_2H_3S^{\bullet}$ species are summarized in Tables 1 and 2, respectively. Table 3 lists the corresponding data for the $C_2H_3S^-$ TSs. Also included in Table 2 are the G2++ electron affinities (EAs) of the $C_2H_3S^{\bullet}$ radicals.

In the following discussion, when we quote the EAs of the radicals, the PAs of the anions, and the relative stabilities of the species, we refer to the energy values at 0 K listed in Tables 1, 2 and 3.

4.3.1 Thioformylmethyl Anion (1^-). The most stable $C_2H_3S^-$ anion is the thioformylmethyl anion, CH_2CHS^- (1^-), with *C*s symmetry. Its G2++ ΔH_{f0} and ΔH_{f298} values are –0.3 and –6.0 kJ mol^{-1}, respectively. The G2++ PA of 1^- is 1446.0 kJ mol^{-1}, which is in very good agreement with the experimental result of 1456.0 ± 14 kJ mol^{-1} reported by Zhang and Grabowski.[16] Results of NBO analysis for 1^- indicate that there is hyperconjugation between the lone pair orbital (n_π(S)) and the π^*(C–C) orbital. The C=C double bond length (1.362 Å) in 1^- is longer than that optimized for ethylene, 1.339 Å. The corresponding hyperconjugation is lower in neutral radical, **1**, and its C=C double bond (1.344 Å) is shorter than that in 1^-. This is because the number of electrons in the n_π(S) orbital in $C_2H_3S^-$ is more than that in the neutral radical. The effect of hyperconjugation also strengthens the C–S bond, due to partial π bonding between these two atoms. This is reflected by the C–S bond lengths of 1^- (1.732 Å) and **1** (1.747 Å).

4.3.2 Thioacetyl Anion (2^-). The anion 2^- has C_s symmetry and is the second most stable isomer on the $C_2H_3S^-$ PES. Energetically, it is 157.2 kJ mol^{-1} above 1^-. The energy between 2^- and 1^- is much larger than that between **2** and **1**, 14.1 kJ mol^{-1}. An NBO analysis reveals that **2** has a partial triple bond character between C and S atoms. Addition of one electron to the thiocarbonyl carbon yields 2^-. In forming 2^-, the unpaired electron of **2** localized on the thiocarbonyl carbon is paired up and the partial triple bond between C and S is lost. From **2** to 2^-, the C–C–S angle decreases from 140.4° to 114.4° and the C–S bond lengthens from 1.532 Å to 1.653 Å.

4.3.3 Cyclic $C_2H_3S^-$ Ions (11^-, 12^-). Two cyclic anions, 11^- and 12^-, have been found. The thiirane anion, 11^-, has C_1 symmetry and is 206.1 kJ mol^{-1} higher in energy than 1^-. The calculated PA of 11^- is 1642.2 kJ mol^{-1}, in excellent agreement with the experimental value,[12] 1640.1 ± 21 kJ mol^{-1}. The S–CH bond (1.918 Å) is longer than the S–CH_2 bond (1.832 Å) in 11^-, but the S–CH bond (1.727 Å) is shorter than the S–CH_2 bond (1.848 Å) in **11**. In **11**, NBO results reveal that there are unpaired α electrons on the carbon atom of the CH group and on the sulphur atom. Also, an unpaired β electron is found between the carbon and sulphur atoms, forming a partial double bond. We believe an unpaired β electron is transferred from a lone pair of S atom and an unpaired α electron is left on the S atom. In 11^-, the

additional electron and these three unpaired electrons are all paired up, forming one lone pair each on the carbon atom and the sulphur atom. The partial double bond character is lost and there is considerable repulsion between the anionic lone pair on the CH group and the nonnbonding electrons on the S atom. Thus the S–CH bond becomes longer.

Another cyclic anion, **12**$^-$, with C_s symmetry has its S–H bond trans to both the C–H bonds. This is the least stable isomer on the $C_2H_3S^-$ PES and it is 444.9 kJ mol^{-1} higher in energy than **1**$^-$. A lone pair of electrons is found on each carbon atom in **12**$^-$. For **12**, an unpaired electron is delocalized between these carbon atoms and a partial double bond is formed between them. Thus, the C–C bond length in **12**$^-$ (1.492 Å) is longer than that (1.375 Å) in **12**.

4.3.4 CH_2SCH^- (9$^-$/10$^-$). Two conformers, *trans* (**9**$^-$) and *cis* (**10**$^-$), of CH_2SCH^- have been found. The *trans* conformer has C_1 symmetry and the *cis* conformer has C_s symmetry. Both conformers are about 298.0 kJ mol^{-1} higher in energy than **1**$^-$. Both **9** and **10** are carbenoid radicals with an unpaired electron centered on the CH_2 carbon and an σ lone pair centered on the other carbon. Without hyperconjugation interactions, both the S–CH_2 and S–CH bonds are single C–S single bond. The strong interaction between the π electrons on the S atom with the vacant *p*–type orbital centered on the carbenoide center results in partial double bond character of the S–CH bond. The unpaired electron on the CH_2 group also has interaction with the π nonbonding electrons of the S atom, again resulting in partial double bond character of the S–CH_2 bond. In summary, the three *p* electrons are delocalized over the C–S–C skelton. In forming the corresponding anions, both C–S bonds are double bonds. The additional electron is part of the p electron system. Thus the S–CH_2 bonds in **9** (1.709 Å) and **10** (1.726 Å) are longer than those in **9**$^-$ (1.662 Å) and **10**$^-$ (1.679 Å). The rotational TS **9-10**$^-$ has been identified and the G2++ energy barrier (ΔE_b) for the process **9**$^-$ → **10**$^-$ is 93.6 kJ mol^{-1}.

4.3.5 2–Thiovinyl Anion (5$^-$/6$^-$/7$^-$/8$^-$). As shown in Figure 1, there are four conformers (**5**$^-$, **6**$^-$, **7**$^-$ and **8**$^-$) for the 2–thiovinyl anion. Among them, **6**$^-$ has the lowest energy and **7**$^-$ is the least stable. The energy difference between **6**$^-$ and **7**$^-$ is 12.5 kJ mol^{-1} and **6**$^-$ is 201.9 kJ mol^{-1} higher in energy than **1**$^-$. In each conformer,

the C–C bond is a double bond and a lone pair of electrons is localized on the carbon atom of CH group. Conversions of **5**$^-$ to **7**$^-$ and **6**$^-$ to **8**$^-$ may proceed via TSs **5-7**$^-$ and **6-8**$^-$, respectively. The ΔE_bs for these rearrangements are small, 8.3 and 0.8 kJ mol^{-1}, respectively. Attempts to locate the (in–plane or out–of–plane) TSs for **5**$^-$ → **6**$^-$ and **7**$^-$ → **8**$^-$, which involve the breaking up of a π bond, were not successful.

4.3.6 1–Thiovinyl Anion (3$^-$/4$^-$). *Trans* (**4**$^-$) and *cis* (**3**$^-$) conformers of 1–thiovinyl anion with C_s symmetry have been found. They are the third most stable species on the $C_2H_3S^-$ PES. The *cis* conformer is 8.9 kJ mol^{-1} lower in energy than the *trans* conformer and is 166.9 kJ mol^{-1} higher in energy than **1**$^-$. The ΔE_b for **4**$^-$ → **3**$^-$ is 21.5 kJ mol^{-1}. There is also hyperconjugation between the lone pair orbital (n_π(S)) and the π^*(C–C) orbital. The second–order perturbation stabilization energies obtained by NBO analysis are 84.1 and 107.3 kJ mol^{-1} in **4**$^-$ and **3**$^-$, respectively. This may be the reason why the *cis* conformer is more stable than the *trans* conformer.

4.3.7 Intramolecular Rearrangements of 1$^-$. Four anions (**2**$^-$, **4**$^-$, **5**$^-$, **11**$^-$) can be rearranged from **1**$^-$. Anion **1**$^-$ can be considered as the open form of **11**$^-$. The rearrangement for **1**$^-$ → **11**$^-$ proceeds via TS **1-11**$^-$. The ΔE_b is 250.5 kJ mol^{-1} and the reverse barrier is 44.4 kJ mol^{-1}. These results are similar to those (250.6 and 45.2 kJ mol^{-1}, respectively) calculated at the G2+ level by Merrill et al.[12] Formation of **2**$^-$ from **1**$^-$ can be achieved through 1,2–H shift. The TS **1-2**$^-$ lies 274.2 and 117.0 kJ mol^{-1} above **1**$^-$ and **2**$^-$, respectively. The 1,3–H shift reaction **1**$^-$ → **5**$^-$ and the 2,3–H shift process **1**$^-$ → **4**$^-$ occur through TSs **1-5**$^-$ and **1-4**$^-$, respectively. Their respective ΔE_bs are 246.8 and 273.8 kJ mol^{-1} and the corresponding reverse barriers are 39.4 and 98.0 kJ mol^{-1}.

4.3.8 Intramolecular Rearrangements of Cyclic $C_2H_3S^-$ ions (11$^-$, 12$^-$) and 1–Thiovinyl Anion (3$^-$/4$^-$). Ring opening of **11**$^-$ leads to the formation **1**$^-$ via TS **1-11**$^-$ has been discussed in the preceding paragraph. Another open form of **11**$^-$ is **10**$^-$ which can be formed by breaking the C–C bond of **11**$^-$. The ring opening process **11**$^-$ → **10**$^-$ has a barrier of 181.8 kJ mol^{-1} and the reverse ΔE_b is 89.7 kJ mol^{-1}. The open

form of **12**$^-$ is **7**$^-$. In this reaction, **12**$^-$ → **7**$^-$, one of the C–S bonds breaks via TS **12-7**$^-$. The forward and reverse barriers are 21.9 and 238.2 kJ mol^{-1}, respectively.

Anion **4**$^-$ can rearrange to **8**$^-$ and **1**$^-$ via TSs **8-4**$^-$ and **1-4**$^-$, respectively. The process of **1**$^-$ → **4**$^-$, a 2,3–H shift reaction, has been discussed. The 1,2–H shift reaction **8**$^-$ → **4**$^-$ has a barrier of 189.5 kJ mol^{-1} and the TS **8-4**$^-$ is 216.2 kJ mol^{-1} above **4**$^-$. Interconversion between **2**$^-$ and **3**$^-$ can be achieved through 1,3–H shift. The hydrogen atom which is trans to the sulphur atom in **2**$^-$ shifts to the sulphur atom through TS **2-3**$^-$. This hydride shift reaction of **2**$^-$ → **3**$^-$ has a barrier of 192.9 kJ mol^{-1} and the corresponding reverse barrier is 183.2 kJ mol^{-1}.

4.4 Conclusions

Twelve $C_2H_3S^-$ isomers/conformers have been identified. The thioformylmethyl anion (**1**$^-$) is the most stable isomer and its ΔH_{f0} is –0.3 kJ mol^{-1}. The next two lowest energy species are the thioacetyl anion (**2**$^-$) and 1–thiovinyl anion (**3**$^-$/**4**$^-$). They are 157.2 and 175.8/166.9 kJ mol^{-1} higher in energy than **1**$^-$. A cyclic anion (**12**$^-$) has the highest energy and its ΔH_{f0} is 444.6 kJ mol^{-1}. The G2++ PAs of **1**$^-$ and thiirane anion (**11**$^-$) are 1446.0 and 1642.2 kJ mol^{-1}, respectively, which are in excellent agreement with the experimental data. Other isomers/conformers identified include CH_2SCH^- (**9**$^-$/**10**$^-$), and 2–thiovinyl anion (**5**$^-$/**6**$^-$/**7**$^-$/**8**$^-$).

Four anions (**2**$^-$, **4**$^-$, **5**$^-$, **11**$^-$) can be rearranged from **1**$^-$, with barriers ranging from 246.8 to 274.2 kJ mol^{-1}. Transition structures for ring opening processes of **11**$^-$ → **10**$^-$ and **12**$^-$ → **7**$^-$, and for rearrangements of **8**$^-$ → **4**$^-$ and **2**$^-$ → **3**$^-$ are also found. In addition, rotational TSs **9-10**$^-$, **5-7**$^-$, **6-8**$^-$, and **4-3**$^-$ are located as well. The energetics of these processes are illustrated in Figure 4.

4.5 References

1. Pople, J. A.; Head-Gordon, M.; Fox, D. J.; Raghavachari, K.; Curtiss, L. A. *J. Chem. Phys.* **1989**, *90*, 5622.
2. Curtiss, L. A.; Raghavachari, K.; Trucks, G. W.; Pople, J. A. *J. Chem. Phys.* **1991**, *94*, 7221.
3. Curtiss, L. A.; Raghavachari, K.; Redfern, P. C.; Rassolov, V. R.; Pople, J. A. *J.*

Chem. Phys. **1998**, *109*, 7764.

4. Rozsondai, M. *The Chemistry of Sulphur-Containing functional groups*; Wiley: New York, 1993; pp. 101.
5. Chiu, S.-W.; Lau, K.-C.; Li, W.-K. *J. Phys. Chem. A* **2000**, *104*, 3028.
6. Chiu, S.-W.; Cheung, Y.-S.; Ma, N. L.; Li, W.-K.; Ng, C. Y. *J. Mol. Struct. (THEOCHEM)* **1997**, *397*, 87.
7. Chiu, S.-W.; Cheung, Y.-S.; Ma, N. L.; Li, W.-K.; Ng, C. Y. *J. Mol. Struct. (THEOCHEM)* **1998**, *452*, 97.
8. Chiu, S.-W.; Cheung, Y.-S.; Ma, N. L.; Li, W.-K.; Ng, C. Y. *J. Mol. Struct. (THEOCHEM)* **1999**, *468*, 21.
9. Chiu, S.-W.; Lau, K.-C.; Li, W.-K.; Ma, N. L.; Cheung, Y. -S.; Ng, C. Y. *J. Mol. Struct. (THEOCHEM)* **1999**, *490*, 109.
10. Chiu, S.-W.; Li, W.-K *J. Phys. Chem. A* **2001**, *105*, 7651.
11. Ma, Z. X.; Liao, C.-L.; Yin, H.-M.; Ng, C. Y.; Chiu, S.-W.; Ma, N. L.; Li, W.-K. *Chem. Phys. Lett.* **1993**, *213*, 250.
12. Merrill, G. N.; Zoller, U.; Reed, D. R.; Kass, S. R. *J. Org. Chem.* **1999**, *64*, 7395.
13. Frisch, M. J.; Trucks, G. W.; Schlegel, H. B.; Scuseria, G. E.; Robb, M. A.; Cheeseman, J. R.; Zakrzewski, V. G.; Montgogery, J. A.; Jr.; Stratmann, R.E.; Burant, J. C.; Dapprich, S.; Millam, J. M.; Daniels, A. D.; Kudin, K. N.; Strain, M. C.; Farkas, O.; Tomasi, J.; Barone, V.; Cossi, M.; Cammi, R.; Mennucci, B.; Pomelli, C.; Adamo, C.; Clifford, S.; Ochterski, J.; Petersson, G. A.; Ayala, P. Y.; Cui, Q.; Morokuma, K.; Malick, D. K.; Rabuck, A. D.; Raghavachari, K.; Foresman, J. B.; Cioslowski, J.; Ortiz, J. V.; Baboul, A. G.; Stefanov, B. B.; Liu, G.; Liashenko, A.; Piskorz, P.; Komaromi, I.; Gomperts, R.; Martin, R. L.; Fox, D. J.; Keith, T.; Al-Laham, M. A.; Peng, C. Y.; Nanayakkara, A.; Gonzalez, C.; Challacombe, M.; Gill, P. M. W.; Johnson, B.; Chen, W.; Wong, M. W.; Andres, J. L.; Gonzalez, C.; Head-Gordon, M.; Replogle, E. S.; Pople, J. A. *GAUSSIAN 98*, Revision A.7; Gaussian, Inc., Pittsburgh PA, 1998.
14. Chiu, S.-W.; Lau, K.-C.; Li, W.-K. *J. Phys. Chem. A*. **1999**, *103*, 6003.
15. Reed, A. E.; Curtiss, L. A.; Weinhold, F. *Chem. Rev.* **1988**, *88*, 899.
16. Zhang, L.; Grabowski, J. J. *J. Chem. Soc. Commun.* **1989**, 1819.

Table 1: G2++ Total Energies (E_0), Enthalpies (H_{298}), Standard Heats of Formation at 0 K (ΔH_{f0}) and 298 K (ΔH_{f298}) of $C_2H_3S^-$ Isomer $1^- - 12^-$.

Species	E_0 (hartree)	H_{298} (hartree)	ΔH_{f0} (kJmol^{-1})	ΔH_{f298} (kJ mol^{-1})
1^-	-475.61767	-475.61299	–0.3	–6.0
2^-	-475.55781	-475.55278	156.9	152.1
3^-	-475.55411	-475.54915	166.6	161.6
4^-	-475.55073	-475.54541	175.5	171.4
5^-	-475.53867	-475.53359	207.1	202.5
6^-	-475.54077	-475.53527	201.6	198.1
7^-	-475.53601	-475.53078	214.1	209.9
8^-	-475.54055	-475.53510	202.2	198.5
9^-	-475.50416	-475.49884	297.7	293.7
10^-	-475.50412	-475.49867	297.8	294.2
11^-	-475.53918	-475.53477	205.8	199.4
12^-	-475.44821	-475.44347	444.6	439.1

Table 2: G2++ Total Energies (E_0), Enthalpies (H_{298}), Standard Heats of Formation at 0 K (ΔH_{f0}) and 298 K (ΔH_{f298}), and Electron Affinities (EA) of $C_2H_3S^\bullet$ Isomer 1 – 12.

Species	E_0 (hartree)	H_{298} (hartree)	ΔH_{f0} (kJmol^{-1})	ΔH_{f298} (kJ mol^{-1})	EA (eV)
1	-475.52524	-475.52053	242.4	236.8	2.52
2	-475.51988	-475.51482	256.5	251.8	1.03
3	-475.44886	-475.44427	442.9	437.0	2.86
4	-475.44839	-475.44377	444.2	438.3	2.78
5	-475.48526	-475.48016	347.4	342.8	1.45
6	-475.48570	-475.48057	346.2	341.7	1.50
7	-475.48381	-475.47868	351.2	346.6	1.42
8	-475.48477	-475.47966	348.6	344.1	1.52
9	-475.42284	-475.41781	511.2	506.5	2.21
10	-475.43605	-475.43111	476.6	471.5	1.85
11	-475.50292	-475.49861	301.0	294.3	0.99
12	-475.42815	-475.42360	497.3	491.3	0.55

Table 3: G2++ Total Energies (E_0), Enthalpies (H_{298}), Standard Heats of Formation at 0 K (ΔH_{f0}) and 298 K (ΔH_{f298}) of $C_2H_3S^-$ Transition Structures Identified in This Work.

TS	E_0 (hartree)	H_{298} (hartree)	ΔH_{f0} (kJmol^{-1})	ΔH_{f298} (kJ mol^{-1})
1-2$^-$	-475.51323	-475.50873	273.9	267.8
1-11$^-$	-475.52226	-475.51802	250.2	243.4
1-5$^-$	-475.52366	-475.51917	246.5	240.3
1-4$^-$	-475.51338	-475.50820	273.5	269.1
11-10$^-$	-475.46994	-475.46544	387.6	381.4
8-4$^-$	-475.46837	-475.46295	391.7	387.9
2-3$^-$	-475.48433	-475.47969	349.8	344.0
12-7$^-$	-475.44527	-475.44074	452.4	446.3
9-10$^-$	-475.46851	-475.46374	391.3	385.9
5-7$^-$	-475.53551	-475.53093	215.4	209.5
6-8$^-$	-475.54048	-475.53568	202.4	197.0
4-3$^-$	-475.54254	-475.53786	197.0	191.3

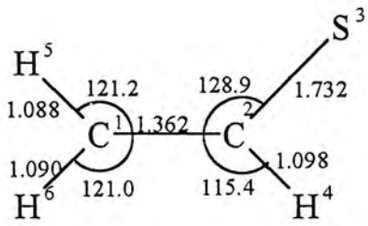

1$^-$ (C_s, ^{1}A')

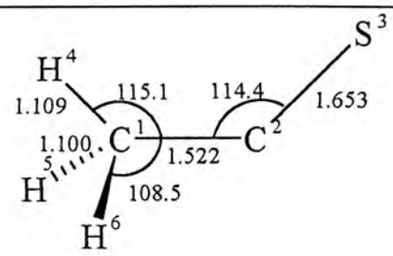

2$^-$ (C_s, ^{1}A')

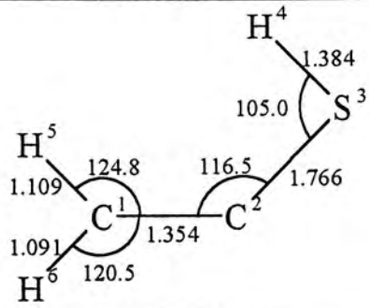

3$^-$ (C_s, ^{1}A')

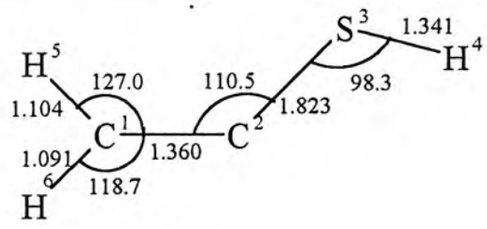

4$^-$ (C_s, ^{1}A')

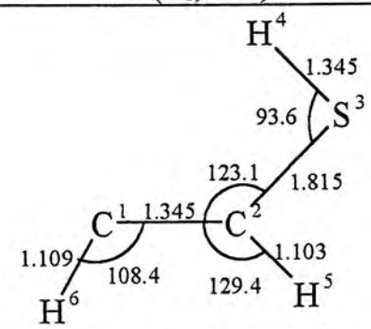

5$^-$ (C_s, ^{1}A')

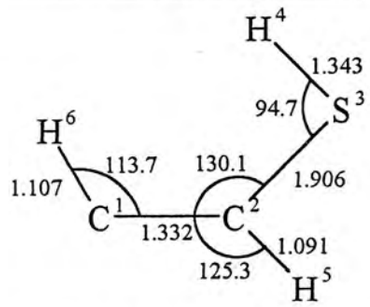

6$^-$ (C_s, ^{1}A')

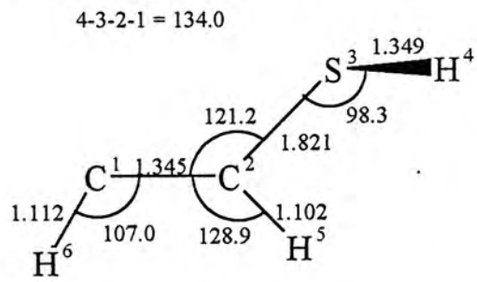

7$^-$ (C_1, ^{1}A)

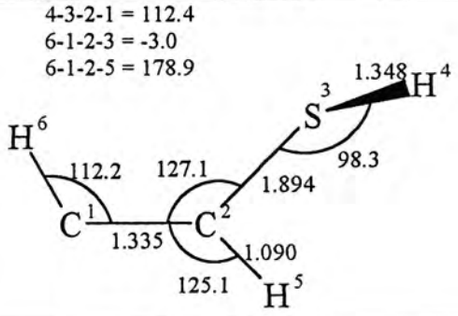

8$^-$ (C_1, ^{1}A)

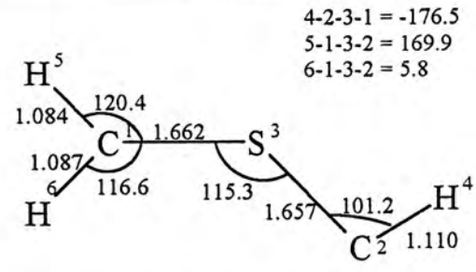

9$^-$ (C_1, ^{1}A)

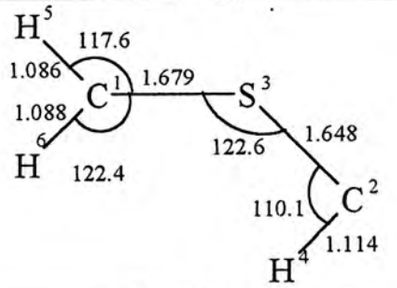

10$^-$ (C_s, ^{1}A')

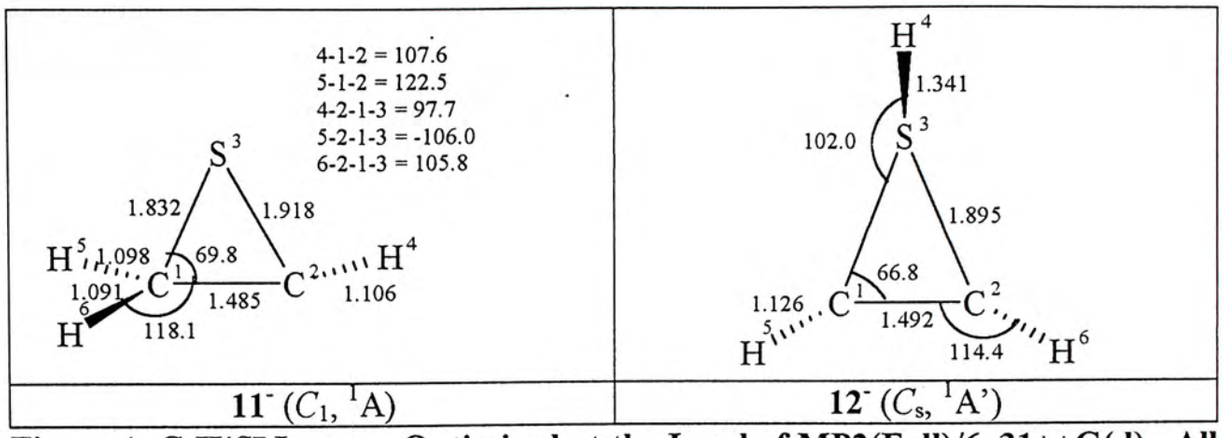

11^- (C_1, ^{1}A)	12^- (C_s, ^{1}A')

Figure 1. $C_2H_3S^-$ Isomers Optimized at the Level of MP2(Full)/6–31++G(d). All Bond Lengths Are in Ångstroms and Angles Are in Degrees.

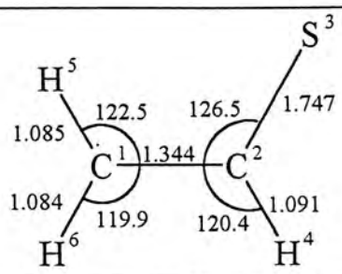

1 (C_s, ^{2}A')

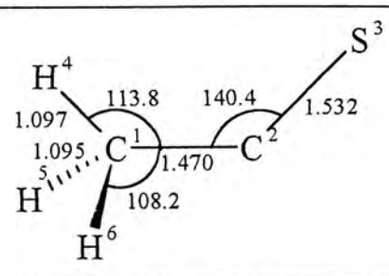

2 (C_s, ^{2}A')

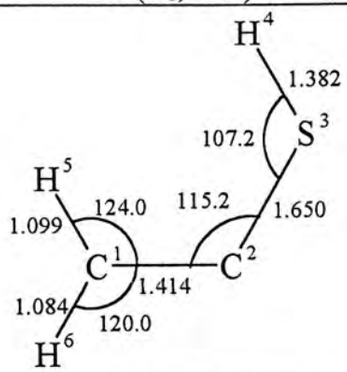

3 (C_s, ^{2}A")

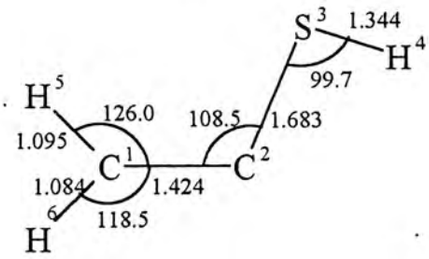

4 (C_s, ^{2}A")

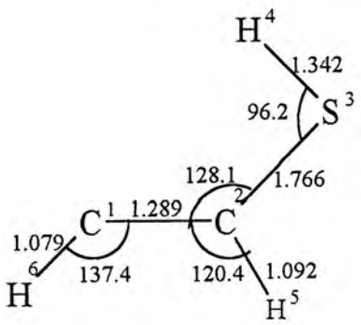

5 (C_s, ^{2}A')

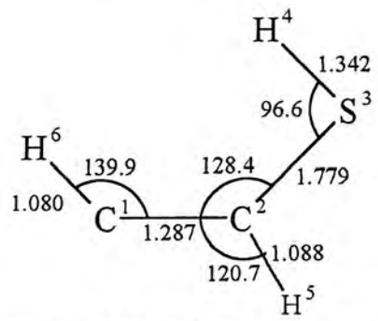

6 (C_s, ^{2}A')

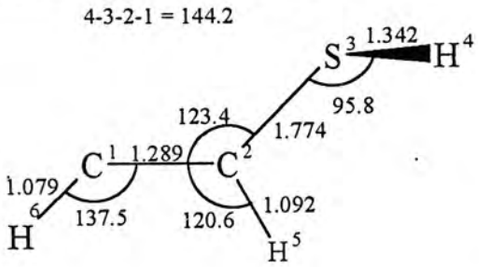

7 (C_1, ^{2}A)

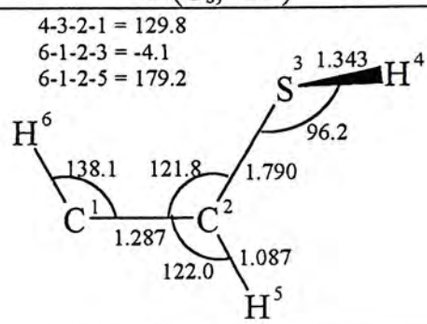

8 (C_1, ^{2}A)

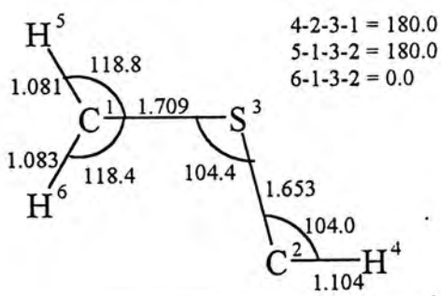

9 (C_1, ^{2}A)

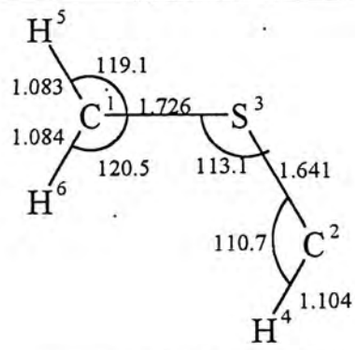

10 (C_s, ^{2}A")

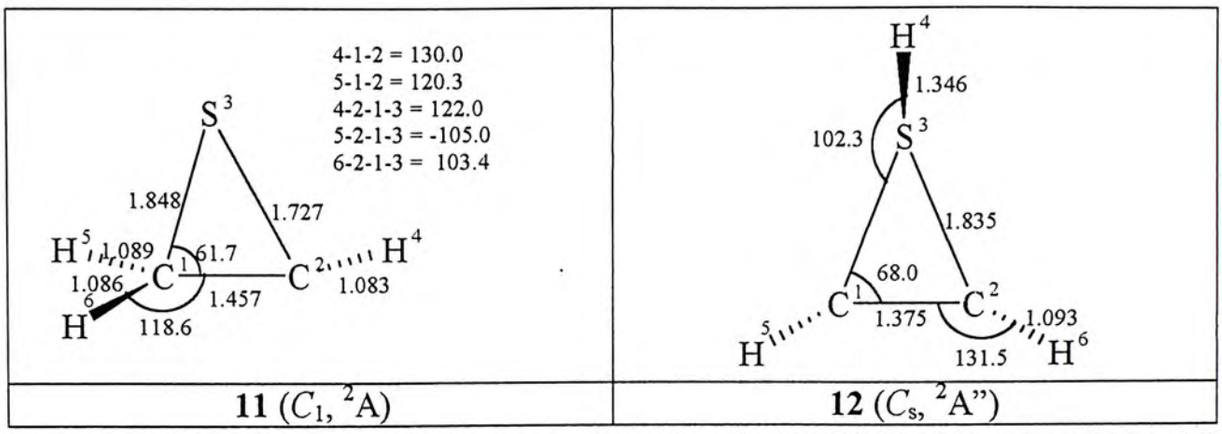

11 (C_1, ^{2}A)	**12** (C_s, ^{2}A")

Figure 2. $C_2H_3S^\bullet$ Isomers Optimized at the Level of MP2(Full)/6–31++G(d). All Bond Lengths Are in Ångstroms and Angles Are in Degrees.

3-2-1 = 120.1 4-1-2 = 122.9 5-1-2 = 119.1 4-1-2-3 = -4.3 5-1-2-3 = 189.8 6-1-2-3 = -113.4 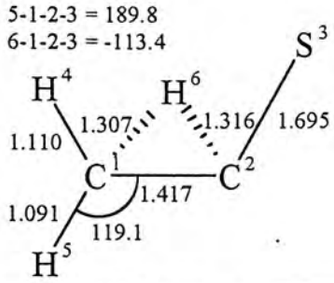	3-2-1-4 = -111.5 5-2-1-4 = 187.4 6-2-1-4 = -3.7 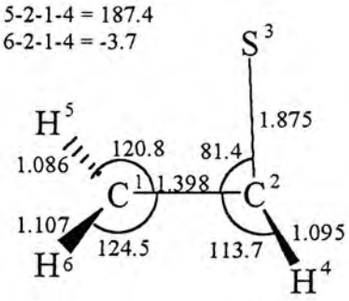
1-2$^-$ (C_1)	**1-11**$^-$ (C_1)
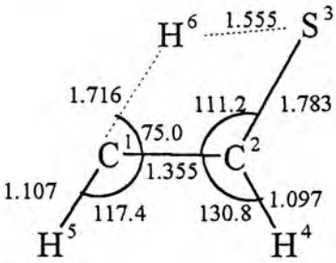	4-1-2-3 = 3.2 5-1-2-3 = 177.9 6-2-3-1 = 164.3 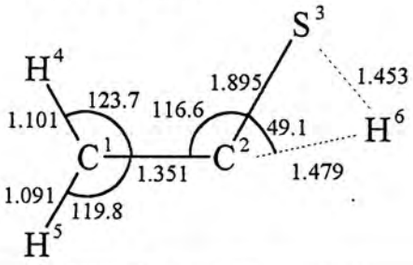
1-5$^-$ (C_s)	**1-4**$^-$ (C_1)
5-1-3 = 121.6 4-2-3-1 = 52.8 5-1-3-2 = -107.5 6-1-3-2 = 47.2 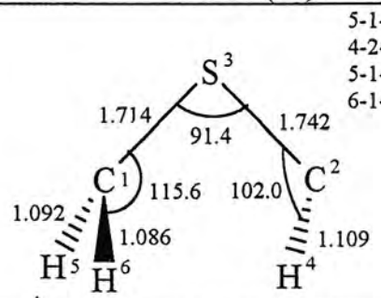	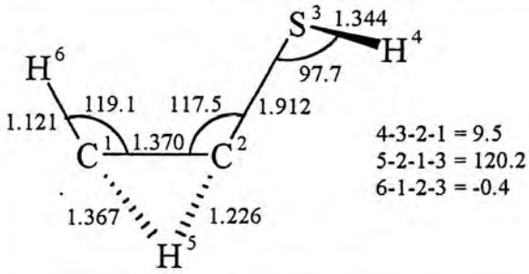
11-10$^-$ (C_1)	**8-4**$^-$ (C_1)
3-2-1 = 112.7 5-2-1 = 125.2 4-3-2-1 = 46.2 5-1-2-3 = 11.9 6-1-2-3 = 170.9 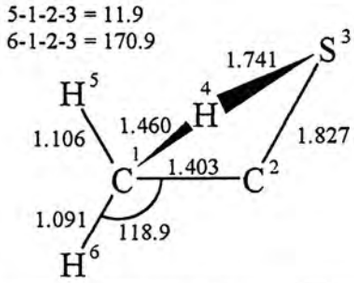	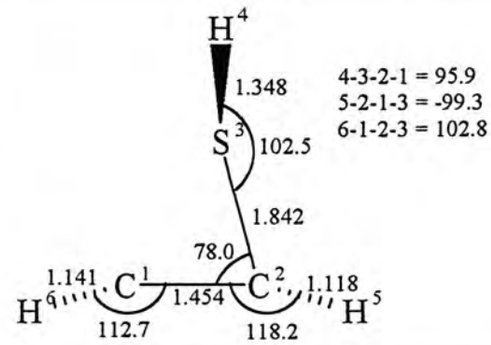
2-3$^-$ (C_1)	**12-7**$^-$ (C_1)

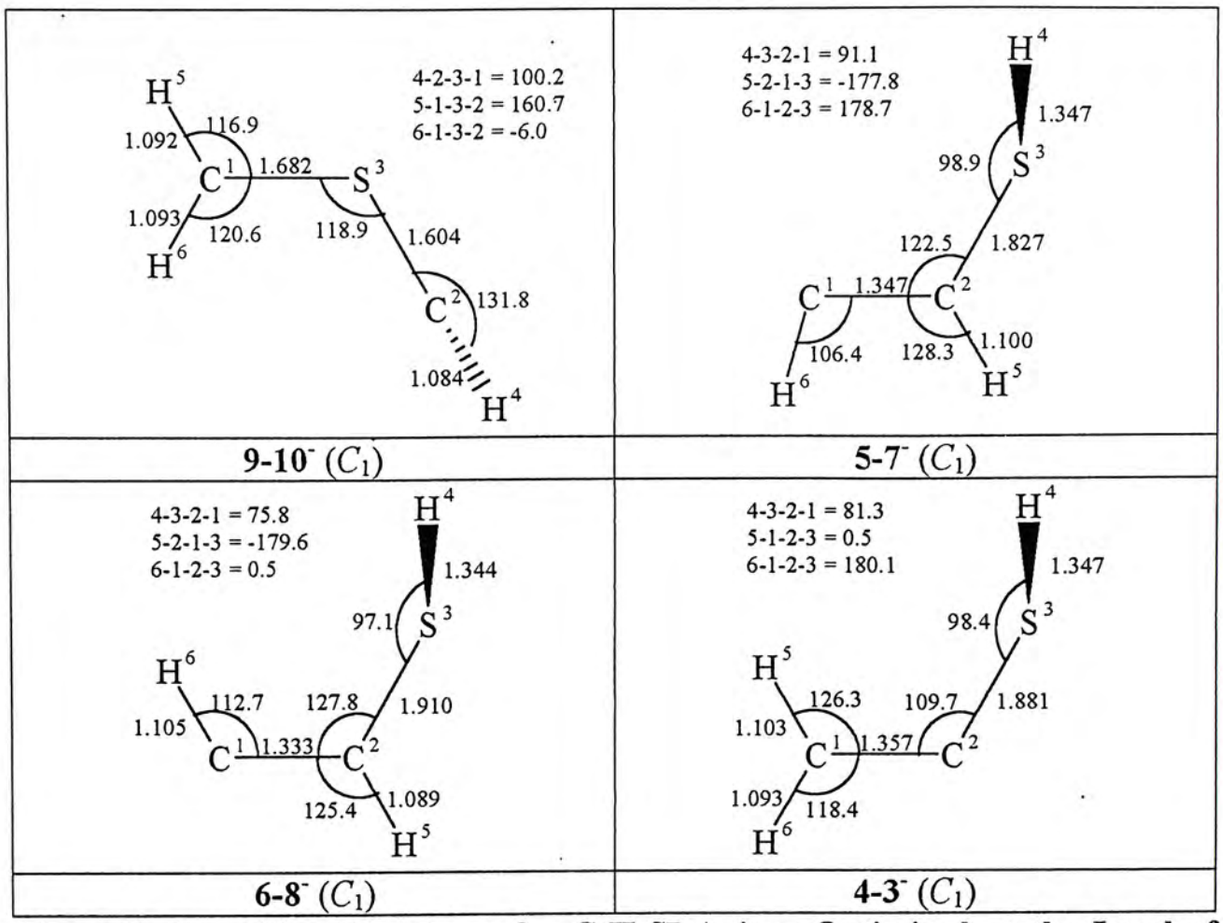

Figure 3. Transition Structures for $C_2H_3S^-$ Anions Optimized at the Level of MP2(Full)/6–31++G(d). All Bond Lengths Are in Ångstroms and Angles Are in Degrees.

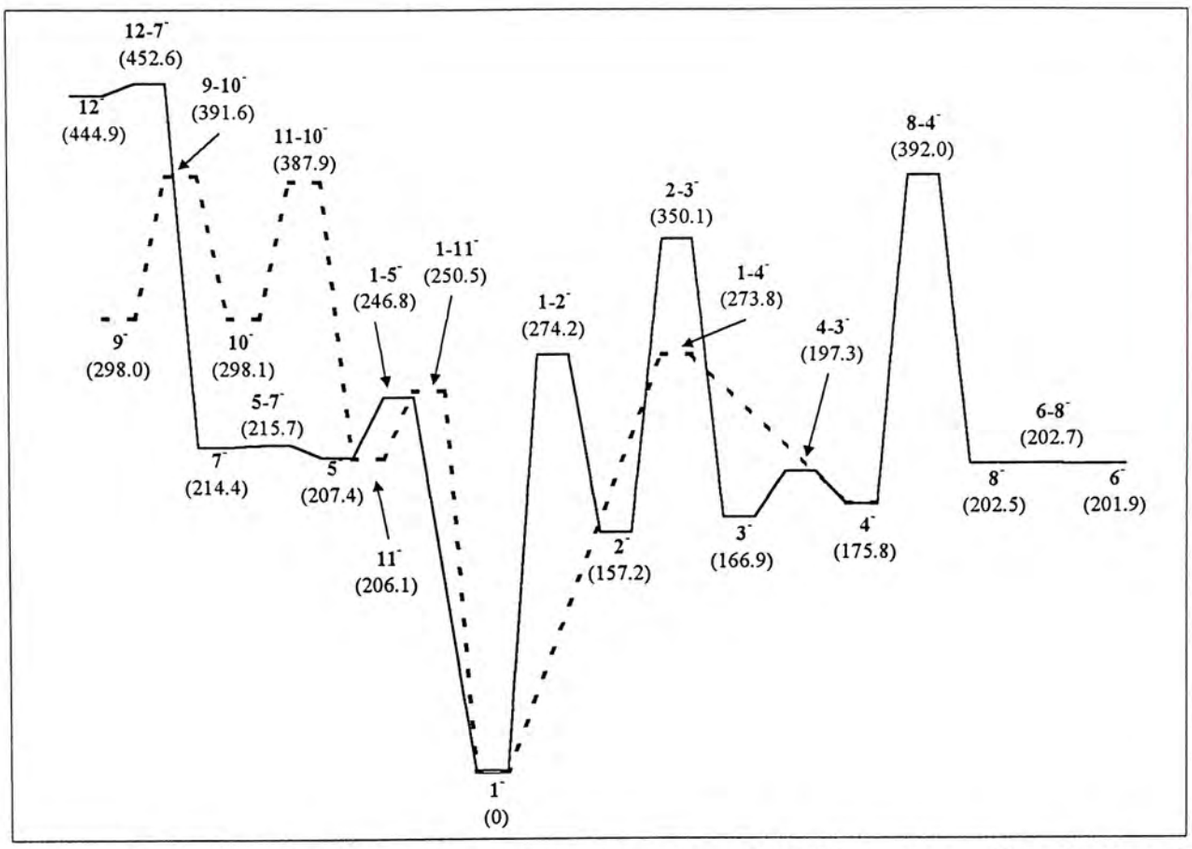

Figure 4. G2++ Potential Energy Surface for $C_2H_3S^-$ Anion. The Values in Bracket are the Relative Energy (in kJ mol^{-1}) with Respect to 1^-.

Chapter 5

Theoretical Studies of Transition Metal Complexes: Bond Energies for Fe^+–D, Fe^+–H_2O, and Fe^+–CO

Abstract

Ab initio calculations have been applied to study the properties of three simple iron(I) complexes, Fe^+–D, Fe^+–H_2O, and Fe^+–CO. It is found that the ground states of Fe^+–H_2O and Fe^+–D are derived from the $^6D(3d^6 4s^1)$ state of Fe^+, while that of Fe^+–CO is derived from the $^4F(3d^7)$ state of Fe^+. In this work, the basis set employed for the metal ion is the [10*s*8*p*3*d*] function, while those for H, D, C, and O are the diffuse valence triple zeta sets of Dunning. Bond energies of these metal complexes have been calculated using different theoretical levels and the results converge at the single–point energy calculated at the CCSD(T) level, based on the geometry optimized at the MP4 level, using the aforementioned basis sets. The calculated bond energy of Fe^+–D is 2.11 eV, in excellent agreement with the experimental result of 2.16 ± 0.06 eV. The Fe–D bond is formed by the spin–pair of the Fe^+ 4*s* and the D 1*s* orbitals. The calculated bond energy of Fe^+–CO, 1.42 eV, is in very good agreement with the experimental result of 1.36 ± 0.08 eV. The NBO result of Fe^+–CO strongly supports that the metal carbonyl bond is based on σ donation from the carbonyl to the metal and π back donation from the metal to the ligand. The computed bond energy of Fe^+–H_2O is 1.17 eV. When this value is compared with the experimental result of 1.32 ± 0.05 eV, the agreement is not very good. The bonding between Fe^+ and the H_2O ligand is electrostatic in character, the main interaction being the electrostatic attraction between the positively charged iron cation and one of the H_2O lone pairs. By comparing the computed bond energies of Fe^+–CO and Fe^+–H_2O, the bond energy of the former is larger by 0.25 eV. However, experimental measurements indicate that this difference is only 0.04 eV. In view of the π back donation capability of the CO ligand, it appears that the calculated results are more in line with our chemical intuition.

5.1 Introduction

Using a variety of mass spectrometric techniques, transition metal ions and their complexes can be generated. In order to understand the bonding in simple transition metal complexes, some properties between transition metal ions and various ligands such as 4*s*-4*p* mixing, 4*s*-3*d* promotion, and 4*s*-3*d* hybridization, etc., should be studied. However, the understanding of these theoretical subjects cannot be realized by experimental data alone. Rather, ab initio calculations should be able to give a meaningful description of the bonding in these complexes. In studies of this type, experiment and calculation should be complementary.

Currently, the theoretical study of transition metal complexes has been an active area of research for several reasons. From one side, there is the challenge of predicting accurately molecular properties such as geometries, binding energies, electronic configurations, etc.; the difficulty is mainly due to the large number of electrons involved and to the complexity of electron correlation effects. From another side, there is the interest in understanding the role of metal–ligand interactions in catalytic processes in which these complexes are often involved. The complexity of these compounds, usually quite large, is one of the reasons why the progress of accurate computations in this particular area is relatively slow. While today for most of the main group element compounds molecular properties can be computed with accuracy routinely, the evaluation of the same data for transition metal compounds usually calls for very sophisticated treatments.[1]

Previously, Armentrout et al. measured the bond energies of Fe^+–D, Fe^+–CO, and Fe^+–H_2O.[2-5] Here we report the results of the ab initio calculations of the bond energies, geometries, electron configurations, charge distributions, and natural bond orbital analysis of these complexes. In addition, these calculated results are compared with the aforementioned experimental data. These three complexes are chosen because experimental estimates of the binding energy are available, and moreover, several theoretical works have been done.[6-10] However, these three complexes were studied by different computational methods. In this work, we study Fe^+–D, Fe^+–CO, and Fe^+–H_2O using same computational method and this is the first step to study how ligation affects the electronic structure and reactivity at the transition metal center.

The bonding in transition metal carbonyls is usually described according to the classical model of Dewar, Duncanson, and Chatt,[11,12] in terms of σ donation from the CO orbital (a carbon *sp* lone pair) to the metal and the accompanying π back donation from the metal to the carbonyl 2π (or π^*) orbital. This is different from a typical bond in organic molecules and great care is needed to obtain an accurate description. The bonding properties of transition metal hydride and transition metal hydrates are different, with spin–pairing and electrostatic interactions being dominant in these bonds, respectively.

5.2 Computational Method

The metal basis sets employed are the [10*s*8*p*3*d*] contraction of the (14*s*11*p*6*d*) functions, while those for the remaining atoms are the diffuse valence triple zeta sets, all taken from Dunning's compilation.[13,14] Five levels of treatment are used in our study. The first one is the SCF method. The states of iron complexes are then tested using the single–excitation CI method. The orbitals selected for occupation may not be those with the lowest energy. Alterations of orbitals are usually required in order to arrive at the ground state configuration. The iron complexes with altered orbitals are then studied at the MP2 and MP4 levels. Finally, single–point calculations at the QCISD(T) and CCSD(T) levels with the structures optimized at the MP4 level were computed. The MP2 harmonic frequencies are used for zero–point vibrational energy correction. The resulting bond energies converge at the single–point energy calculated at the CCSD(T) level. Zero–point energy (ZPE) and basis set superposition error (BSSE) corrections are also included in the 'final' bond energies; BSSE was evaluated using the counterpoise method of Boys and Bernardi.[15]

Metal ligand features are analyzed in terms of the natural bond orbital (NBO)[16] scheme at the MP4 level. This analysis allows us to isolate the metal–ligand interaction energies in low–order perturbative expressions of easily interpretable form and to relate these expressions to chemical explanations. This scheme has been successfully applied to the analyse of metal–ligand interaction.[16]

All computations involved in this work were carried out on DEC 900 au workstations using the Gaussian 98 suite of programs.[17]

5.3 Results and Discussion

The geometries of the three complexes and the H_2O and CO ligands are listed in Table 1. The results of the bond energies of all the complexes at different level of theory are given in Table 2.

5.3.1 Fe^+–D. The ground state of Fe^+ is $^6D(3d^6 4s^1)$, but this state is only 0.23 eV lower in energy than the excited states $^4F(3d^7)$.[18] For Fe^+–D, we find the ground state to be $^5\Delta$, derived from the ^6D state of Fe^+. The calculated bond energy is 2.11 eV, in excellent agreement with the experimental result of 2.16 ± 0.06 eV.[2,3] The Fe^+ occupation is $3d(xy)^1 3d(xz)^1 3d(yz)^1 3d(x^2\text{-}y^2)^2 3d(z^2)^1 4s^1$. The sixth non-bonded d electron goes into a δ orbital [from $d(x^2\text{-}y^2)$] to minimize electron repulsion with the electrons in the σ bond. The Fe–D bond is formed by the spin–pair of the Fe^+ $4s$ and the D $1s$ orbitals. The calculated orbital occupancy for the Fe^+ and D in the complex are $4s^{0.45}3d^{6.06}4p^{0.01}$ and $1s^{1.45}2p^{0.03}$, respectively. The natural population analyses (NPA) atomic charges on the Fe^+ and D, q_{Fe} and q_D, are +1.477 and -0.477 respectively. The NPA atomic charges and the orbitals occupancy from the MP4 density for all three complexes are summarized in Table 3 for easy comparison.

5.3.2 Fe^+–CO. The calculated bond energy of Fe^+–CO, 1.42 eV, is again in very good agreement with the experimental result of 1.36 ± 0.08 eV.[4] On the other hand, the ground state of Fe^+–CO is $^4\Sigma^-$. The Fe^+ occupation, derived from the ^4F state of Fe^+, is $3d(xy)^1 3d(xz)^2 3d(yz)^2 3d(x^2\text{-}y^2)^1 3d(z^2)^1$. From the NPA results, atomic charges on Fe, C, and O, q_{Fe}, q_C, and q_O, are +1.043, +0.396, and -0.439 respectively. This result shows that there is about 0.043 e^- transferred from Fe^+ to CO. The orbital occupancy for Fe^+ is $4s^{0.11}3d^{6.84}4p^{0.01}$, suggesting that the bonding between Fe^+ and CO involves $4s3d_\sigma$ hybridization.

The traditional picture of Dewar, Duncanson, and Chatt [11,12] is based on σ donation from the carbonyl to the metal and π back donation from the metal to the ligand. For the CO ligand, the σ donation arises from the 5σ hybrid orbital (essentially an sp hybrid orbital of the carbon atom, contributing to the σ^* orbital) to the unoccupied metal orbitals with σ symmetry, and the π back donation is from the metal to the empty antibonding orbital ($2\pi^*$) of CO. The NBO method strongly supports this traditional picture, showing clearly that the metal carbonyl is

dominated by these two contributions. The result of NBO analysis of the Fe^+–CO bonding is summarized in Table 4.

If the second–order perturbation stabilization energy for a donor bond orbital transferred to an acceptor bond orbital is large, it indicates that there is strong interaction between the orbitals. Results in Table 4 indicate that the σ interaction is stronger than that of the π back donation. For the α electron, there is the donation from the *sp* hybrid orbital of carbon to the unoccupied 4*s* orbital of iron. However, the β electron donates from the *sp* hybrid orbital of carbon to the *sd* hybrid orbital of iron. The stabilization energy for the α electron is larger than that for the β electron. The π back donation occurs from the π orbitals [*d*(xz) and *d*(yz)] of the iron to the empty antibonding orbitals ($2\pi^*$) of CO. By symmetry, the stabilization energies for the donation from either *d*(xz) or *d*(yz) to the π^* of CO are the same.

5.3.3 Fe^+–H_2O. The ground state of Fe^+–H_2O is $^6A_1$, derived from the ^6D ground state of Fe^+, with an occupation of $3d(xy)^1 3d(xz)^1 3d(yz)^1 3d(x^2\text{-}y^2)^2 3d(z^2)^1 4s^1$. The computed bond energy is 1.17 eV. When this value is compared with the experimental result of 1.32 ± 0.05 eV,[5] the agreement is not very good, even though it may still be deemed as acceptable. From the results of NPA, atomic charges on Fe, O, and H, q_{Fe}, q_O, and q_H, are +0.988, -1.065, and +0.539 respectively. The values of q_O and q_H for unbound H_2O are -0.928 and +0.464, respectively. Comparison of the q_O and q_H with those of unbound water shows that hydrate formation is accompanied by an *increase* in the electronic charge on oxygen and a *decrease* in the electronic charge on the hydrogens. There is thus charge transfer from the water to the iron(I) cation. In this case, there is 0.012 e^- transferred from the ligand to the Fe^+. The orbital occupancy for the Fe^+ in Fe^+–H_2O is $4s^{0.96}3d^{6.01}4p^{0.04}$. The bonding between Fe^+ and the H_2O ligand is essentially electrostatic in nature, the main interaction is between the iron cation and one of the H_2O lone pairs. In Fe^+–H_2O, it is possible for the 4*s* orbital of iron to mix in 4*p* character in order to reduce the repulsion between the occupied 4*s* orbital and the electron donating water ligand. The doubly occupied 3*d* orbital is the $3d(x^2\text{-}y^2)$, where the symmetry axis is z and the molecule lies on the yz plane, see Figure 1. The 3*dδ* orbitals, $d(x^2\text{-}y^2)$ and *d*(xy), have the smallest overlap with the H_2O orbitals.

It should be noted that, in their study of Fe^+–H_2O, Bock et al.[10] found that, at the MP2(Full)/6-311++G(d,p)//MP2(Full)/6-311++G(d,p) level, the lowest electronic state is $^4B_2$, with all the electrons occupying the $3d$ orbitals. On the other hand, at the CCSD(T)(Full)/6-311++G(d,p)//MP2(Full)/6-311++G(d,p) level, $^6A_1$ was found to be the ground state, in agreement with our results.

Recall that in Fe^+–D and Fe^+–H_2O, Fe^+ binds with the ligands through the ^6D state of the $3d^6 4s^1$ configuration. However, in Fe^+–CO, Fe^+ combines with CO through the ^4F state arising from the $3d^7$ configuration. Here the CO ligand can take advantage of π back donation and this effect favors the $3d^7$ configuration, with all seven electrons occupying the d orbitals. The H_2O ligand has a smaller repulsion with the Fe^+, compared with CO, so binding through $3d^6 4s^1$ is energetically more favorable.[7]

By comparing the computed bond energies of Fe^+–CO and Fe^+–H_2O, it is found that the former is larger by 0.25 eV. However, experimental measurements indicate that this difference is only 0.04 eV. In view of the π back donation capability of the CO ligand, it appears that the calculated results are more in line with our chemical intuition.

5.4 Conclusions

High–level ab initio calculations have been applied to study the properties of three iron(I) complexes, Fe^+–D, Fe^+–H_2O, and Fe^+–CO. The ground states Fe^+–D, Fe^+–CO and, Fe^+–H_2O are $^5\Delta$, $^4\Sigma^-$, and $^6A_1$, respectively. The calculated bond energy of Fe^+–D is 2.11 eV, in excellent agreement with the experimental result of 2.16 ± 0.06 eV. The Fe–D bond is formed by the spin–pair of the Fe^+ $4s$ and the D $1s$ orbitals. The calculated bond energy of Fe^+–CO, 1.42 eV, is also in very good agreement with the experimental result of 1.36 ± 0.08 eV. The NBO result of Fe^+–CO strongly supports that metal carbonyl bond is based on σ donation from the carbonyl to the metal and π back donation from the metal to the ligand. The computed bond energy of Fe^+–H_2O is 1.17 eV, only in fair agreement with the experimental result of 1.32 ± 0.05 eV. The bonding between Fe^+ and the H_2O ligand is electrostatic in character, the main interaction being the attraction between the iron cation and one of the H_2O lone pairs. By comparing the computed bond energies of

Fe^+–CO and Fe^+–H_2O, the former is found to be larger by 0.25 eV. However, experimental measurements indicate that this difference is only 0.04 eV. In view of the π back donation capability of the CO ligand, it appears that the calculated results are more in line with our chemical intuition.

5.5 References

1. Salahub, D. R.; Russo, N. *Metal-Ligand Interactions: From Atoms, to Clusters, to Surfaces, Vol. 378 of NATO Advanced Study Institute, Series C*; Kluwer Academic: Dordrecht, 1992.
2. Elkind, J. L.; Armentrout, P. B. *J. Am. Chem. Soc.* **1986**, *108*, 2765.
3. Elkind, J. L.; Armentrout, P. B. *J. Phys. Chem.* **1986**, *90*, 5736.
4. Schultz, R. H.; Crellin, K. C.; Armentrout, P. B. *J. Am. Chem. Soc.* **1991**, *113*, 8590.
5. Schultz, R. H.; Armentrout, P. B. *J. Phys. Chem.* **1993**, *97*, 596.
6. Schilling, J. B.; Goddard III, W. A.; Beauchamp, J. L. *J. Am. Chem. Soc.* **1986**, *108*, 582.
7. Barnes, L. A.; Rosi, M; Bauschlicher, Jr. C. W. *J. Chem. Phys.* **1990**, *93*, 609.
8. Rosi, M; Bauschlicher, Jr. C. W. *J. Chem. Phys.* **1989**, *90*, 7264.
9. Rosi, M; Bauschlicher, Jr. C. W. *J. Chem. Phys.* **1990**, *92*, 1876.
10. Trachtman, M.; Markham, G. D.; Glusker, J. P.; George, P.; Bock, C. W. *Inorg. Chem.* **1998**, *37*, 4421.
11. Dewar, M. J. S. *Bull. Soc. Chim. Fr.* **1951**, *18*, C71.
12. Chatt, J.; Duncanson, L. A. J. Chem. Soc. **1953**, 2939.
13. Dunning, Jr. T. H. *J. Chem. Phys.* **1989**, *90*, 1007.
14. Kendall, R. A.; Dunning, Jr. T. H.; Harrison, R. J.; *J. Chem. Phys.* **1992**, *96*, 6796.
15. Boys, S. F.; Bernardi, F. *Mol. Phys.* **1970**, *19*, 553.
16. Reed, A. E.; Curtiss, L. A.; Weinhold, F. *Chem. Rev.* **1988**, *88*, 899.
17. Frisch, M. J.; Trucks, G. W.; Schlegel, H. B.; Scuseria, G. E.; Robb, M. A.; Cheeseman, J. R.; Zakrzewski, V. G.; Montgogery, J. A.; Jr.; Stratmann, R.E.; Burant, J. C.; Dapprich, S.; Millam, J. M.; Daniels, A. D.; Kudin, K. N.; Strain, M. C.; Farkas, O.; Tomasi, J.; Barone, V.; Cossi, M.; Cammi, R.; Mennucci, B.; Pomelli, C.; Adamo, C.; Clifford, S.; Ochterski, J.; Petersson, G. A.; Ayala, P.

Y.; Cui, Q.; Morokuma, K.; Malick, D. K.; Rabuck, A. D.; Raghavachari, K.; Foresman, J. B.; Cioslowski, J.; Ortiz, J. V.; Baboul, A. G.; Stefanov, B. B.; Liu, G.; Liashenko, A.; Piskorz, P.; Komaromi, I.; Gomperts, R.; Martin, R. L.; Fox, D. J.; Keith, T.; Al-Laham, M. A.; Peng, C. Y.; Nanayakkara, A.; Gonzalez, C.; Challacombe, M.; Gill, P. M. W.; Johnson, B.; Chen, W.; Wong, M. W.; Andres, J. L.; Gonzalez, C.; Head-Gordon, M.; Replogle, E. S.; Pople, J. A. *GAUSSIAN 98*, Revision A.7; Gaussian, Inc., Pittsburgh PA, 1998

18. Sugar, J.; Corliss, C. *J. Chem. Phys. Ref. Data* **1985**, *14*, 1.

Table 1: Bond Lengths (Å) and Bond Angles (deg) for the Iron(I) Complexes and the Unbound Ligands Optimized at the MP4 Level.

Species	Fe–D		
Fe^+–D	1.592		
Species	Fe–C	C–O	
Fe^+–CO	1.836	1.150	
CO		1.147	
Species	Fe–O	O–H	HOH
Fe^+–H_2O	2.101	0.969	106.5
H_2O		0.963	104.1

Table 2: Bond Energies of Fe^+–D, Fe^+–CO, and Fe^+–H_2O at Different Level of Theory.

Species	Level of Theory	Total Energies (hartree)	Separated Energies (hartree)	D_0[a] (eV)	D_0'[b] (eV)
Fe^+–D	HF	-1262.71663	-1262.67996	1.00	0.82
	MP2	-1262.80650	-1262.73613	1.91	1.73
	MP4	-1262.82049	-1262.74167	2.14	1.96
	QCISD(T)	-1262.82646	-1262.74228	2.29	2.11
	CCSD(T)	-1262.82627	-1262.74210	2.29	2.11
			Experimental Result	2.16 ± 0.06 eV[c]	
Fe^+–CO	HF	-1374.91700	-1374.88842	0.78	0.57
	MP2	-1375.41559	-1375.35267	1.71	1.51
	MP4	-1375.45514	-1375.38346	1.95	1.74
	QCISD(T)	-1375.44387	-1375.38227	1.68	1.47
	CCSD(T)	-1375.44068	-1375.38094	1.63	1.42
			Experimental Result	1.36 ± 0.08 eV[d]	
Fe^+–H_2O	HF	-1338.28879	-1338.24621	1.16	0.96
	MP2	-1338.61677	-1338.56989	1.28	1.13
	MP4	-1338.63800	-1338.59008	1.30	1.15
	QCISD(T)	-1338.63832	-1338.58958	1.33	1.17
	CCSD(T)	-1338.63785	-1338.58916	1.32	1.17
			Experimental Result	1.32 ± 0.05 eV[e]	

[a] Bond energies without ZPE or BSSE correction. [b] Bond energies corrected with ZPE and BSSE. [c] Experimental result from ref 2 and 3. [d] Experimental result from ref 4. [e] Experimental result from ref 5.

Table 3: Atomic Charges, q, and Orbital Occupancy in the Fe^+–D, Fe^+–CO, and Fe^+–H_2O, Calculated from Natural Population Analyses (NPA) Using the MP4 Results.

Species	Atom	NPA Atomic Charge, q	Orbital Occupancy
Fe^+–D	Fe^+	+1.477	$4s^{0.45}3d^{6.06}4p^{0.01}$
	D	-0.477	$1s^{1.45}2p^{0.03}$
Fe^+–CO	Fe^+	+1.043	$4s^{0.11}3d^{6.84}4p^{0.01}$
	C	+0.396	$2s^{1.46}2p^{2.08}3s^{0.03}3p^{0.02}3d^{0.01}$
	O	-0.439	$2s^{1.71}2p^{4.67}3s^{0.04}$
CO	C	+0.609	$2s^{1.62}2p^{1.72}3s^{0.03}4p^{0.01}5d^{0.01}$
	O	-0.609	$2s^{1.73}2p^{4.83}4d^{0.04}$
Fe^+–H_2O	Fe^+	+0.988	$4s^{0.96}3d^{6.01}4p^{0.04}$
	O	-1.065	$2s^{1.75}2p^{5.29}3s^{0.01}3p^{0.01}3d^{0.01}$
	H	+0.539	$1s^{0.46}$
	H	+0.539	$1s^{0.46}$
H_2O	O	-0.928	$2s^{1.75}2p^{5.16}3d^{0.02}$
	H	+0.464	$1s^{0.53}$
	H	+0.464	$1s^{0.53}$

Table 4: Summary of the NBO Analysis of Fe^+–CO.

Spin	Donor NBO [hybrids]	Acceptor NBO [hybrids]	ΔE^f (kcal mol^{-1})
α	C [s(67.93%) p(32.01%)]	Fe [s(96.70%)]	31.9
β	C [s(66.77%) p(33.17%)]	Fe [s(43.01%)d(56.90%)]	48.7
	Fe [d(99.94%]	C-O [p(99.46%)]	18.3
	Fe [d(99.94%]	C-O [p(99.46%)]	18.3

[f] The second-order perturbation stabilization energies

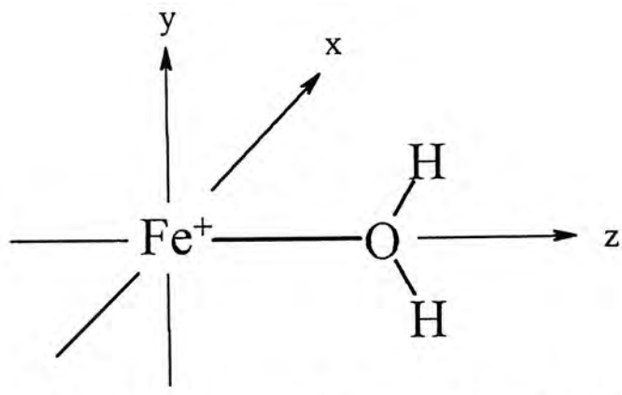

Figure 1. Coordinate System of Fe^+–H_2O.

Chapter 6

Ab Initio Study of the Charge–Delocalized and –Localized Form of the Rhodizonate Dianion

Abstract

Ab initio calculations have been applied to identify computationally the experimentally found charge–localized C_{2v} structure of the rhodizonate dianion ($C_6O_6^{2-}$), and to find a theoretical level that would yield six C–C bonds in the 1.440 Å range for the charge–delocalized D_{6h} form of $C_6O_6^{2-}$. In the presence of the two Na^+ cations or one Ca^{2+} cation, structures with C_2 symmetry instead of those with C_{2v} symmetry of the charge–localized form have been found with one C–C and four C–O double bonds, but most of the computed bond lengths are not in very good agreement with the experimental measurements. For the case of the charge–delocalized form, we cannot find a theoretical level that would yield the computed C–C bonds within the experimental range and would have π electron cloud covering the whole ring.

6.1 Introduction

In the early 1960s, West et al. suggested that monocyclic oxocarbon dianions of general formula $C_nO_n^{2-}$ should constitute a new series of "aromatic" compounds.[1] Here, the "oxocarbon" designates compounds in which all, or nearly all, of the carbon atoms are attached to carbonyl or enolic oxygens or to their hydrated equivalents.[2,3] The most famous monocyclic oxocarban are the deltate ($C_3O_3^{2-}$), squarate ($C_4O_4^{2-}$), croconate ($C_5O_5^{2-}$), and rhodizonate ($C_6O_6^{2-}$) dianions. The IR and Raman spectra, along with the deduced force constants, indicated $C_4O_4^{2-}$ and $C_5O_5^{2-}$ to have D_{nh} symmetry,[4] and this was confirmed later by X–ray analysis.[5,6] The Urey–Bradly force fields of $C_nO_n^{2-}$ (n = 3,[7] 4, and 5 [4]) were compared with those of aromatic species such as benzene, the cyclopentadienyl anion, and the cyclopropenyl cation. The C–C stretching force constants for $C_4O_4^{2-}$ and $C_5O_5^{2-}$ are greater than those for a C–C single bond and those for the $C_3O_3^{2-}$ dianion are as large as those of benzene. This indicates extensive electron delocalization over the oxacarbon rings. Large delocalization energies were consistent with this observation.[8]

However, Dewar et al.[9,10] and Hess and Schaad[11] pointed out that delocalization energy cannot be used as a measure of aromatic stabilization. Almost all conjugated systems, even very labile ones, are known to have significant delocalization energies. Delocalization energies of familiar carbocyclic systems can seldom be arranged in the experimental order of stability.[12] The present consensus is that any aromaticity index of a cyclic conjugated system must be related to some thermodynamic stability estimated relative to an appropriate olefinic reference structure. Using graph theory, Aihara[13] calculated the topological resonance energy (TRE) and diamagnetic susceptibilities of $C_nO_n^{2-}$ and also found that the degree of aromaticity decreases with increasing ring size. This conclusion was supported further by Ha et al.'s semiempirical and ab initio results on the IR frequencies and diamagnetic anisotropies of $C_nO_n^{2-}$.[14] Jug also reached similar conclusions using bond orders as an alternative critieron.[15] In recent year, Schleyer et al. carried out ab initio calculation on $C_nO_n^{2-}$ (n = 3–6) and also concluded that the aromaticity decrease with increasing ring size.[16] They found that $C_3O_3^{2-}$, $C_4O_4^{2-}$, and $C_5O_5^{2-}$ have symmetries of D_{3h}, D_{4h}, and D_{5h}, respectively while $C_6O_6^{2-}$ has C_2 symmetry. Note that $C_nO_n^{2-}$ have only 2π electrons assigned to the carbon rings, and one would expect decreasing aromaticity with the ring size on this basis.

Recently, Mak and Lam have reported that $C_6O_6^{2-}$ anions with C_{2v} and D_{6h} symmetries were generated and stabilized in a hydrogen–bonded host lattice. In addition, these anions' structures were determined by X–ray crystallography .[17] The D_{6h} tautomer has a charge–delocalized form and the measured C–C and C–O bond lengths are 1.440–1.442 Å and 1.245–1.246 Å, respectively. The C_{2v} tautomer is a charge–localized form with five long (1.439 –1.472 Å) and one short (1.404 Å) C–C bonds and four short (1.231–1.246 Å) and two long C–O (1.265 Å) bonds. The D_{6h} and C_{2v} structures are corresponding to non–benzenoid aromatic and enediolate character, respectively. The measured structures of these tautomers are shown in Figure 1. The latest calculations by Schleyer et al. are not in agreement with the experimental results where the calculated C–C bonds are about 1.500 Å.[16] In addition, there has been no theoretical report on the C_{2v} tautomer.

In this chapter, our objectives are to identify computationally the experimentally found C_{2v} structure, and, for the D_{6h} structure, we will attempt to find a theoretical level that would yield six C–C bonds in the 1.440 Å range.

6.2 Computational Methods

The charge–delocalized structure has been studied at different levels including HF, MP2, B3LYP, B3PW91, QCISD and CASSCF in order to yield the C–C bond lengths that close to the experimental measurement. Some calculations were carried out with very large basis sets such as 6–31+G(2df,p) and aug–cc–pvtz as implemented in the Gaussian 98 program.[18]

The geometry optimizations and frequency calculations of the charge–localized form were carried out in the presence of counter ions, either two Na^+ cations or one Ca^{2+} cation. The theoretical levels employed included HF/6–31(d), MP2(full)/6–31G(d), B3LYP/6–31G(d), and B3LYP/6–311+G(d).

6.3 Results and Discussion

6.3.1 Charge–Localized $C_6O_6^{2-}$. Without the addition of the counter ion, we failed to locate the enol tautomer, no matter how hard we tried. Even under the C_{2v} symmetry constraint, all six C–C bonds came out essentially with an equal length; ditto for the six C–O lengths. However, in the presence of either two Na^+ cations or one Ca^{2+}cation, the enol tautomer with C_{2v} and C_2 symmetries have been located and their structures are shown in Figures 2 and 3.

As shown in Figures 2 and 3, the enol complexes minimum have C_2 symmetry, while those structures with C_{2v} symmetry are transition states or higher order saddle points. The best results come from Ca complex by placing the Ca^{2+} symmetrically between two "neighboring" oxygen atoms. Here we do get five long and one short C–C bonds and four short and two long C–O bonds, in qualitative agreement with experimental structure. From the result obtained at the B3LYP/6–311+G(d) level, the shortest and the longest C–C bonds are 1.405 and 1.542 Å, respectively, and the C–O bonds range from 1.204 to 1.320 Å. For the MP2 level, the C–C and the C–O bonds are 1.420–1.522 and 1.227–1.327 Å, respectively. Compared with the experimental measurements, most of the computed C–C bonds are clearly to be "too long". Also, the complexes are not exactly planar, even though they are "nearly" so. Even though our calculated results are not in perfect agreement with experimental data, this is the first time that a charge–localized enediolate tautomer for the rhodizonate dianion has been computationally identified.

The result of the natural bond orbital[19] (NBO) analysis of the MP2 density reveals that C1–C2, C3–C9, C4–C10, C5–C11, and C6–C12 bonds have double bond character, while all others are single bonds. Table 1 summarizes the results of the second–order perturbation theory analysis of the Fock matrix in NBO basis. The interaction energy arising from the electron donation to the σ^* orbital of the C5–C6 bond is larger than those for the C3–C5 and the C1–C3 bonds. This may be one of the reasons why the C5–C6 bond is the longest.

6.3.2 Charge–Delocalized $C_6O_6^{2-}$. The computed C–C and C–O bond lengths of the D_{6h} structure are summarized in the Table 2. It is seen that most of the computed C–C bonds are about 1.500 Å, while experimentally they are 1.440–1.442

Å. Our results are in agreement with those reported by Schleyer et al. But they are far too long compared with the experimental measurements. Our "best" computed result is 1.486 Å, obtained at the CASSCF(10,8)/6–31+G(d) level, which takes into consideration 10 electrons and 8 orbitals in the active space. The active space in this case consists of the five highest occupied molecular and the three lowest virtual orbitals. The NBO result at the same level reveals that there is no or little π electron delocalized between carbon atoms and they are only localized at the C–O bonds. In the presence of two Na^+ counter ions, one on top and one below the six–membered ring or one Ca^{2+} on top of the ring, C–C bonds become even longer. The additions of the counter ions in this case are of no help. We have not been able to find a theoretical level that would have π electron cloud covering the whole ring, as expected intuitively.

In order to yield a computed structure with bond lengths similar to the experimental results, two approaches can be tried. First, we can carry out the optimization at the level of CASSCF(12,10) with a large basis set such as 6–311+G(2df,p). However, such a calculation is beyond our (hardware) capability. Another way is to mimic the real systems. The network of H-bonding, water molecules and R_4N^+ ions seem to play a crucial role in stabilization of these two forms of the $C_6O_6^{2-}$ anion. So the inclusion of the whole network in the calculation may lead to better results. Clearly this approach is even more expensive in terms of computational cost.

6.4 Conclusions

Ab initio calculations have been applied to identify computationally the experimentally found charge–localized C_{2v} structure of rhodizonate dianion. Also, attempts have been made to find a theoretical level that would yield six C–C bonds in the 1.440 Å range for the charge–delocalized D_{6h} form of $C_6O_6^{2-}$. In the presence of the Na^+ or Ca^{2+} cations, structures with C_2 symmetry instead of those with C_{2v} symmetry of charge–localized form have been found. These structures have one C–C and four C–O double bonds. Most of the computed bond lengths are not in quantitative agreement with the experimental measurements. However, we do get qualitative accord between experiment and calculation. For the charge–delocalized form, we have failed to find a theoretical level that would yield computed C–C

bonds within the experimental range and would have π electron cloud covering the whole ring.

6.5 References

1. West, R.; Niu, H. –Y.; Powell, D. L.; Evans, M. V. *J. Am. Chem. Soc.* **1960**, *82*, 6240.
2. West, R.; Niu, J. In *Nonbenzenoid Aromatics*; Snyder, J. P., Ed.; Academic Press: New York: 1969; Vol. I.
3. West, R., Ed. *Oxocarbons*; Academic Press: New York, 1980.
4. Ito, M.; West, R. *J. Am. Chem. Soc.* **1963**, *85*, 2580.
5. Baenziger, N. C.; Hegenbarth, J. J. *J. Am. Chem. Soc.* **1963**, *85*, 2580.
6. McIntyre, W. M.; Werkema, M. S. *J. Chem. Phys.* **1964**, *42*, 3563.
7. West, R.; Eggerding, D.; Perkins, J.; Handy, D.; Tuazon, E. C. *J. Am. Chem. Soc.* **1979**, *101*, 1710.
8. West, R.; Powell, D. L. *J. Am. Chem. Soc.* **1963**, *85*, 2577.
9. Dewar, M. J. S.; Gleicher, G. J. *J. Am. Chem. Soc.* **1965**, *87*, 685, 692.
10. Dewar, M. J. S.; de Llano, C. *J. Am. Chem. Soc.* **1969**, *91*, 789.
11. Hess, B. A., Jr.; Schaad, L. J. *J. Am. Chem. Soc.* **1971**, *93*, 305, 2431.
12. Schaad, L. J.; Hess, B. A., Jr. *J. Am. Chem. Soc.* **1972**, *94*, 3068.
13. Aihara, J. *J. Am. Chem. Soc.* **1981**, *103*, 1633.
14. Puebla, C.; Ha, T. K. *THEOCHEM* **1986**, *137*, 171.
15. Jug, K. *J. Org. Chem.* **1983**, *48*, 1344.
16. Schleyer, P. v. R.; Najafian, K.; Kiran, B.; Jiao, H. *J. Org. Chem.* **2000**, *65*, 426.
17. Lam, C. K.; Mak, T. C. W. *Angew. Chem.* **2001**, *40*, 3453.
18. Frisch, M. J.; Trucks, G. W.; Schlegel, H. B.; Scuseria, G. E.; Robb, M. A.; Cheeseman, J. R.; Zakrzewski, V. G.; Montgogery, J. A.; Jr.; Stratmann, R.E.; Burant, J. C.; Dapprich, S.; Millam, J. M.; Daniels, A. D.; Kudin, K. N.; Strain, M. C.; Farkas, O.; Tomasi, J.; Barone, V.; Cossi, M.; Cammi, R.; Mennucci, B.; Pomelli, C.; Adamo, C.; Clifford, S.; Ochterski, J.; Petersson, G. A.; Ayala, P. Y.; Cui, Q.; Morokuma, K.; Malick, D. K.; Rabuck, A. D.; Raghavachari, K.; Foresman, J. B.; Cioslowski, J.; Ortiz, J. V.; Baboul, A. G.; Stefanov, B. B.; Liu, G.; Liashenko, A.; Piskorz, P.; Komaromi, I.; Gomperts, R.; Martin, R. L.; Fox, D. J.; Keith, T.; Al-Laham, M. A.; Peng, C. Y.; Nanayakkara, A.; Gonzalez, C.;

Challacombe, M.; Gill, P. M. W.; Johnson, B.; Chen, W.; Wong, M. W.; Andres, J. L.; Gonzalez, C.; Head-Gordon, M.; Replogle, E. S.; Pople, J. A. *GAUSSIAN 98*, Revision A.7; Gaussian, Inc., Pittsburgh PA, 1998.

19. Reed, A. E.; Curtiss, L. A.; Weinhold, F. *Chem. Rev.* **1988**, *88*, 899.

Table 1: Results of the Second–Order Perturbation Theory Analysis of the Fock Matrix in NBO Basis of the Enol Tautomer.

Donor NBO	Acceptor NBO	ΔE^a (kcal mol^{-1})
BDπ C1–C2	BDπ* C3–O9 / C4–O10	34.8
LPπ O7/O8	BDπ* C1–C2	56.0
LPπ O7/O8	BDσ* C1–C3 / C2–C4	17.2
LPπ O9/O10	BDσ* C1–C3 / C2–C4	22.5
LPπ O9/O10	BDσ* C3–C5 / C4–C6	26.7
LPπ O11/O12	BDσ* C3–C5 / C4–C6	24.5
LPπ O11/O12	BDσ* C5–C6	25.7
BDπ* C1–C2	BDπ* C3–O9 / C4–O10	180.0
BDπ* C3–O9 / C4–O10	BDπ* C5–O11 / C6–O12	149.0

[a] The second–order perturbation stabilization energies.

Table 2: Computed C–C and C–O Bond Lengths of the Charge–Delocalized Form of $C_6O_6^{2-}$.

Level of Theory	C–C (Å)	C–O (Å)
HF/6–31G(d)	1.492	1.216
B3 LYP /6–31G(d)	1.498	1.247
B3 LYP /6–311+G(d)	1.501	1.239
B3LYP/6–31+G(2df,p)	1.500	1.240
QCISD/6–31+G(d)	1.499	1.250
B3PW91/aug–cc–pvtz	1.493	1.235
CASSCF(2,4)/6–31+G(d)	1.491	1.218
CASSCF(6,4)/6–31+G(d)	1.492	1.216
CASSCF(6,6)/6–31+G(d)	1.488	1.220
CASSCF(6,8)/6–31+G(d)	1.489	1.224
CASSCF(10,8)/6–31+G(d)	1.486	1.226
Experiment	1.440-1.442	1.245-1.246

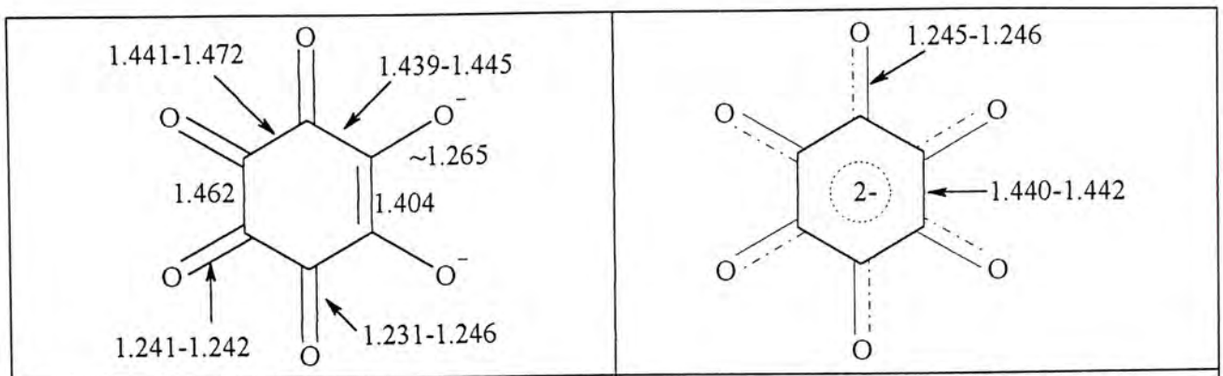

Figure 1. The Experimental Result of the Charge–Localized Form and Charge–Delocalized Form of $C_6O_6^{2-}$.

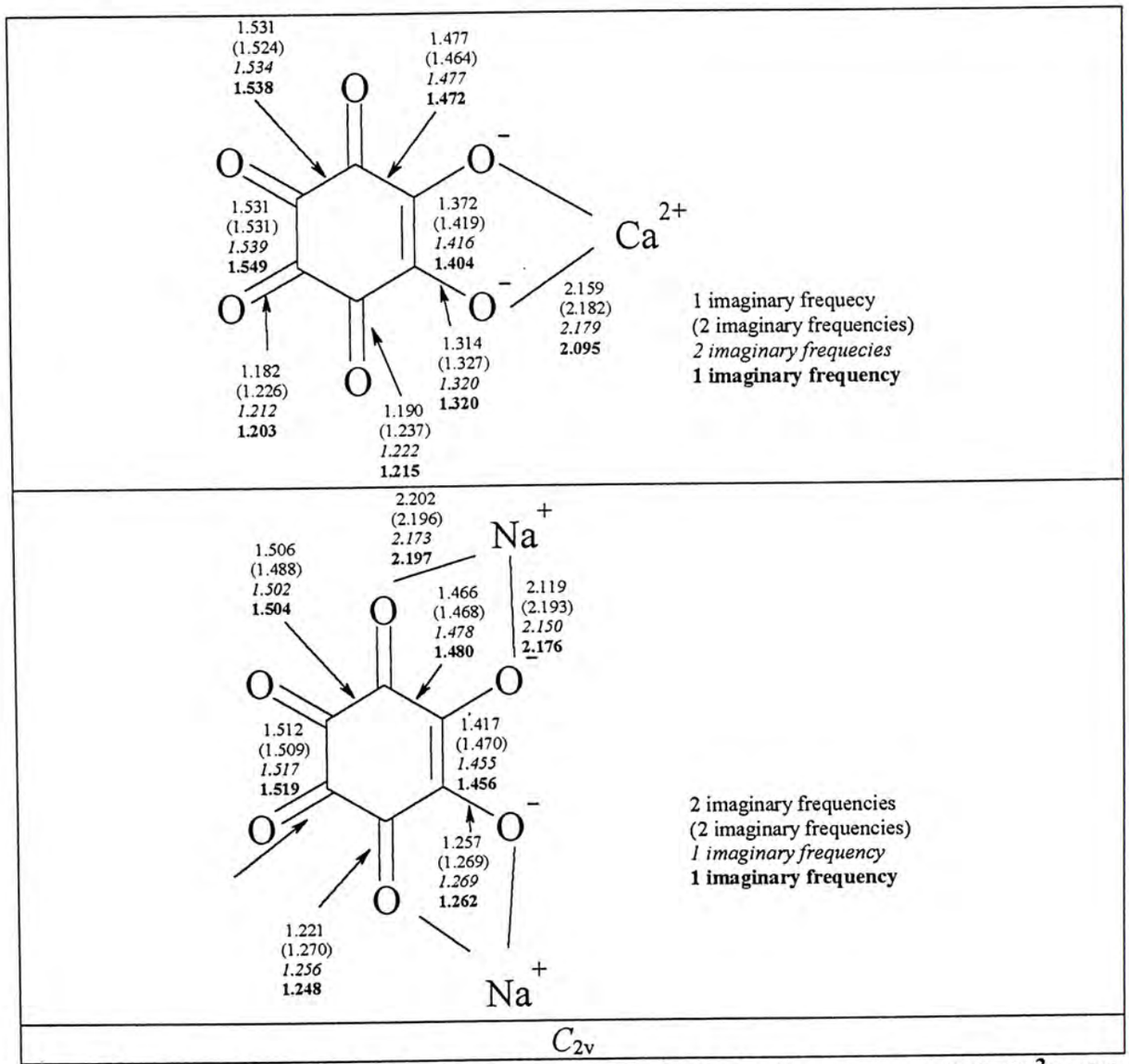

Figure 2. The Computed Results of the Charge–Localized Form of $C_6O_6^{2-}$ with C_{2v} Symmetry at the Levels of HF/6–31G(d) (Normal Font), MP2(Full)/ 6–31G(d) (Bracketed), B3LYP/6–31G(d) (Italic Font), B3LYP/6–311+G(d) (Bold Font).

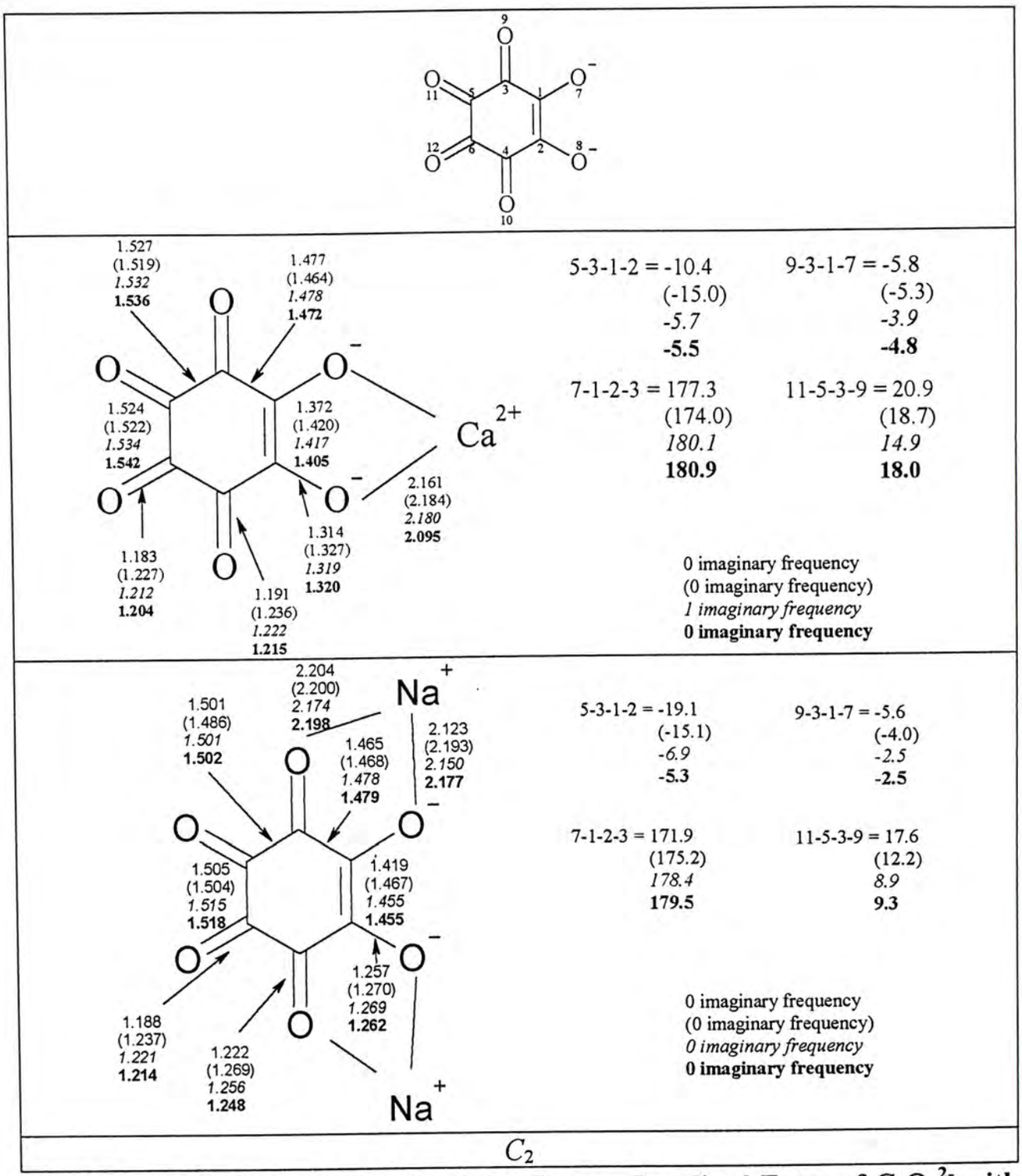

Figure 3. The Computed Results of the Charge–Localized Form of $C_6O_6^{2-}$ with C_2 Symmetry at the Levels of HF/6–31G(d) (Normal Font), MP2(Full)/ 6–31G(d) (Bracketed), B3LYP/6–31G(d) (Italic Font), B3LYP/6–311+G(d) (Bold Font).

Chapter 7

Franck–Condon Factor Simulated Spectra of the Cations of *cis*–2–Butene, *trans*–2–Butene, Isobutene, *cis*–Dichloroethene, and *trans*–Dichloroethene

Abstract

Recently, Ng and his group carried out the measurements for the vibrational bands of the cations of *cis*–2–butene, *trans*–2–butene, isobutene, *cis*–dichloroethene, and *trans*–dichloroethene by using the pulsed field ionization–photoelectron (PFI–PE) detection technique with vacuum ultraviolet (VUV) lasers. In this chapter, we will interpret the vibrational spectra by the facilitation of the second–order Møller–Plesset perturbation theory (MP2) calculations and spectral simulations based on the Franck–Condon (FC) principle. Using the harmonic vibrational frequencies and Franck–Condon factor (FCF) simulation for the cations calculated at the MP2 level of theory, we have assigned the PFI–PE vibrational bands observed for those species. Except the isobutene cation, FCF program successfully reproduces the simulated spectra with most of the peak positions and relative intensities being similar to the experimental spectra. However, many weak peaks in the experimental and the simulated spectra are not matched. In any event, FCF simulated spectra are useful to identify the conformation of the molecules.

where $\mathbf{Q}^G$ and $\mathbf{Q}^E$ are the normal mode coordinates of the ground and excited states, respectively, **W** is the Duschinsky rotational matrix and k^E is the displacement of the potential minima of the ground state projected in the normal coordinates for the excited state. The matrix W and the vector k^E are given[6,7] as

$$\mathbf{W} = (L^E)^T L^G$$

$$k^E = (L^E)^T \mathbf{M}^{1/2} \Delta X$$

where the L^G and L^E matrix are determined by diagonalizing the mass–weighted Cartesian force constant matrices for the ground and excited states and the superscript T stands for transposition. Also, $M^{1/2}$ is the diagonal matrix whose diagonal elements are square roots of the atomic masses, and ΔX is the vector difference of the equilibrium geometries between two states in the Cartesian coordinate. The N–dimensional FC integrals are calculated with a general recurrence formula.[8] In the simulations, the maximum total vibrational quanta of the ground and excited states are set to be 3 and 5, respectively. Therefore, the transitions involved are from $v'' = 0$ to a maximum of $v' = 5$.

The simulated peak positions were determined by the calculated vibrational frequencies of the two states, which served as the input to the Yang program. The peak intensities are determined by the FCF or the square of the overlap integral between two vibrational levels; they are the main pieces of information calculated by the program.

7.3 Results and Discussion

With the help of the theoretical calculations and FCF simulations, we have assigned the experimental vibrational bands resolved in the PFI–PE spectra for all molecules. The peaks within the range of the experimental observation in the FCF simulated spectra are also assigned. It should be noted that the weak peaks in the simulated spectra are not matched with the experimental results. Hence we did not make assignments for these peaks.

7.3.1 *cis*–2–Butene Cation. The calculated ionization energy (IE) of *cis*–2–butene is 9.17 eV, which is in very good agreement with the experimental result of 9.13 eV.[1] The experimental and simulated spectra (from MP2 calculation results) of the *cis*–2–butene cation are displayed in Figures 1a and 1b. The detailed

peak assignments from the MP2 calculation and the FCF simulation, together with the experimental results, are summarized in Table 1.

The MP2 calculation indicates that there are 30 vibrational modes for the *cis*–2–butene cation with harmonic frequencies in the range of ≈20–3200 cm^{-1}. The lowest calculated frequency is 23 cm^{-1} and is attributed to the ν_1^+ mode. The two lowest vibrational frequencies observed at 61 and 95 cm^{-1} are attributed to the $2\nu_1^+$ and ν_2^+ modes, respectively. The observed $2\nu_1^+$ frequency is in fair accord with MP2 and FCF $2\nu_1^+$ prediction (46 and 47 cm^{-1}, respectively), while the experimental ν_2^+ frequency is in good agreement with the MP2 and FCF ν_2^+ value (92 cm^{-1} and 94 cm^{-1}, respectively). The experimental frequencies 128, 210 and 247 cm^{-1}, which do not match any predicted vibrational frequencies, are assigned to be the combination modes $4\nu_1^+$, $2\nu_2^+$ and $\nu_1^+ + \nu_3^+$, respectively. The PFI–PE bands at 179 and 293 cm^{-1} are assigned as ν_3^+ and ν_4^+ and they match with the MP2/FCF predictions. The PFI–PE peak at 368 cm^{-1} is attributed to the $2\nu_3^+$ mode and this mode is also predicted in the FCF simulated spectrum. The PFI–PE bands at 730 and 756 cm^{-1} are assigned to be the ν_6^+ and ν_7^+ modes. The observed frequency at 978 cm^{-1} is attributed as ν_{10}^+. This assignment is in poor accord with the MP2 calculation (939 cm^{-1}) and is in good accord with the FCF simulation (969 cm^{-1}). Based on the comparison between MP2 frequencies and FCF simulation, the PFI–PE bands at 1038, 1263, 1298, 1443, and 1553 cm^{-1} can be assigned with some confidence as ν_{12}^+, ν_{14}^+, ν_{15}^+, ν_{20}^+, and ν_{22}^+, respectively. Finally, the PFI–PE peaks at 1095 and 1398 cm^{-1} are attributed to be the combination mode $2\nu_1^+ + \nu_{12}^+$, and ν_{18}^+ respectively.

7.3.2 *trans*–2–Butene Cation. The calculated IE of *trans*–2–butene is 9.18 eV, which again is in good agreement with the experimental result of 9.13 eV. The experimental and simulated spectra of the *trans*–2–butene cation are shown in Figures 2a and 2b. The detailed peak assignments from the MP2 calculation and the FCF simulation, together with experimental results, are summarized in Table 2.

The MP2 calculation show that there are 30 vibrational modes for the *trans*–2–butene cation with harmonic frequencies in range of ≈100–3200 cm^{-1}. The experimental frequencies at 104, 127, and 133 cm^{-1} are attributed to the ν_1^+, ν_2^+, and

ν_3^+ modes, respectively. They are predicted by the MP2 calculation, but not by FCF simulation. The PFI–PE bands at 212 and 264 cm^{-1} are assigned as $2\nu_1^+$, and ν_4^+, respectively, and these modes are simulated in the FCF spectrum. The observed peaks at 397 and 536 cm^{-1}, which do not match in either FCF simulation or MP2 calculation, are attributed to the $\nu_3^+ + \nu_4^+$, and $2\nu_4^+$ modes, respectively. The measured bands at 492, 801, 874, 1265, 1308, 1411, 1479, and 1567 cm^{-1} are assigned to be ν_5^+, ν_8^+, ν_9^+, ν_{14}^+, ν_{16}^+, ν_{20}^+, ν_{21}^+, and ν_{22}^+, respectively. Among them, ν_8^+, ν_{14}^+, ν_{16}^+, ν_{20}^+, and ν_{22}^+ are intense peaks and they are successfully reproduced in the simulated spectrum with similar relative intensity. However, there is an intense peak at 739 cm^{-1} in the PFI–PE spectrum, but it is absent in the simulated spectrum. The PFI–PE peaks at 739, 1165, 1371, and 1509 cm^{-1} are attributed as ν_6^+, ν_{12}^+, $\nu_1^+ + \nu_{14}^+$, and $\nu_1^+ + \nu_{20}^+$, respectively. Three observed peaks at 1690, 1827, and 2063 cm^{-1}, which can also be found in the simulated spectrum, are assigned to be the combination modes $\nu_1^+ + \nu_{22}^+$, $\nu_4^+ + \nu_{22}^+$, and $\nu_8^+ + \nu_{14}^+$, respectively.

7.3.3 *cis*–Dichloroethene Cation. The calculated IE of *cis*–dichloroethene is 9.65 eV, which is in excellent agreement with the experimental result of 9.66 eV. The experimental and simulated spectra of the *cis*–dichloroethene cation are shown in Figures 3a and 3b, respectively. The detailed peak assignments from the MP2 calculation and the FCF simulation, together with experimental results, are summarized in Table 3. Figures 3a and 3b indicate that the FCF program produces simulated results that are in very good accord with experiment, in terms of either peak positions or relative intensities.

The MP2 calculation show that there are 12 vibrational modes for the cation with harmonic frequencies in the range of ≈180–3200 cm^{-1}. Based on the comparison between MP2 frequencies and FCF simulation, the PFI–PE bands at 182, 581, 810, 995, 1197, 1381, and 1429 cm^{-1} can be assigned with some confidence as ν_1^+, ν_3^+, ν_5^+, ν_7^+, ν_8^+, $\nu_1^+ + \nu_8^+$, and ν_{10}^+, respectively. The observed peaks at 280, 730, 901, 1349 cm^{-1}, which are predicted in MP2 frequencies but not in the FCF simulated spectrum, are attributed to the ν_2^+, ν_4^+, ν_6^+, and ν_9^+ modes, respectively. There are five peaks observed in the PFI–PE spectrum but not in the FCF simulation or the MP2 calculation. Among them, the observed peaks at 560,

685, 1091, and 1300 cm^{-1} are assigned to be $2\nu_2^+$, $2\nu_1^+ + \nu_2^+$, $\nu_1^+ + \nu_6^+$, and $2\nu_1^+ + \nu_6^+$, respectively. However, the observed peak at 147 cm^{-1}, which is out of the range of the MP2 frequencies, cannot be assigned to any mode. The observed peak at 182 cm^{-1} is assigned as ν_1^+ and it is in excellent agreement with the lowest peak of the MP2 results (180 cm^{-1}) and FCF simulation (179 cm^{-1}). The observed peak at 147 cm^{-1} may arise from noise during the measurement, but we cannot rule out errors in the MP2 calculation.

7.3.4 *trans*–Dichloroethene Cation. The calculated IE of *trans*–dichloroethene is 9.61 eV, which is in excellent agreement with the experimental result of 9.63 eV. The experimental and simulated spectra of the *trans*–dichloroethene cation are shown in Figures 4a and 4b, respectively. The detailed peak assignments from the MP2 calculation and the FCF simulation, together with experimental results, are summarized in Table 4. Figures 4a and 4b also show that the FCF program produces simulated results that are in very good agreement with experiment, in terms of both peak positions and relative intensities.

The MP2 calculation indicates that there are 12 vibrational modes for the cation with harmonic frequencies in the range of ≈160–3200 cm^{-1}. Based on the comparison between MP2 frequencies and FCF simulation, the PFI–PE bands at 369, 739, 947, 1076, 1261, 1315, and 1454 cm^{-1} can be assigned as ν_3^+, $2\nu_3^+$, ν_6^+, ν_7^+, ν_9^+, $\nu_3^+ + \nu_6^+$, and ν_{10}^+, respectively. The PFI–PE peaks at 164, 839 and 226 cm^{-1} are attributed to the ν_1^+, ν_2^+ and ν_4^+ modes, respectively. The remaining PFI–PE bands at 324, 480, 537, 637, 699, 1107, and 1205 cm^{-1}, which do not match in either FCF simulation or MP2 calculation, are attributed to the $2\nu_1^+$, $3\nu_1^+$, $\nu_1^+ + \nu_3^+$, $4\nu_1^+$, $2\nu_1^+ + \nu_3^+$, $\nu_1^+ + \nu_6^+$, and $\nu_3^+ + \nu_4^+$ modes, respectively.

7.3.5 Isobutene Cation. The calculated IE of isobutene is 9.25 eV, which is in very good agreement with the experimental result of 9.22 eV. The experimental and simulated spectra are shown in Figures 5a and 5b, respectively. The detailed peak assignments from the MP2 calculation and the FCF simulation, together with experimental results, are summarized in Table 5. Figures 5a and 5b indicate that the FCF program can only produce a few peaks that are in good agreement with experiment.

The MP2 calculation shows that there are 30 vibrational modes with harmonic frequencies in range of ≈160–3200 cm^{-1}. As can be seen in the experimental spectrum, the peaks are broad, especially in the ranges of 100–300 and 1400–1800 cm^{-1}. This increases the complexity of peak assignments. The lowest vibrational mode observed at 127 cm^{-1} is attributed to the ν_1^+ mode and it is in fair accord with the MP2 prediction of 101 cm^{-1}. With the help from the FCF simulated spectrum, the experimental frequencies at 151, 209, 327, and 522 cm^{-1} are attributed to the ν_2^+, $2\nu_1^+$, $2\nu_2^+$, and $3\nu_2^+$ modes, respectively. The PFI–PE peaks at 192 and 216 cm^{-1} cannot be assigned because they do not match with any combination or theoretical predictions. The PFI–PE bands at 260, 634, 771, and 828 cm^{-1} are assigned to be ν_3^+, $\nu_3^+ + \nu_4^+$, ν_7^+, and ν_8^+, respectively. The PFI–PE peaks at 1313, 1408, 1438, 1465, 1500, and 1540 cm^{-1} are attributed to the ν_{14}^+, ν_{18}^+, ν_{19}^+, ν_{20}^+, ν_{21}^+, and ν_{22}^+ modes, respectively, and they are only predicted by the MP2 frequencies. The experimental frequencies at 1233, 1514, 1559, 1620, 1705, and 1759 are assigned as the combination modes $2\nu_1^+ + \nu_{12}^+$, $\nu_2^+ + \nu_{17}^+$, $\nu_1^+ + \nu_{19}^+$, $\nu_1^+ + \nu_{21}^+$, $2\nu_1^+ + \nu_{21}^+$, and $\nu_3^+ + \nu_{21}^+$, respectively. It is clear that the severe noise in the experimental spectrum causes uncertainty in the peak assignment.

7.4 Conclusions

Using the MP2 harmonic vibrational frequencies and FCF simulation for the cations of *cis*–2–butene, *trans*–2–butene, isobutene, *cis*–dichloroethene, and *trans*–dichloroethene, we have assigned the PFI–PE vibrational bands observed for those species. Excepting the isobutene cation, the FCF program successfully reproduces the simulated spectra that are in good accord with the experimental measurements, both in terms of peak positions and relative intensities. However, many weak peaks in the experimental and the simulated spectra are not matched well. In any event, FCF simulated spectra are useful to identify the conformation of the molecules.

7.5 References

1. Ng, C. Y.; Woo. H. K.; Zhan, J.; Lau, K. –C.; Cheung, Y. S. *J. Chem. Phys.* **2002**, *116*, 8803.

2. Frisch, M. J.; Trucks, G. W.; Schlegel, H. B.; Scuseria, G. E.; Robb, M. A.; Cheeseman, J. R.; Zakrzewski, V. G.; Montgogery, J. A.; Jr.; Stratmann, R.E.; Burant, J. C.; Dapprich, S.; Millam, J. M.; Daniels, A. D.; Kudin, K. N.; Strain, M. C.; Farkas, O.; Tomasi, J.; Barone, V.; Cossi, M.; Cammi, R.; Mennucci, B.; Pomelli, C.; Adamo, C.; Clifford, S.; Ochterski, J.; Petersson, G. A.; Ayala, P. Y.; Cui, Q.; Morokuma, K.; Malick, D. K.; Rabuck, A. D.; Raghavachari, K.; Foresman, J. B.; Cioslowski, J.; Ortiz, J. V.; Baboul, A. G.; Stefanov, B. B.; Liu, G.; Liashenko, A.; Piskorz, P.; Komaromi, I.; Gomperts, R.; Martin, R. L.; Fox, D. J.; Keith, T.; Al-Laham, M. A.; Peng, C. Y.; Nanayakkara, A.; Gonzalez, C.; Challacombe, M.; Gill, P. M. W.; Johnson, B.; Chen, W.; Wong, M. W.; Andres, J. L.; Gonzalez, C.; Head-Gordon, M.; Replogle, E. S.; Pople, J. A. *GAUSSIAN 98*, Revision A.7; Gaussian, Inc., Pittsburgh PA, 1998.
3. Yang D. S.; Hackett, P. A. *J. Elect. Spectro. and Rel. Phenom.* **2000**, *106*, 153.
4. Duschinsky, F. *Acta Physicochim URSS* **1937**, *7*, 551
5. Yamaguchi, M.; Momose, T.; Shida, T. *J. Chem. Phys.* **1990**, *93*, 4211.
6. Doktorov, E. V.; Malkin, I. A.; Man'ko, V. I. *J. Mol. Spectrosc.* **1976**, *64*, 302.
7. Doktorov, E. V.; Malkin, I. A.; Man'ko, V. I. *J. Mol. Spectrosc.* **1975**, *56*, 1.
8. Lupka H.; Cribb, P. H. *J. Chem. Phys.* **1986**, *83*, 1303.

Table 1: Comparison of Experimental and Theoretical Vibrational Frequencies (cm^{-1}) for *cis*–2–Butene Cation.

Symmetry	Scaled MP2 frequency	MP2 Assignment	FCF	FCF Assignment	PFI–PE	PFI–PE Assignment
a_2	23	ν_1^+				
			47	$2\nu_1^+$	61	$2\nu_1^+$
b_1	92	ν_2^+	94	ν_2^+	95	ν_2^+
					128	$4\nu_1^+$
a_2	176	ν_3^+	185	ν_3^+	179	ν_3^+
					210	$2\nu_2^+$
					247	$\nu_3^+ + \nu_1^+$
a_1	285	ν_4^+	284	ν_4^+	293	ν_4^+
			352	$2\nu_3^+$	368	$2\nu_3^+$
b_2	553	ν_5^+				
b_1	747	ν_6^+			730	ν_6^+
a_2	765	ν_7^+			756	ν_7^+
a_1	824	ν_8^+	824	ν_8^+		
b_1	877	ν_9^+				
b_2	939	ν_{10}^+	969	ν_{10}^+	978	ν_{10}^+
a_2	1036	ν_{11}^+				
a_1	1038	ν_{12}^+	1038	ν_{12}^+	1038	ν_{12}^+
			1085	$\nu_{12}^+ + 2\nu_1^+$	1095	$\nu_{12}^+ + 2\nu_1^+$
b_2	1179	ν_{13}^+				
a_1	1276	ν_{14}^+	1276	ν_{14}^+	1263	ν_{14}^+
a_1	1305	ν_{15}^+	1305	ν_{15}^+	1298	ν_{15}^+
b_2	1308	ν_{16}^+				
b_2	1386	ν_{17}^+				
a_2	1401	ν_{18}^+			1398	ν_{18}^+
b_1	1414	ν_{19}^+				
a_1	1434	ν_{20}^+	1434	ν_{20}^+	1443	ν_{20}^+
b_2	1486	ν_{21}^+	1480	ν_{21}^+		
a_1	1568	ν_{22}^+	1568	ν_{22}^+	1553	ν_{22}^+
b_2	2942	ν_{23}^+				
a_1	2947	ν_{24}^+				
b_1	2991	ν_{25}^+				
a_2	2992	ν_{26}^+				
b_2	3120	ν_{27}^+				
a_1	3134	ν_{28}^+				
b_2	3150	ν_{29}^+				
a_1	3161	ν_{30}^+				

Table 2: Comparison of Experimental and Theoretical Vibrational Frequencies (cm^{-1}) for *trans*–2–Butene Cation.

Symmetry	Scaled MP2 frequency	MP2 Assignment	FCF	FCF Assignment	PFI–PE	PFI–PE Assignment
a_u	102	ν_1^+			104	ν_1^+
a_u	128	ν_2^+			127	ν_2^+
b_g	130	ν_3^+			133	ν_3^+
			203	$2\nu_1^+$	212	$2\nu_1^+$
			231	$\nu_1^+ + \nu_3^+$		
b_u	277	ν_4^+	261	ν_4^+	264	ν_4^+
					397	$\nu_3^+ + \nu_4^+$
a_g	483	ν_5^+	482	ν_5^+	492	ν_5^+
					536	$2\nu_4^+$
b_g	758	ν_6^+			739	ν_6^+
a_u	770	ν_7^+				
a_g	830	ν_8^+	830	ν_8^+	801	ν_8^+
a_u	883	ν_9^+	871	ν_9^+	874	ν_9^+
b_u	934	ν_{10}^+				
b_g	1042	ν_{11}^+				
b_u	1140	ν_{12}^+			1165	ν_{12}^+
a_g	1195	ν_{13}^+				
a_g	1271	ν_{14}^+	1271	ν_{14}^+	1265	ν_{14}^+
b_u	1286	ν_{15}^+				
a_g	1320	ν_{16}^+	1319	ν_{16}^+	1308	ν_{16}^+
b_u	1321	ν_{17}^+				
					1371	$\nu_1^+ + \nu_{14}^+$
b_g	1406	ν_{18}^+				
a_u	1408	ν_{19}^+				
a_g	1429	ν_{20}^+	1429	ν_{20}^+	1411	ν_{20}^+
b_u	1467	ν_{21}^+	1475	ν_{21}^+	1479	ν_{21}^+
					1509	$\nu_1^+ + \nu_{20}^+$
a_g	1590	ν_{22}^+	1590	ν_{22}^+	1567	ν_{22}^+
			1690	$\nu_1^+ + \nu_{22}^+$	1690	$\nu_1^+ + \nu_{22}^+$
			1850	$\nu_4^+ + \nu_{22}^+$	1827	$\nu_4^+ + \nu_{22}^+$
			2101	$\nu_8^+ + \nu_{14}^+$	2063	$\nu_8^+ + \nu_{14}^+$
b_u	2940	ν_{23}^+				
a_g	2943	ν_{24}^+				
a_u	2989	ν_{25}^+				
b_g	2992	ν_{26}^+				
a_g	3115	ν_{27}^+				
b_u	3123	ν_{28}^+				
a_g	3136	ν_{29}^+				
b_u	3137	ν_{30}^+				

Table 3: Comparison of Experimental and Theoretical Vibrational Frequencies (cm^{-1}) for *cis*–Dichloroethene Cation.

Symmetry	Scaled MP2 frequency	MP2 Assignment	FCF	FCF Assignment	PFI–PE	PFI–PE Assignment
					147	
a_1	180	ν_1^+	179	ν_1^+	182	ν_1^+
a_2	290	ν_2^+			280	ν_2^+
					560	$2\nu_2^+$
b_2	582	ν_3^+	580	ν_3^+	581	ν_3^+
					685	$2\nu_1^+ + \nu_2^+$
b_1	747	ν_4^+			730	ν_4^+
a_1	827	ν_5^+	825	ν_5^+	810	ν_5^+
a_2	926	ν_6^+			901	ν_6^+
b_2	997	ν_7^+	1003	ν_7^+	995	ν_7^+
					1091	$\nu_1^+ + \nu_6^+$
a_1	1212	ν_8^+	1211	ν_8^+	1197	ν_8^+
					1300	$2\nu_1^+ + \nu_6^+$
b_2	1357	ν_9^+			1349	ν_9^+
			1390	$\nu_1^+ + \nu_8^+$	1381	$\nu_1^+ + \nu_8^+$
a_1	1444	ν_{10}^+	1443	ν_{10}^+	1429	ν_{10}^+
b_2	3132	ν_{11}^+				
a_1	3146	ν_{12}^+				

Table 4: Comparison of Experimental and Theoretical Vibrational Frequencies (cm^{-1}) for *trans*–Dichloroethene Cation.

Symmetry	Scaled MP2 frequency	MP2 Assignment	FCF	FCF Assignment	PFI–PE	PFI–PE Assignment
a_u	167	ν_1^+			164	ν_1^+
b_u	246	ν_2^+			226	ν_2^+
					324	$2\nu_1^+$
a_g	367	ν_3^+	365	ν_3^+	369	ν_3^+
					480	$3\nu_1^+$
					537	$\nu_1^+ + \nu_3^+$
					637	$4\nu_1^+$
					699	$2\nu_1^+ + \nu_3^+$
			730	$2\nu_3^+$	739	$2\nu_3^+$
a_u	863	ν_4^+			839	ν_4^+
b_g	896	ν_5^+				
a_g	967	ν_6^+	965	ν_6^+	947	ν_6^+
b_u	1011	ν_7^+	1095	ν_7^+	1076	ν_7^+
					1107	$\nu_1^+ + \nu_6^+$
					1205	$\nu_3^+ + \nu_4^+$
b_u	1247	ν_8^+				
a_g	1263	ν_9^+	1263	ν_9^+	1261	ν_9^+
			1330	$\nu_3^+ + \nu_6^+$	1315	$\nu_3^+ + \nu_6^+$
a_g	1464	ν_{10}^+	1463	ν_{10}^+	1454	ν_{10}^+
b_u	3138	ν_{11}^+				
a_g	3138	ν_{12}^+				

Table 5: Comparison of Experimental and Theoretical Vibrational Frequencies (cm^{-1}) for Isobutene Cation.

Symmetry	Scaled MP2 frequency	MP2 Assignment	FCF	FCF Assignment	PFI–PE	PFI–PE Assignment
b	101	ν_1^+			127	ν_1^+
a	174	ν_2^+	174	ν_2^+	151	ν_2^+
					192	
			202	$2\nu_1^+$	209	$2\nu_1^+$
					216	
a	267	ν_3^+			260	ν_3^+
			349	$2\nu_2^+$	327	$2\nu_2^+$
			377	$2\nu_1^+ + \nu_2^+$		
a	395	ν_4^+				
b	404	ν_5^+				
b	439	ν_6^+				
			523	$3\nu_2^+$	522	$3\nu_2^+$
			550	$3\nu_1^+ + \nu_2^+$		
					634	$\nu_3^+ + \nu_4^+$
a	756	ν_7^+			771	ν_7^+
a	855	ν_8^+			828	ν_8^+
b	882	ν_9^+				
b	960	ν_{10}^+				
b	990	ν_{11}^+				
a	1036	ν_{12}^+	1024	ν_{12}^+		
b	1045	ν_{13}^+				
					1233	$2\nu_1^+ + \nu_{12}^+$
b	1310	ν_{14}^+			1313	ν_{14}^+
a	1322	ν_{15}^+				
a	1348	ν_{16}^+				
b	1358	ν_{17}^+				
b	1396	ν_{18}^+			1408	ν_{18}^+
a	1422	ν_{19}^+			1438	ν_{19}^+
b	1475	ν_{20}^+			1465	ν_{20}^+
a	1479	ν_{21}^+			1500	ν_{21}^+
			1522	$\nu_2^+ + \nu_{17}^+$	1514	$\nu_2^+ + \nu_{17}^+$
a	1546	ν_{22}^+			1540	ν_{22}^+
					1559	$\nu_1^+ + \nu_{19}^+$
					1620	$\nu_1^+ + \nu_{21}^+$
			1696	$2\nu_1^+ + \nu_{21}^+$	1705	$2\nu_1^+ + \nu_{21}^+$
					1759	$\nu_3^+ + \nu_{21}^+$
b	2908	ν_{23}^+				
a	2920	ν_{24}^+				
a	3053	ν_{25}^+				
b	3056	ν_{26}^+				
a	3114	ν_{27}^+				
a	3129	ν_{28}^+				
b	3130	ν_{29}^+				
b	3235	ν_{30}^+				

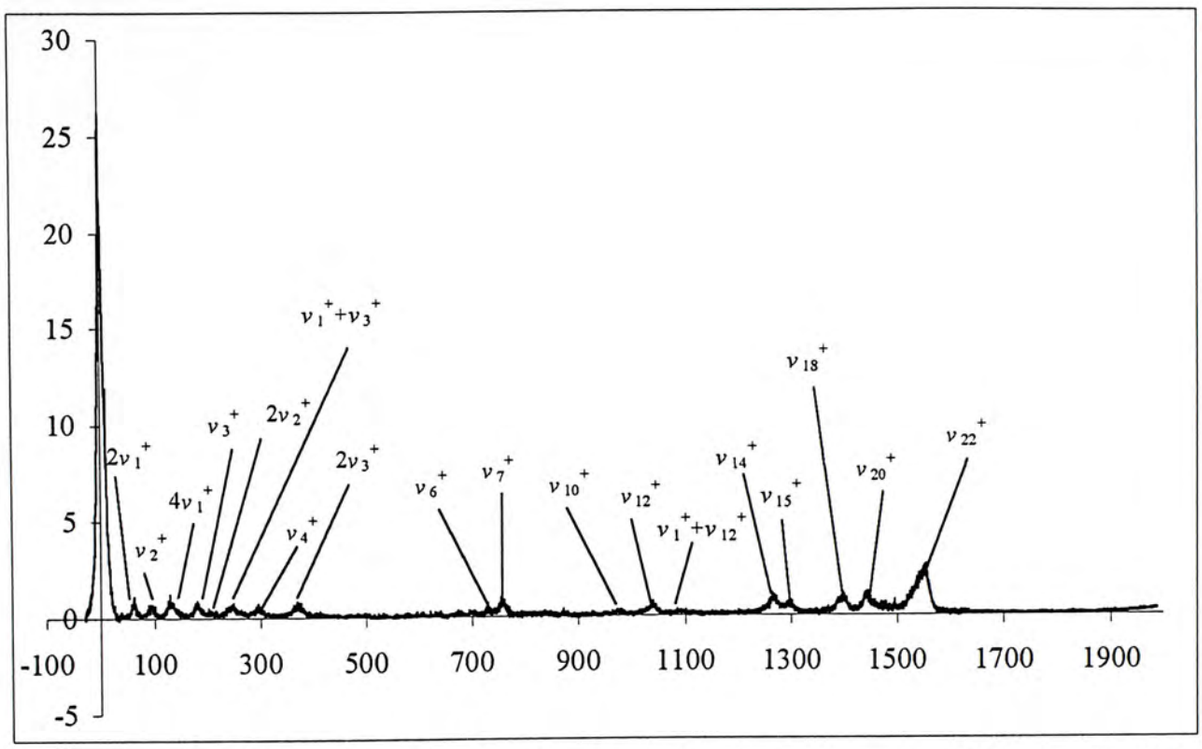

Figure 1a. VUV–PFI–PE Spectrum of *cis*–2–Butene Cation, Plotting I(PFI–PE)/I(hv) (Arb. Unit) against Energy above IE (cm^{-1}).

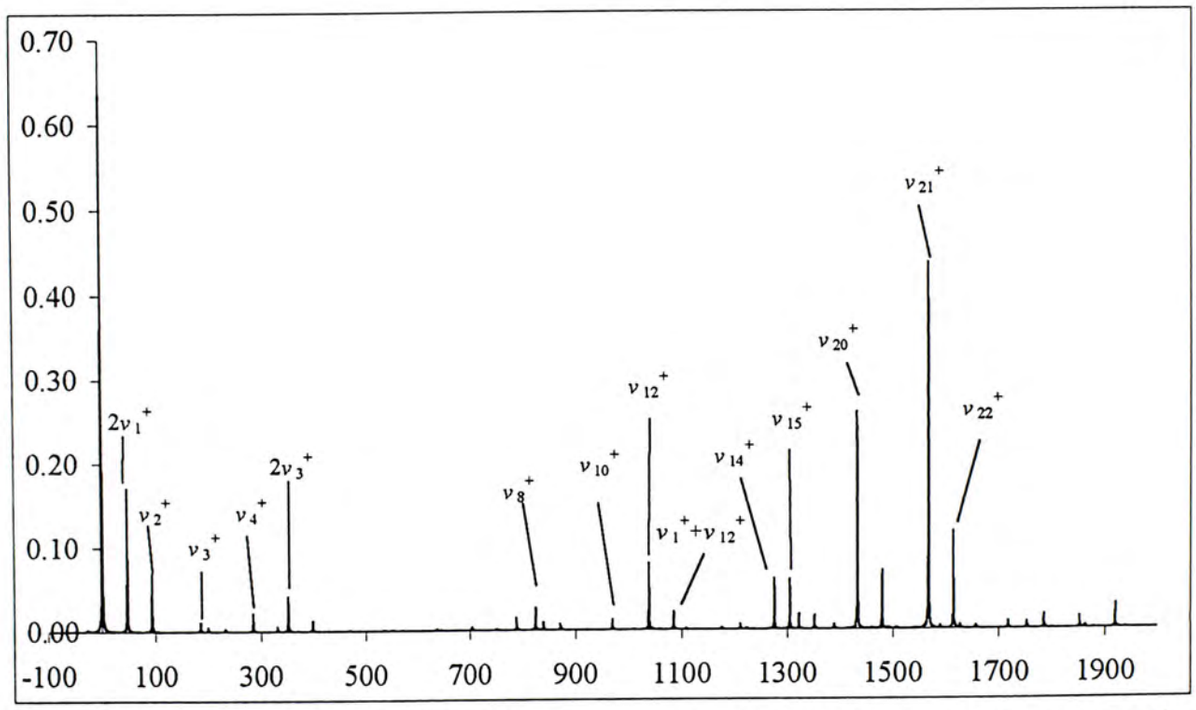

Figure 1b. FCF Simulated Spectrum of *cis*–2–Butene Cation, Plotting I(PFI–PE)/I(hv) (Arb. Unit) against Energy above IE (cm^{-1}).

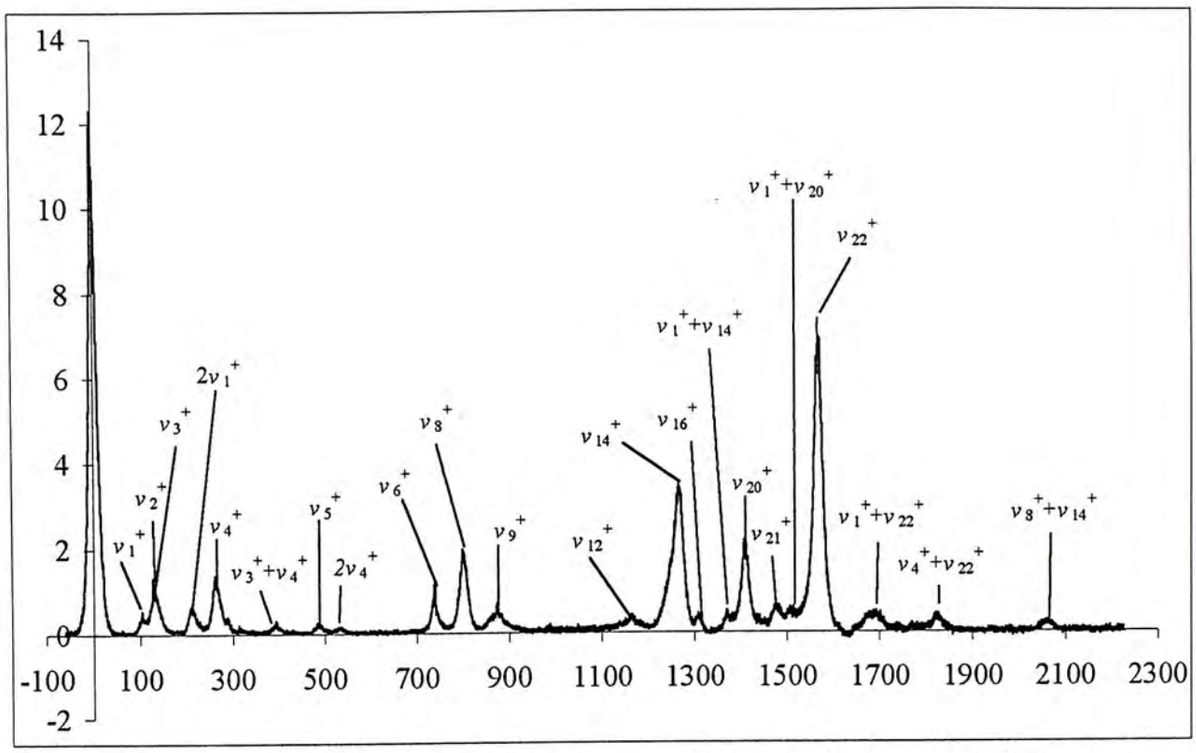

Figure 2a. VUV–PFI–PE Spectrum of *trans*–2–Butene Cation, Plotting I(PFI–PE)/I(hv) (Arb. Unit) against Energy above IE (cm^{-1}).

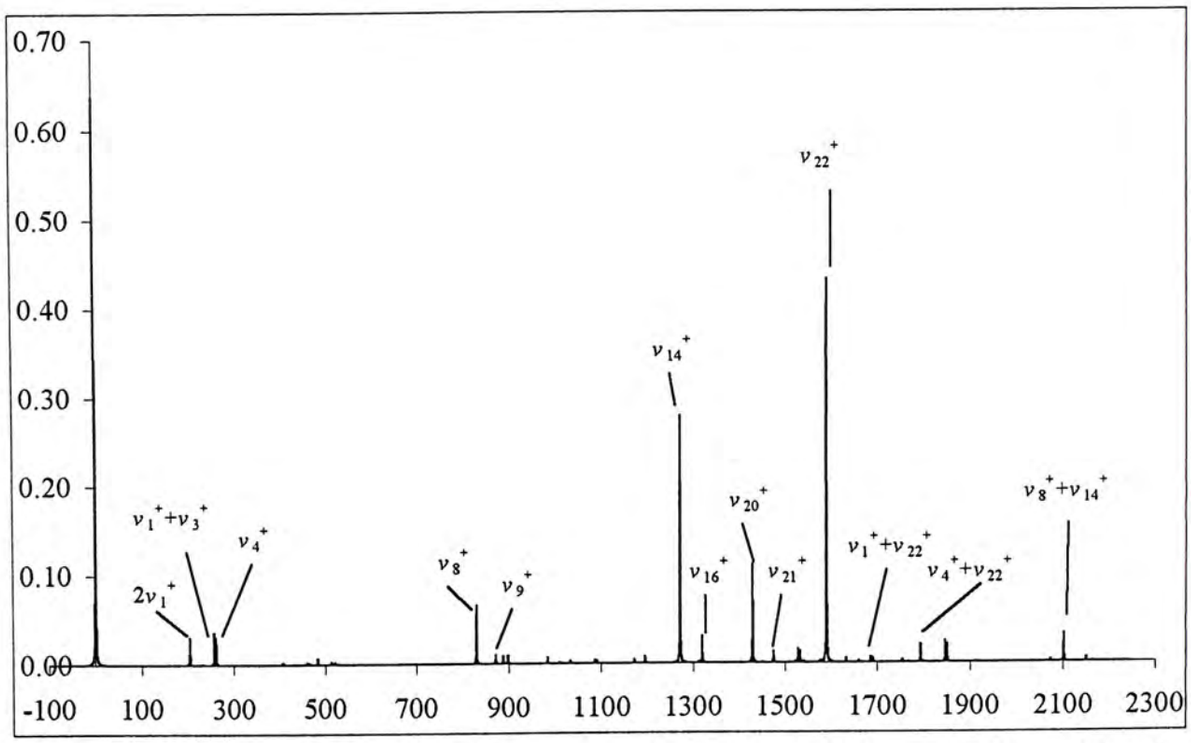

Figure 2b. FCF Simulated Spectrum of *trans*–2–Butene Cation, Plotting I(PFI–PE)/I(hv) (Arb. Unit) against Energy above IE (cm^{-1}).

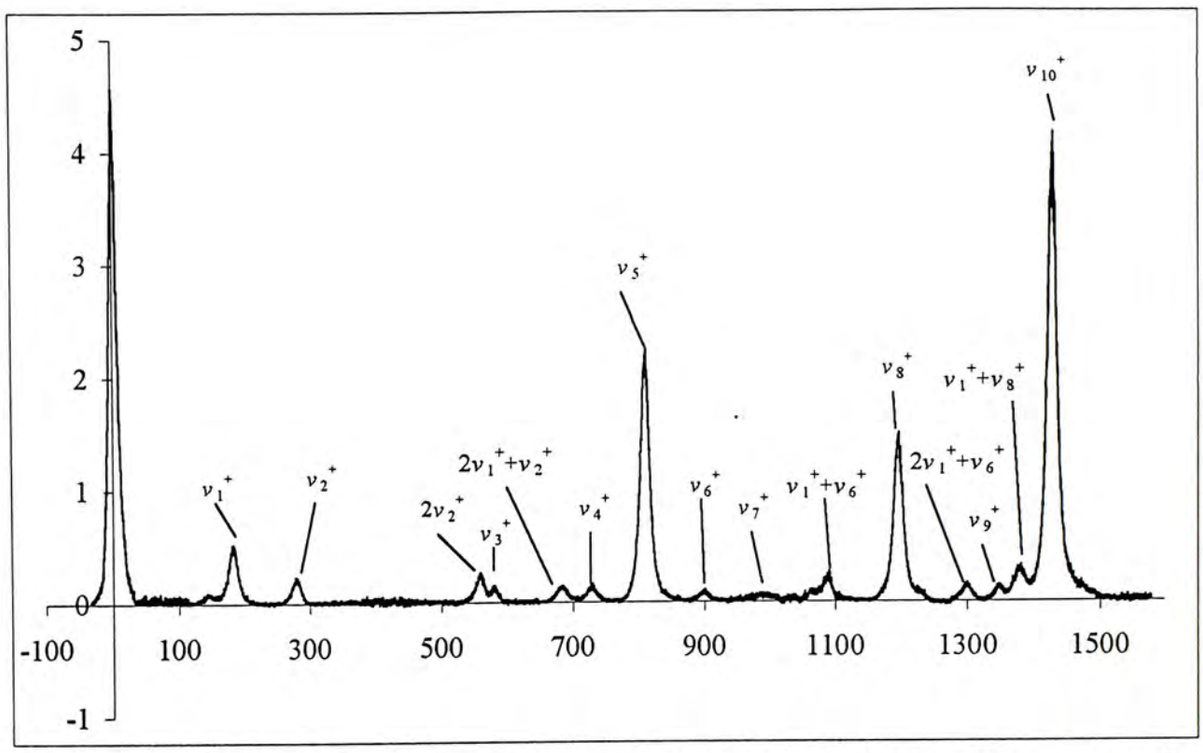

Figure 3a. VUV–PFI–PE Spectrum of *cis*–Dichloroethene Cation, Plotting I(PFI–PE)/I(hv) (Arb. Unit) against Energy above IE (cm^{-1}).

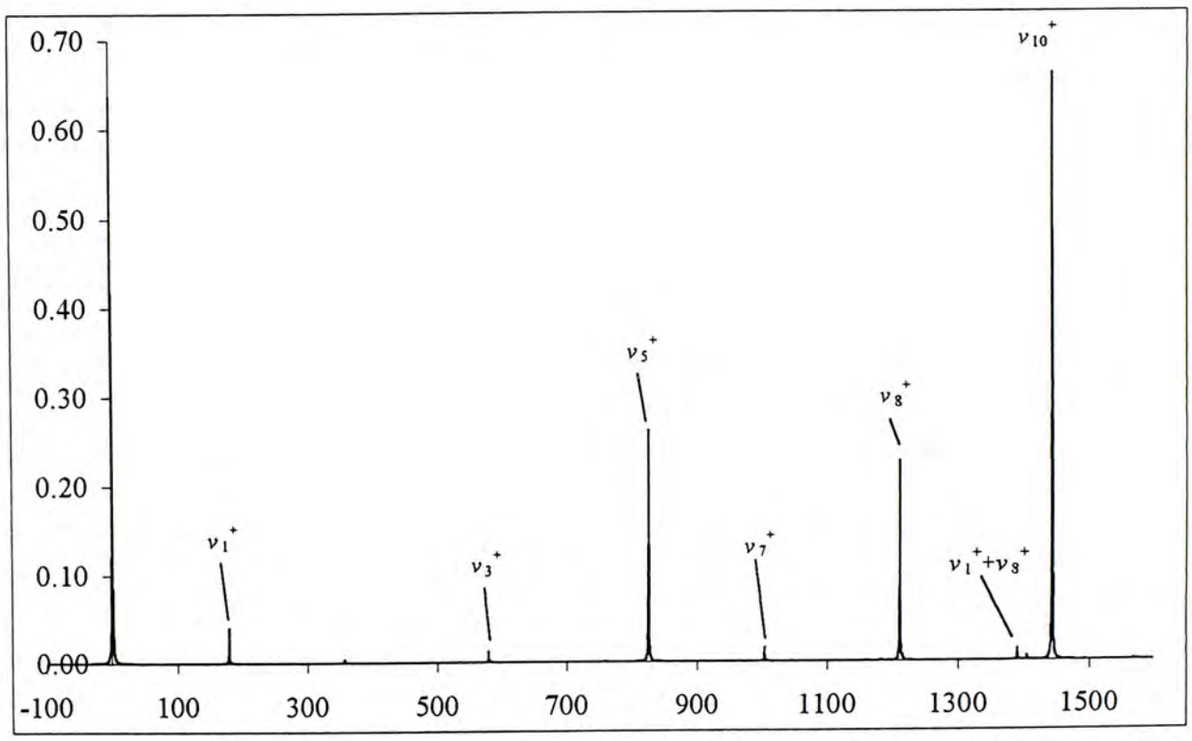

Figure 3b. FCF Simulated Spectrun of *cis*–Dichloroethene Cation, Plotting I(PFI–PE)/I(hv) (Arb. Unit) against Energy above IE (cm^{-1}).

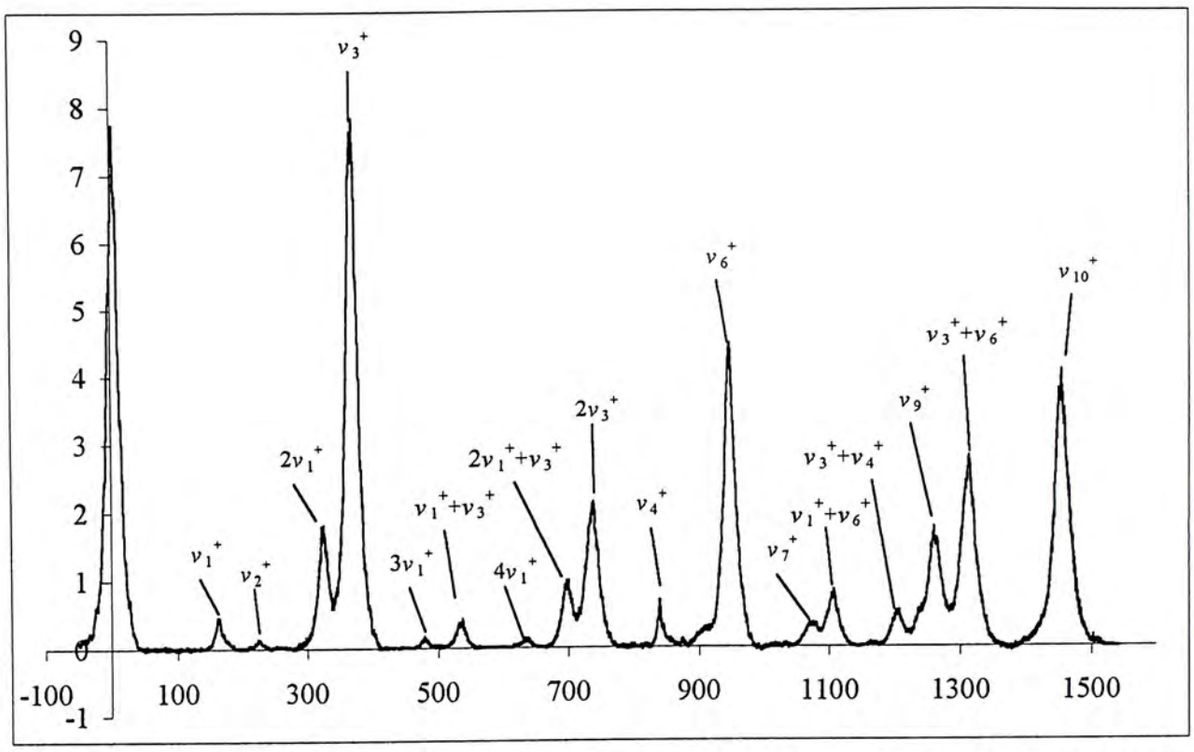

Figure 4a. VUV–PFI–PE Spectrum of *trans*–Dichloroethene Cation, Plotting I(PFI–PE)/I(hv) (Arb. Unit) against Energy above IE (cm^{-1}).

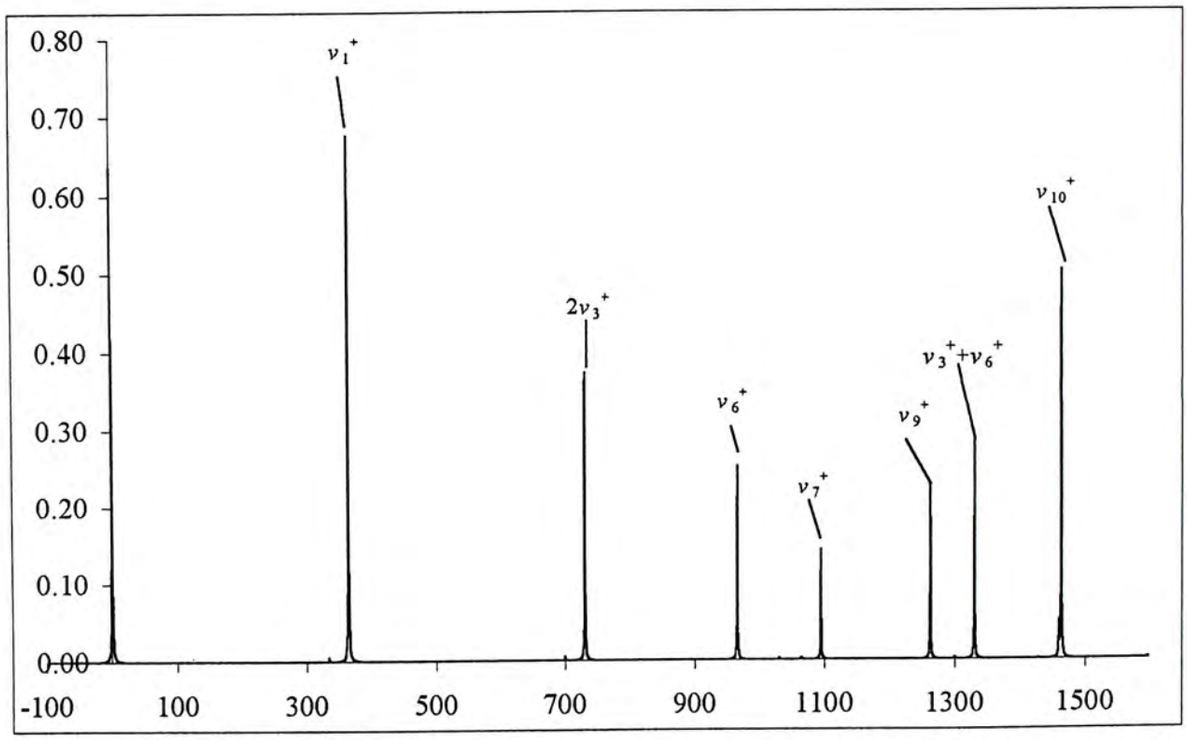

Figure 4b. FCF Simulated Spectrum of *trans*–Dichloroethene Cation, Plotting I(PFI–PE)/I(hv) (Arb. Unit) against Energy above IE (cm^{-1}).

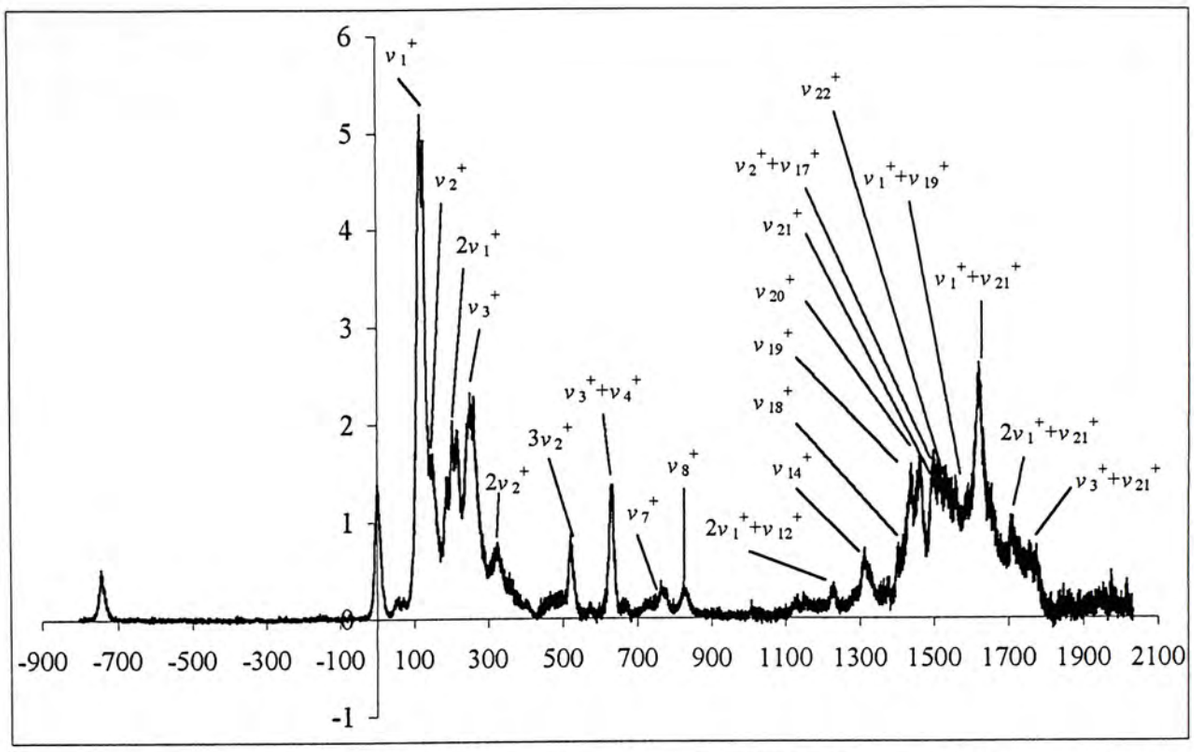

Figure 5a. VUV–PFI–PE Spectrum of Isobutene Cation, Plotting I(PFI–PE)/I(hv) (Arb. Unit) against Energy above IE (cm^{-1}).

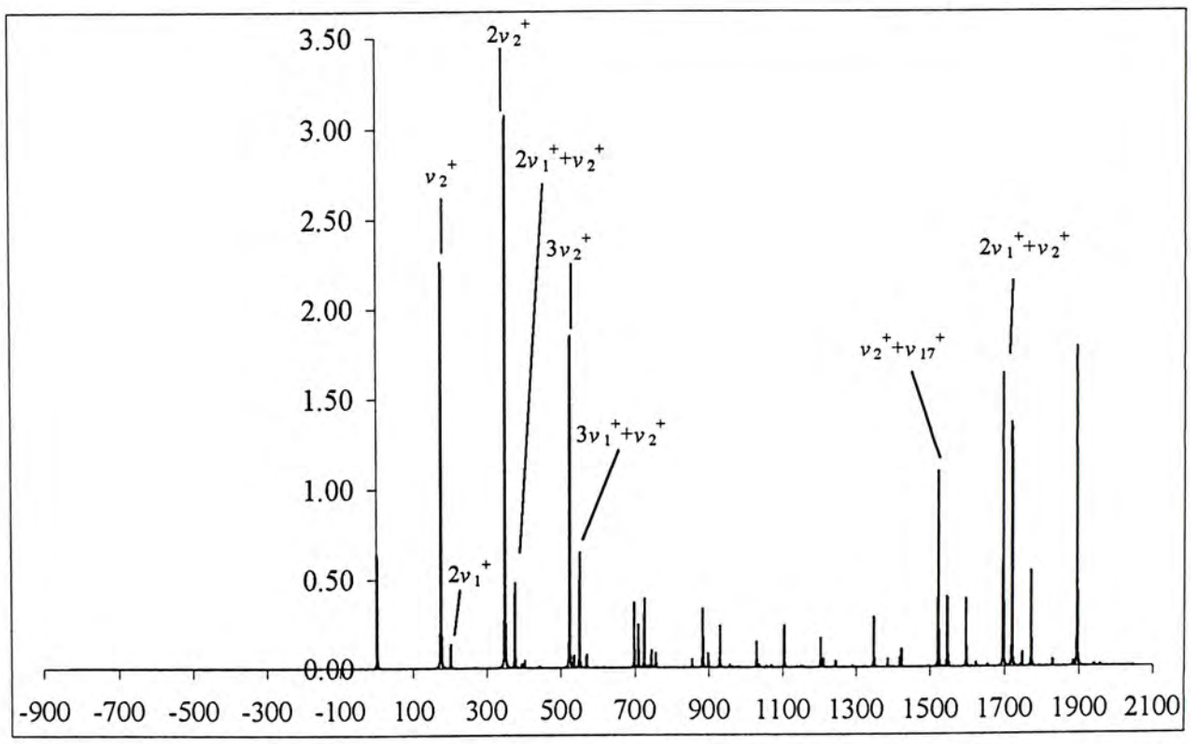

Figure 5b. FCF Simulated Spectrum of Isobutene Cation, Plotting I(PFI–PE)/I(hv) (Arb. Unit) against Energy above IE (cm^{-1}).

Chapter 8
Conclusions

Since conclusions have been made for each project in the respective chapter, we will not specifically comment on the individual chemical systems studied in this work. On the other hand, different models of theory, modified Gaussian–2 (G2++) and Gaussian–3 (G3), as well as other high–level methods including CASSCF, QCISD(T), CCSD(T), etc., have been employed to study the structures and energetics of several interesting systems. We will now remark on the relative merits of these models.

In this thesis, we have employed the G3 method to study the dissociative photoionization of cyanoethylene and photodissociation of phenylacetylene. Combining with the experimental results, good to excellent agreements between the G3 results and experimental values are observed in most cases. In addition, we have used the G2++ method to study the isomers of $C_2H_3S^-$ anions. Although, few experimental data for the $C_2H_3S^-$ anions are available for comparison, we have employed an orbital analysis (NBO) to explain the structures and energetics of these isomers. We have also carried out high–level calculations [QCISD(T) and CCSD(T)] for the bond energies of Fe^+–D, Fe^+–H_2O, and Fe^+–CO. Good agreements between the computed results and experimental date are also observed. Finally, it is noted that the CASSCF method appears to be the best way to identify the charge–localized and –delocalized rhodizonate dianions.

Since most of the calculated results obtained in this work are in good agreements with the available experimental data, and, based on the previous successes for the methods employed, the unexpected large discrepancies between experimental and calculated results for some quantities reported in this thesis may not be due to the failure of the theoretical model. Rather, these discrepancies suggest that the experimental results may be inaccurate and deserve re–examination.

Appendix A

The Gaussian–2 and The Gaussian–3 Theoretical Models

The mathematical details of the Gaussian–2 (G2) and the Gaussian–3 (G3) methodologies are presented below.

A.1 The G3 Theory

The G3 energy is an approximation of the ab initio energy calculated at the QCISD(T)/G3large level. It involves geometry optimization at the MP2(Full)/6–31G(d) level. Also, vibrational frequency calculations at the HF/6–31G(d) level for the zero–point vibrational energy (ZPVE), thermal corrections, and a semi–empirical higher–level correction (HLC) are required. Based on the optimized geometry, several single–point energy calculations are performed, and the G3 energy E(G3) is given as follows.

$$E(G3) = E_{base} + \Delta E(QCI) + \Delta E(+) + \Delta E(2df,p) + \Delta E(G3large) + \Delta E(SO) + 0.8929 \times ZPVE_{HF} + HLC_{G3}, \quad (1)$$

where E_{base} = E[MP4SDTQ/6–31G(d)],

$\Delta E(QCI)$ = E[QCISD(T)/6–31G(d) – MP4SDTQ/6–31G(d)],

$\Delta E(+)$ = E[MP4SDTQ/6–31+G(d) – MP4SDTQ/6–31G(d)],

$\Delta E(2df,p)$ = E[MP4SDTQ/6–31G(2df,p) – MP4SDTQ/6–31G(d)],

$\Delta E(G3large)$ = E[MP2(Full)/G3large – MP2/6–31G(2df,p) – MP2/6–31+G(d) + MP2/6–31G(d)],

$ZPVE_{HF}$ = ZPVE at HF/6–31G(d),

$HLC_{G3} = -6.386\times10^{-3}n_\beta - 2.977\times10^{-3}(n_\alpha - n_\beta)$ and

$-6.219\times10^{-3}n_\beta - 1.185\times10^{-3}(n_\alpha - n_\beta)$

for molecular and atomic species, respectively. Here $n_\alpha \geq n_\beta$ and n_α and n_β are the numbers of α and β valence electrons, respectively.

$\Delta E(SO)$ is spin–orbit correction for atomic species, and is taken from experiment or accurate theoretical calculations in the case where no experimental data are available.

A.2 The G2++ Theory

G2++ is a modified G2 method. It involves geometry optimization and vibrational frequency calculations at the MP2(Full)/6–31++G(d) level. The details of G2++ energies are given below.

$$E(G2++) = E_{base} + \Delta E(QCI) + \Delta E(+) + \Delta E(2df) + \Delta + 0.972 \times ZPVE_{MP2(+)} + HLC_{G2++}, \quad (2)$$

where E_{base} = E[MP4SDTQ/6–311G(d,p)],

$\Delta E(QCI)$ = E[QCISD(T)/6–311G(d,p) – MP4SDTQ/6–311G(d,p)],

$\Delta E(+)$ = E[MP4SDTQ/6–311++G(d,p) – MP4SDTQ/6–311G(d,p)],

$\Delta E(2df)$ = E[MP4SDTQ/6–311G(2df,p) – MP4SDTQ/6–311G(d,p)],

Δ = E[MP2/6–311++G(3df,2p) – MP2/6–311G(2df,p) – MP2/6–311++G(d,p) + MP2/6–311G(d,p)],

$ZPVE_{MP2(+)}$ = ZPVE at MP2(Full)/6–31++G(d),

$HLC_{G2++} = -5.03 \times 10^{-3} n_{\beta} - 0.18 \times 10^{-3} n_{\alpha}$.

Appendix B

Calculation of Enthalpy at 298 K, H_{298}

The theoretical energies obtained with the Gaussian–n methods refer to isolated molecules at 0 K with stationary nuclei, while thermochemical measurements are carried out with vibrating molecules at finite temperature, usually 298 K. Hence, comparison of theoretical results with experimental data normally requires zero–point vibrational energy and thermal corrections. From statistical mechanics, and assuming ideal gas behavior, the difference between the enthalpy at finite temperature (H_T) and the energy at 0 K (E_0) is given by

$$H_T - E_0 = E_T^{trans} + E_T^{rot} + \Delta E_T^{vib} + RT$$

where $E_T^{trans} = (3/2)RT$,

$E_T^{rot} = (3/2)RT$ (for a non–linear molecule)

$E_T^{rot} = RT$ (for a linear molecule) or 0 (for an atom)

$\Delta E_T^{vib} = E_T^{vib} - E_0^{vib}$

$$= \sum_{i}^{3n-6} \frac{h\nu_i}{\exp(h\nu_i / kT) - 1}$$, where ν_i's are scaled harmonic frequencies.

Appendix C

The Function Counterpoise Scheme

In a function counterpoise calculation, the interaction energy is to be corrected. Consider a molecule A–B, the calculation for atom A is repeated, only this time with the whole basis used in the molecule A–B, but without additional nuclear charges (Z(B)=0), or electrons. The same calculation is then performed for atom B, but here the nuclear charge of atom A is set to zero (Z(A)=0). By this functional counterpoise procedure (FCP), we get, in addition to energy values E_A and E_B, two corrected values E_A^C and E_B^C. The BSSE can now be calculated:

$$E^{BSSE} = E_A + E_B - E_A^C - E_B^C$$

The corrected binding energy, $\Delta_{AB}E^C$, is then given by:

$$\begin{aligned}\Delta_{AB}E^C &= \Delta_{AB}E + E^{BSSE} \\ &= E_{AB} - E_A - E_B + (E_A + E_B - E_A^C - E_B^C) \\ &= E_{AB} - E_A^C - E_B^C\end{aligned}$$

where $\Delta_{AB}E = E_{AB} - E_A - E_B$ is the uncorrected energy.